INDI with Flight Envelope Protection for the Flying-V

Jurian Stougie

Technische Universiteit Delft

TUDelft

INDI with Flight Envelope Protection for the Flying-V

by

Jurian Stougie

to obtain the degree of Master of Science
at the Delft University of Technology,
to be defended publicly on Thursday October 6, 2022 at 09:30 AM.

Project duration:	September 1, 2021 – October 6, 2022	
Thesis committee:	Dr. ir. E. van Kampen,	TU Delft, supervisor
	Ir. T. S. C. Pollack,	TU Delft
	Dr. Ir. M. M. van Paassen,	TU Delft
	D. Ir. R. Vos,	TU Delft

Cover image from: https://www.tudelft.nl/lr/flying-v/vliegend-schaalmodel visited at 24-11-2021.

An electronic version of this thesis is available at http://repository.tudelft.nl/.

TU Delft

Abstract

To reduce the environmental impact of aircraft, technological innovations are required. The Flying-V could be one of these technical innovations, as research shows it could be up to 20 % more efficient than regular aircraft of the same size. The Flying-V however has low lateral control authority, and pitch break-up could occur for high angles of attack.

The goal of this research is to increase the maturity of the Flight Control System of the Flying-V. To do so, a Flight Control Systems (FCS) is proposed with Flight Envelope Protection, which is based on an Incremental Nonlinear Dynamic Inversion inner loop control law. For longitudinal control, a C^* control law was implemented, and for lateral control, a Rate Control Attitude Hold control law. To test the performance of this controller, the handling qualities of this FCS were determined in the presence of sensor dynamics, as well as discretization effects. The controller is able to be tuned within level 1 handling qualities at selected design conditions, as long as the time delay of the angular rate sensors is no more than 0.04 seconds.

The effect of sampling time and aerodynamic uncertainties were also evaluated for cruise conditions, and it was shown that the controller is robust for changes in the aerodynamic model, as well as being statically stable for sampling times lower than 0.1 seconds. Finally, the Flight Envelope Protection laws were tested, and shown to meet the requirements, for the cases that were tested, setting a step in maturity for the Flight Control System.

Contents

List of Figures

List of Tables

1

Introduction

Reducing the environmental impact of aircraft is a challenge that becomes each year more important. Due to increasing passenger amount, the emissions due to aviation are growing, as can be seen in Figure 1.1. To limit the growth of emissions, technical advancements are needed. As the technical advancements for conventional shaped aircraft is only limited, other forms of aircraft should also be considered, such as flying wings.

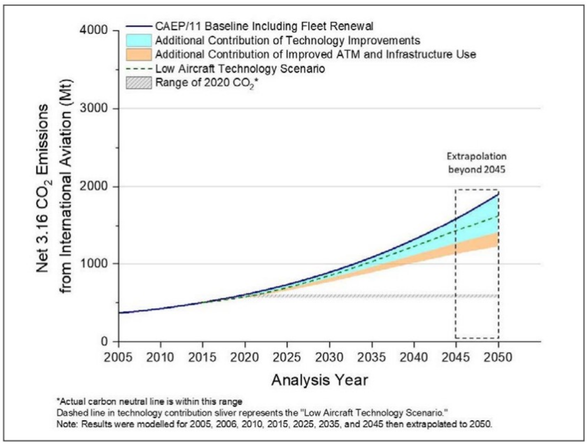

Figure 1.1: CO_2 Emissions from International Aviation, 2005 to 2050, from [13]

The Flying-V is a promising design of a flying wing, as based on research it will be between 10 and 25 % more aerodynamically efficient [11] than conventional aircraft. The Flying-V is a flying wing with two cylindrical fuselages forming a V shape [7]. Another advantage is from flying wings, in general, is that they have reduced noise levels during landing and take-off, in comparison with conventional aircraft [25]. The Flying-V can be seen in Figure 1.2.

However, there are also some challenges for the Flying-V, as research indicated that the Flying-V has pitch break-up tendencies for angles of attack higher than $20°$ [29] and that the dutch roll is unstable [8], there are also indications for low lateral control authority [8].

To improve the flying and handling qualities of an aircraft a Flight Control System (FCS) can be used. Recently a lot of research is done on nonlinear controllers, which are able to deal with nonlinearities in aircraft's aerodynamics and kinematics. One of these is Nonlinear Dynamics Inversion (NDI), which uses a model of the aircraft's dynamics to cancel out aerodynamic and kinematic nonlinearities. One of the disadvantages of NDI is that it is sensitive to model inaccuracies [42]. Therefore Incremental Nonlinear Dynamics Inversion (INDI) was developed, a sensor-based version of NDI, that is less sensitive to model inaccuracies [32].

Van Overeem [28] proposed an INDI controller for the Flying-V, to get the Flying-V to have adequate handling qualities during cruise and approach. However, in this research, the performance of

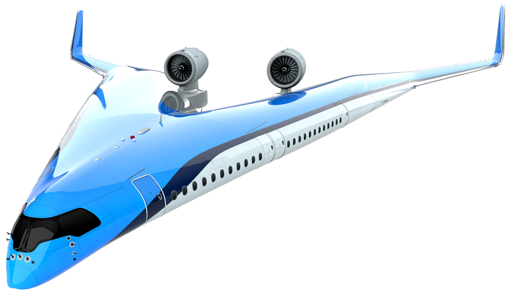

Figure 1.2: Isometric view of the Flying-V obtained from the Flying-V website [1]

the controller is only evaluated in these two conditions. Also, different uncertainties, like for example time delay, were not taken into account. These uncertainties could degrade the performance of the FCS. For certification of an aircraft, it should be shown in a full-scale flight test that the aircraft meets the requirements set by aviation authorities for flying qualities. Before a flight test will be commissioned, simulations of the aircraft are required [39]. The schedule for certification used by Airbus can be found inFigure 1.3. In this research non real-time desktop simulations will be used to evaluate the performance of the INDI control laws for the Flying-V when different uncertainties are in effect, as well as the performance in high angle of attack conditions.

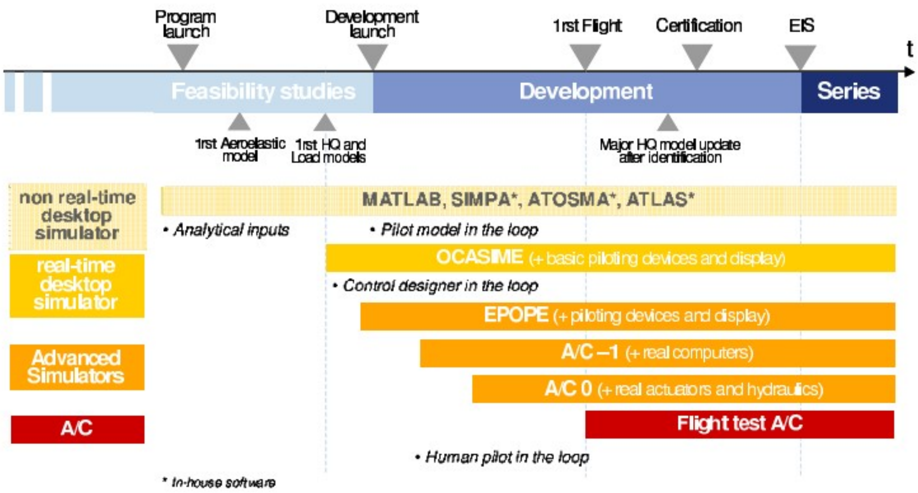

Figure 1.3: Validation means of Airbus for aircraft, from [39]

1.1. Research Questions

The research objective is to increase the maturity of the Flight Control System of the Flying-V by testing and if necessary improve the INDI based flight control laws in high angle of attack conditions and with other effects. To achieve this objective, the following questions should be answered:

1. What are the challenges associated with the Flying-V in terms of stability and control characteristics?
2. What is the state of the art in INDI flight control?

[1] https://www.tudelft.nl/en/ae/flying-v visited at 20-09-2022

3. What is the performance of the INDI controller for the Flying-V under high angle of attack conditions?
   (a) How can the performance of an INDI controller be measured?
   (b) What are the control system requirements for aircraft under high angle of attack conditions?
   (c) How can the INDI controller be extended to include Flight envelope protection?
4. What is the influence of different effects on the robustness of the INDI controller?
   (a) How is robustness of a control system defined?
   (b) What is the influence of time delay?
   (c) What is the influence of the sampling frequency?
   (d) What is the influence of aerodynamic uncertainties?

1.2. Research scope

To answer the research questions, non-real-time desktop simulations of the Flying-V will be used. For the research a simulation of the full-scale aircraft will be used, where a rigid body is assumed, meaning that aero-elasticity effects will not be taken into account. The simulation will be based on already obtained aerodynamic coefficients obtained from Vortex Lattice Method, wind tunnel tests and flight tests. The research will only look at cruise and approach conditions, with a forward c.g. position, due to time limitations. The forward c.g. position is chosen, as van Overeem [27] found that this position in combination with approach conditions,the bare airframe dynamics is the farthest from reaching Level 1 Handling Qualities.

1.3. Report layout

In part I a scientific paper is presented in which the research that was done during this thesis is presented. Next to that, in part II the literature study of this thesis is given. After that in part III the verification of the linearized models and LOES fitting algorithm is given. Finally, in IV the conclusion and recommendations are given.

I

Scientific Paper

Incremental Nonlinear Dynamic Inversion control with Flight Envelope Protection for the Flying-V

Jurian Stougie *
Faculty of Aerospace Engineering, Delft University of Technology, Delft, 2629HS, The Netherlands

To reduce the impact of aviation on the environment, technological innovations, such as the Flying-V are required. The Flying-V is a proposed commercial flying wing, which uses the Airbus A350-900 as reference aircraft. In this work, a Flight Control system for the Flying-V is proposed with a longitudinal C^* control law, and a Rate Control Attitude Hold roll control law. This Flight Control System also includes a Flight Envelope Protection law to prevent reaching angles of attack higher than 30 degrees, where the Flying-V becomes statically unstable. The FEP also prevents the Flying-V from reaching load factors above 2.5 and limits the roll angle. The control laws are tuned to be within level 1 handling qualities in the selected approach and cruise conditions, with the presence of sensor dynamics, and a digital control system. Robustness for aerodynamic uncertainties is also shown. Finally, it is shown that the FEP is able to prevent the angle of attack from becoming too large.

I. Introduction

In 2010 around, 4.9 % of the radiative forcing, causing climate change, comes from aviation, and this is projected to increase 3-4 times in 2050 [1]. To reduce the impact of aviation on the environment, technological innovations are required. The Flying-V is a possible way of reducing the environmental impact of aircraft, as research shows that the Flying-V could be up to 25 % percent more aerodynamically efficient than conventional aircraft [2].

The Flying-V was first proposed by Benad [3] in 2015 as a commercial flying wing. The Airbus A350-900 was used as a reference aircraft [3]. It was designed to have a capacity of 315 passengers, and a cruise speed of Mach 0.85, which is the same as the Airbus reference aircraft.

However, research also showed that the Flying-V has some stability and control characteristics that need extra attention before it can be used as a commercial airliner. It suffers from pitch break-up for angles of attack above 20 degrees [4]. It also has an unstable dutch roll in approach conditions [5] and low lateral control authority [6]. To increase the flying qualities of an aircraft, a Flight Control System can be implemented. Van Overeem [7] proposes a FCS based on Incremental Nonlinear Dynamic Inversion (INDI). This showed that the control laws were able to get the eigenmodes within level 1 handling qualities, however different effects that typically degrade the performance of the control system, such as time delays and sensor noise, were not taken into account. To get the Flying-V certified either the pitch break-up behaviour should be removed by redesigning the airframe, or some form of flight envelope protection should be implemented, to prevent from reaching angles of attack where the pitch break up becomes unrecoverable.

In this research the proposed FCS that is based on INDI will be extenden. INDI, originally called Simplified NDI [8] is a nonlinear sensor-based control method, that requires less model information than, for example, Nonlinear Dynamic Inversion, and is therefore more robust for parametric uncertainties [9]. However, a difference in time delay between the actuator position and angular rate measurements typically degrades the performance of the INDI controller [10].

The goal of this research is to increase the maturity of the Flight Control System of the Flying-V, by evaluating the performance of the FCS with the effects of sensor dynamics, discretization, and aerodynamic uncertainties, as well as implementing a Flight Envelope Protection control law.

The structure of the paper is as follows. In section II the simulation model that will be used is explained,by first showing the aerodynamic model of the Flying-V and then the sensor and discrete time modeling are explained. Next, in section III the control laws of the FCS are given. After this in section **??** the method of evaluating the control laws performance is given. Next, in section V the results of the research are presented and discussed. Finally, the conclusion is shown and recommendations for further research are given in section VI.

*MSc Student, Control and Simulation Research Group, Delft University of Technology

II. Simulation model

In this section, the simulation model that is used for analysis is explained. First, the aerodynamic model of the Flying-V that will be used is presented. Then the way the discretization will be modeled is presented in section II.B, and the sensors in section II.C. Finally, in section IV.B the method of measuring the performance of the control laws is introduced.

A. Flying-V

The general layout of the Flying-V, with the locations of the control surfaces, can be seen in figure 1. A top-view of the wing, with exact inboard (δ_{CS_1}) and outboard (δ_{CS_2}) control surface dimensions is given in figure 2. The rudders (δ_{CS_3}) are integrated into the wing tips. The layout of the Flying-V is taken from the research of Cappuyns [5]. In this research, the forward centre of gravity will be used, which is located 29.4 m behind the nose. The analysis of the flight control system will be done in cruise and approach conditions. Cruise condition is on an altitude of 13 km at Mach 0.85, whereas in approach conditions the altitude is at sea level, with Mach 0.2. The mass of the aircraft is set to 240,000 kg.

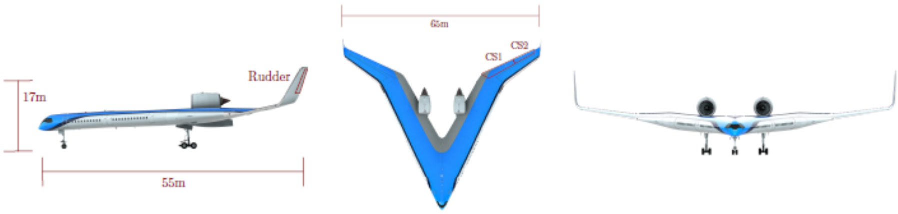

Fig. 1 Flying-V with control surface locations, retrieved from van Overeem [11]

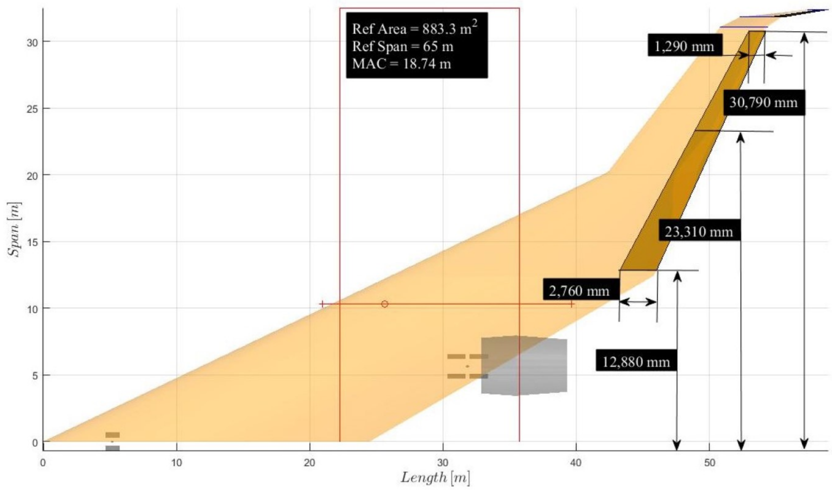

Fig. 2 Flying-V wing, from Cappuyns [5]

1. Aerodynamic model

The aerodynamic data used for this research is also as used by van Overeem [11]. This data is a combination of Vortex-Lattice Method (VLM) data obtained by Cappuyns [5] and Windtunnel data obtained by Garcia [12]. The VLM data is used as a baseline, which is the reason the control surface layout of this model is also used [11]. The longitudinal coefficients for angles of attack under 15 degrees are from the VLM model, whereas the data for angles of attack up to 30 degrees are from the wind tunnel data.

The aerodynamic coefficients are available for two Mach numbers (0.2 and 0.85). As some simulations will have a large variation of airspeed, the aerodynamic data is linearly interpolated between these two Mach numbers. The aerodynamic data does not include compressibility effects. For the simulations, zero wind will be assumed. Furthermore, an atmosphere corresponding to the International Standard Atmosphere will be assumed.

2. Control Surfaces

To increase the flexibility of the control surfaces, the inboard and outboard control surfaces are split up in a left and right control surfaces, which can be directed independently from each other by the control allocation. The actuators are modeled as a second-order transfer function, given in equation 1, for which the values are obtained from Matamoros [13].

$$H_{act} = \frac{\omega_{act}^2}{s^2 + 2\zeta_{act}\omega_{act}s + \omega_{act}^2} = \frac{4000}{s^2 + 140s + 4000} \quad \text{and} \quad H_{thrust} = \frac{1}{0.2s + 1} \tag{1}$$

The rate limit for δ_{CS_1} and δ_{CS_2} is 80 deg/s and for δ_{CS_3} it is 120 deg/s. The position limits are 25 and 30 degrees respectively [5]. The thrust transfer function that converts the commanded thrust to actual thrust is given in equation 1 with the maximum thrust being $3.79 \cdot 10^5$ N [14].

B. Discrete-time modeling

The controller itself will run with a baseline sampling frequency of 100 Hz, and each sensor will have its own sampling frequency. The actuator dynamics as well as the aircraft dynamics will stay a continuous time system. In figure 4 an overview is given of which part of the simulation will run in which time frame. The discrete INDI control law is given in equation 2 [15]. The integrators in the controller will be replaced with discrete integrators using Tustins approximation, as given in equation 3 [16].

$$\boldsymbol{u}_k = \boldsymbol{u}_{k-1} + G^{-1}(\boldsymbol{x}_{k-1})\left(\boldsymbol{\nu}_k - \frac{\boldsymbol{x}_{k-1} - \boldsymbol{x}_{k-2}}{T_s}\right) \tag{2}$$

$$\frac{1}{s} \approx \frac{T_s(z+1)}{2(z-1)} \tag{3}$$

The signals will be sampled before and after the sensors, to get the discrete signals for the sensor and controller dynamics. Before the actuator and the engine dynamics, the signals will be converted back to continuous-time by a zero-order hold. This zero-order hold and sampler will be approximated with equation 4 for the linearized models [16].

$$G_{0_s}(s) = \frac{1 - e^{-sT_s}}{sT_s} \approx \frac{1 - sT_s/6}{1 + sT_s/3} \tag{4}$$

In MATLAB Simulink, zero-order hold blocks are used to sample signals, and signals are automatically converted to continuous time signals if required. Therefore for the nonlinear simulations, the sampling will be done with zero-order hold blocks, and no zero-order block will be used for transforming the signal from discrete to continuous time.

C. Sensor Modeling

The general overview of how the sensors will be modeled can be found in Figure 3. The baseline values for each sensor can be found in table 1. These values are based on values found by Grondman [17] for the sensors of the Cessna Citation II PH-LAB laboratory aircraft. The noise and bias are implemented by adding white noise to the signal, with a mean of the bias, and a standard deviation of the noise level. If the FCS cannot be tuned for level 1 Flying qualities with these values, the sensor(s) that prevent this should be identified, as well as the values for which level 1 can be obtained.

To obtain the angular accelerations, the output of the body rate filters is first filtered by a second order filter with a frequency of 30 rad/s and a damping ratio of 1 and then differentiated. The instantaneous change of pitch angle $\dot{\theta}$ and change of roll angle $\dot{\phi}$ are calculated using the gyroscopes.

It is assumed that the air density and actuator positions are at all times known by the controller, without any time delay, bias, or noise.

Table 1 Baseline sensor parameters, based on Grondman [17]

Sensor	Sampling rate $[hz]$	Time delay [s]	Noise	Bias	Filter time constant
$p, q, r\ [rad/s]$	50	0.1	$1 \cdot 10^{-9}$	$3 \cdot 10^{-5}$	0.05
$\phi, \theta\ [rad]$	50	0.1	$1 \cdot 10^{-9}$	$4 \cdot 10^{-3}$	0.05
$V\ [m/s]$	1/0.065	0.325	$1 \cdot 10^{-4}$	2.5	0.05
$\alpha, \beta\ [rad]$	50	0.1	$7.5 \cdot 10^{-8}$	$3 \cdot 10^{-5}$	0.05
$A_x, A_y, A_z\ [g]$	50	0.1	$1 \cdot 10^{-5}$	$2.5 \cdot 10^{-3}$	0.05

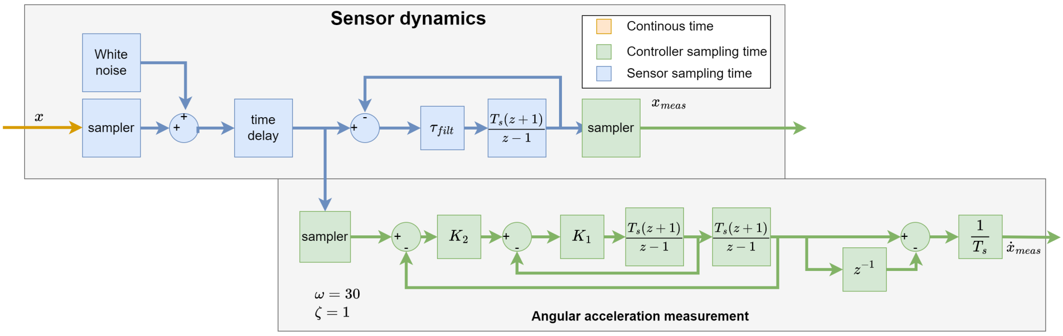

Fig. 3 Sensor dynamics model

III. Control laws

A. Incremental Nonlinear Dynamic Inversion and Control Allocation

The inner loop of the Flight control system will be based on an Incremental Nonlinear Dynamic Inversion (INDI) control law, which is extended with a control allocation algorithm, to ensure efficient use of the control surfaces.

1. INDI

For INDI it is assumed that you can describe the equations of motion as a system given in equation 5. In this equation $\boldsymbol{x}$ is the state vector, $\boldsymbol{u}$ the input vector, and $\boldsymbol{y}$ the output vector. To this system a Taylor expansion is applied, where higher order terms are neglected [10]. This expansion is given in equation 6.

$$\dot{\boldsymbol{x}} = f(\boldsymbol{x}) + G(\boldsymbol{x})\boldsymbol{u} \text{ and } \boldsymbol{y} = h(\boldsymbol{x}) \tag{5}$$

$$\begin{aligned} \dot{\boldsymbol{x}} &\approx \dot{\boldsymbol{x}}_0 + \frac{\partial}{\partial \boldsymbol{x}}[\boldsymbol{f}(\boldsymbol{x}) + G(\boldsymbol{x})\boldsymbol{u}]_{\boldsymbol{u}_0,\boldsymbol{x}_0}(\boldsymbol{x} - \boldsymbol{x}_0) + \frac{\partial}{\partial \boldsymbol{u}}[\boldsymbol{f}(\boldsymbol{x}) + G(\boldsymbol{x})\boldsymbol{u}]_{\boldsymbol{u}_0,\boldsymbol{x}_0}(\boldsymbol{u} - \boldsymbol{u}_0) \\ &= \dot{\boldsymbol{x}}_0 + \frac{\partial}{\partial \boldsymbol{x}}[\boldsymbol{f}(\boldsymbol{x}) + G(\boldsymbol{x})\boldsymbol{u}]_{\boldsymbol{u}_0,\boldsymbol{x}_0}(\Delta\boldsymbol{x}) + G(\boldsymbol{x}_0)(\Delta\boldsymbol{u}) \end{aligned} \tag{6}$$

When the sample rate is high enough, the equation can be simplified to equation 7. For this time scale separation is applied, as it is assumed control surface deflections are faster than the aircraft dynamics [10].

$$\dot{\boldsymbol{x}} \approx \dot{\boldsymbol{x}}_0 + G(\boldsymbol{x}_0)\Delta\boldsymbol{u} \tag{7}$$

Inverting this equation and adding the previous control input gives the control law in equation 8.

$$\boldsymbol{u} = \boldsymbol{u}_0 + G^{-1}(\boldsymbol{x}_0)(\boldsymbol{v} - \dot{\boldsymbol{x}}_0) \tag{8}$$

The INDI control law that will be used is based on the rotational equations of motion, given in equation 9

$$\dot{\boldsymbol{\omega}} = \boldsymbol{I}^{-1}\boldsymbol{M} - \boldsymbol{I}^{-}1\,(\boldsymbol{\omega} \times \boldsymbol{I}\boldsymbol{\omega}) \tag{9}$$

Differentiating equation 9 with respect to the control surface deflections gives equation 10.

$$G(\mathbf{x}) = \frac{\rho V^2 Sc}{2}\boldsymbol{I}^{-1}\begin{bmatrix} C_{l_{\delta_{CS1L}}} & C_{l_{\delta_{CS1R}}} & C_{l_{\delta_{CS2L}}} & C_{l_{\delta_{CS2R}}} & C_{l_{\delta_{CS3}}} \\ C_{m_{\delta_{CS1L}}} & C_{m_{\delta_{CS1R}}} & C_{m_{\delta_{CS2L}}} & C_{m_{\delta_{CS2R}}} & C_{m_{\delta_{CS3}}} \\ C_{n_{\delta_{CS1L}}} & C_{n_{\delta_{CS1R}}} & C_{n_{\delta_{CS2L}}} & C_{n_{\delta_{CS2R}}} & C_{n_{\delta_{CS3}}} \end{bmatrix} \tag{10}$$

Which when filled into equation 8, gives the new control surface deflections, as shown in equation 11, in which $\boldsymbol{P}$ is the inverse of $\boldsymbol{B}$. However, there is a problem with this equation, as the control effectiveness matrix is not square, and thus can not be inverted. This problem will be solved with the control allocation, presented in the next section.

$$\mathbf{u} = \mathbf{u}_0 + \frac{2\boldsymbol{I}}{\rho V^2 * S * c}\boldsymbol{P}(\boldsymbol{\nu} - \dot{\boldsymbol{x}}_0) \tag{11}$$

2. Control Allocation

As the Flying-V has five different control surfaces, there are only three different moments that need to be controlled. This means that the control effectiveness matrix $\boldsymbol{B}$ has five columns and three rows, so the matrix cannot be inverted. This can be solved by using a pseudo-inverse, the choice of which impacts how the control surfaces are used. Furthermore, as the Flying-V has limited control authority, it is important that the control surfaces are used effectively. It is therefore preferable if the control allocation takes actuator limits into account. The maximum control deflections can be calculated using equation 12 [18].

$$\Delta\boldsymbol{u}_{max} = \min\left(\dot{\boldsymbol{u}}_{max}\frac{\omega_{act}}{2\zeta_{act}}, \boldsymbol{u}_{max} - \boldsymbol{u}\right) \text{ and } \Delta\boldsymbol{u}_{min} = \max\left(\dot{\boldsymbol{u}}_{min}\frac{\omega_{act}}{2\zeta_{act}}, \boldsymbol{u}_{min} - \boldsymbol{u}\right) \tag{12}$$

For control allocation, a cascading algorithm was chosen. The first step is to use a Moore-Penrose pseudo-inverse (as given in equation 13), to get the inverse of the control effectiveness matrix $\boldsymbol{B}$. Using the Moore-Penrose pseudo-inverse minimises the total control deflections [19].

$$\boldsymbol{P} = \boldsymbol{B}^T(\boldsymbol{B}\boldsymbol{B}^T)^{-1} \tag{13}$$

The required control deflections can be calculated with equation 14, in which $\boldsymbol{m}^*_{des}$ is defined in equation 15.

$$\boldsymbol{u} = \boldsymbol{P}\boldsymbol{m}^*_{des} \tag{14}$$

$$\boldsymbol{m}^*_{des} = \frac{2\boldsymbol{I}}{\rho V^2 Sc}(\boldsymbol{\nu} - \dot{\boldsymbol{x}}_0) \tag{15}$$

If none of the demanded control deflections are over the limits, calculated with equation 12, these control deflections are used as the output. If this is not the case, the following three scenarios will be checked, in this order:

1) If control surface 3 has reached its limit:
    - Control surface 3 will be set to either its limit or to the required yaw moment divided by $C_{l_{CS3}}$.
    - The column related to control surface 3, and the row related to the yaw moment is removed from the control effectiveness matrix $\boldsymbol{B}$. The desired yaw moment is removed from the $\boldsymbol{m}^*_{des}$.
    - The new $\boldsymbol{m}^*_{des}$ is calculated by subtracting the generated moment by Control surface 3 from $\boldsymbol{m}^*_{des}$.
2) Else, if either Control surface 2 left, or right (or both) have reached their limits:
    - Find which of these two control surfaces is the most over its limit, and calculate $a = u/u_{lim}$. Scale the other control surface with a, so that direction is preserved between these two control surfaces.
    - Calculate the new $\boldsymbol{m}^*_{des}$ by subtracting the generated moments from $\boldsymbol{m}^*_{des}$.
    - Remove the rows related to $\delta_{CS_{2_L}}$ and $\delta_{CS_{2_R}}$ from $\boldsymbol{B}$
3) Else, if either Control surface 1 left, or right (or both) have reached their limits:
    - Find which of these two control surfaces is the most over its limit, and calculate $a = u/u_{lim}$. Scale the other control surface with a, so that direction is preserved between these two control surfaces.
    - Calculate the new $\boldsymbol{m}^*_{des}$ by subtracting the generated moments from $\boldsymbol{m}^*_{des}$.
    - Remove the rows related to $\delta_{CS_{1_L}}$ and $\delta_{CS_{1_R}}$ from $\boldsymbol{B}$

If one of the inboard or outboard control surfaces is at its deflection limits, the other control surfaces are no longer scaled, to prevent the control surfaces from staying locked at their deflection limit. This means direction, the ratio between moments, is temporarily not guaranteed until the control surface is no longer at its limit.

After this, there are four cases:

1) $\boldsymbol{B}$ has more columns than rows: in this case, the Moore-Penrose pseudo-inverse is used to invert the $\boldsymbol{B}$.
2) $\boldsymbol{B}$ has the same amount of rows as columns: it can be inverted normally.
3) $\boldsymbol{B}$ has fewer columns than rows: The problem is now over-determined, and the result will not fully meet the desired moment. To minimize the error, the following pseudo-inverse is used [19]: $\boldsymbol{P} = \left(\boldsymbol{B}_{red}^T \boldsymbol{B}_{red}\right)^{-1} \boldsymbol{B}_{red}^T$
4) $\boldsymbol{B}$ is empty, meaning there are no control surfaces left to allocate. In this case, the control allocation does not completely meet the desired moment.

With the new inversed $\boldsymbol{B}$ matrix and $\boldsymbol{m}_{des}^*$ the other control surfaces can be allocated. If some control surfaces reach their limit, the algorithm starts again, until no surfaces are over the limit, or there are no control surfaces left to allocate.

B. Flight Control System

The overall control layout is based on the Flight control system proposed by Lombaerts [20], however, some changes were made. The angle of attack loop is removed, and the controller's load factor input is used straight into the reference model for longitudinal control, because the Flight Envelope Protection (FEP) law that is used limits the angle of attack by limiting the commanded load factor, making the angle of attack loop not necessary. The inner loop NDI controller is also replaced with an INDI control law. The way the FEP was implemented is also different, which will be elaborated on in section III.C. An overview of the Flight Control System can be found in Figure 4.

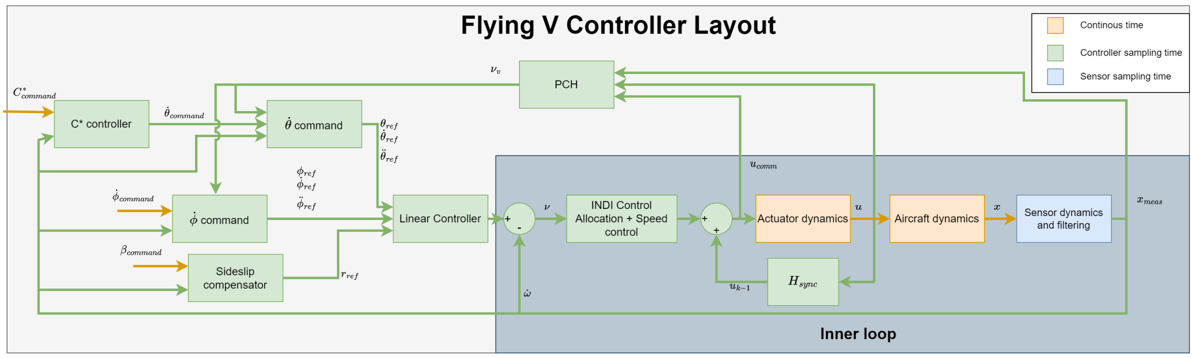

Fig. 4 Block diagram of the Flight Control System of the Flying-V

1. C* controller

For longitudinal control, a C^* controller is chosen. C^* control is based on the C^* criterion. The idea behind C^* control is that it is a mix of pitch rate and load factor control, where in lower speed regimes the pitch rate is dominant, whereas for higher speeds the load factor control is dominant [21]. C^* control is selected as Airbus also uses this control law in there Aircraft, for example, the A320 also uses C^* control [22]. This will increase the familiarity that pilots have when flying with the Flying-V for the first time [21]. It should be noted however that Airbus uses a combination of load factor and pitch rate feedback, that is not strictly C^* control [22].

The C^*-command is multiplied by $\frac{\cos(\theta)}{\cos(\phi)}$ to include turn compensation, as well as lower the commanded load factor at high pitch angles. [20]. After this, the pitch rate is subtracted from the command, to get a commanded load factor, which then is used to get a $\dot{\theta}_{command}$ for the pitch reference model. This is done with PI-control, combined with a feedforward path. The feedforward path is used to shape the aircraft's response to pilot inputs. An overview of the C^* controller can be seen in figure 5.

2. Reference models

The reference models for pitch and roll are largely identical. The difference between the reference models is that the roll protection is located in the roll reference model, which will be elaborated on in section III.C.

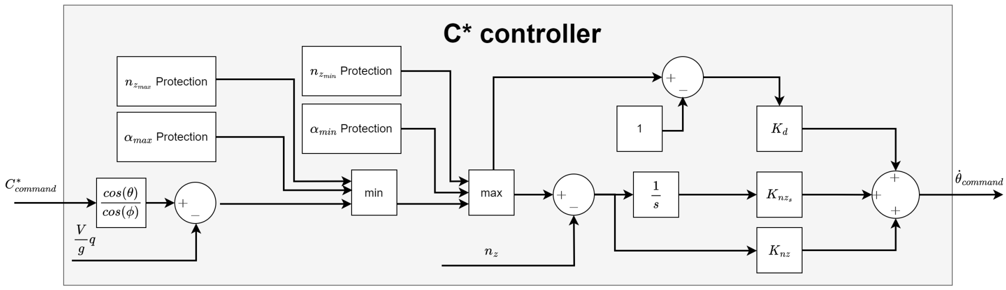

Fig. 5 Block diagram of the C^* controller

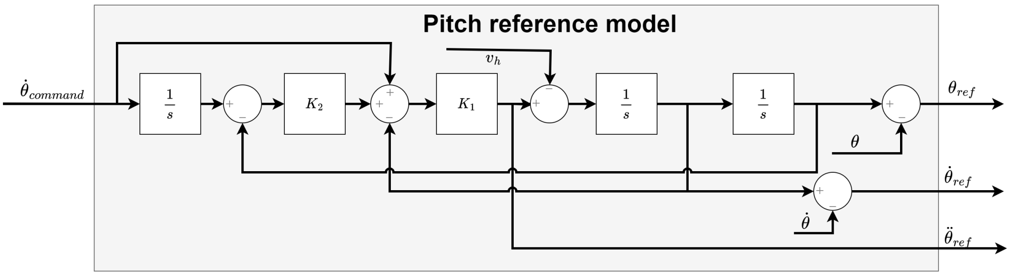

Fig. 6 Block diagram of the pitch reference model

Both reference models act as second-order filters. The relation between the gains and the natural frequency and damping ratio can be found in Equations 16.

$$K_1 = 2\zeta\omega \text{ and } K_2 = \frac{\omega}{2\zeta} \tag{16}$$

The roll reference model has as input a roll rate command from the pilot, and the reference model acts as a Rate Control Attitude Hold controller. A difference from the controller from Lombaerts [20] is that this control law does not switch to attitude control for roll angles above 30 degrees.

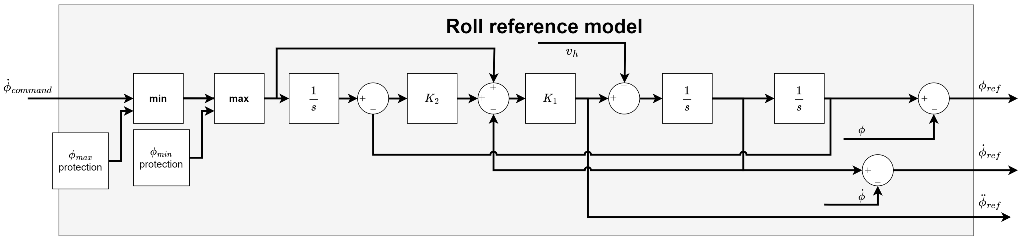

Fig. 7 Block diagram of the roll reference model

3. Sideslip Compensation

The block diagram for the sideslip compensator is given in figure 8. w is approximated with equation 17. This will take care of the control of the yaw channel, meaning that the FCS will have sideslip control, and not yaw rate control [20]. For this control law sideslip angle measurements are required.

$$w \approx V \sin(\alpha) \tag{17}$$

4. Linear controller

The linear controller converts the outputs of the reference models and sideslip compensator to the virtual control signal ν. It is a PI controller using the control laws given in equations 18, 19, and 20 which are obtained from Lombaerts[20].

$$\nu_p = \left(K_\phi + \frac{K_{\phi I}}{s}\right) \cdot \phi_{ref} + K_{\dot{\phi}} \cdot \dot{\phi}_{ref} + K_{\ddot{\phi}} \cdot \ddot{\phi}_{ref} \tag{18}$$

$$\nu_q = K_\theta \cdot \theta_{ref} + K_{\dot{\theta}} \cdot \dot{\theta}_{ref} + K_{\ddot{\theta}} \cdot \ddot{\theta}_{ref} \tag{19}$$

$$\nu_r = K_r \cdot r_{ref} \tag{20}$$

5. Pseudo Control Hedging

Pseudo Control Hedging (PCH) is a way to prevent actuator windup. PCH lowers the reference model signal, by calculating the difference between the demanded moment, and the estimated generated moment. The virtual control hedge can be calculated with equation 21, which are obtained from Grondman [17].

$$\boldsymbol{\nu}_h = G(\boldsymbol{x})(\boldsymbol{u}_{comm} - \boldsymbol{u}_{actual}) \tag{21}$$

The virtual control hedge will be subtracted from the reference models, as can be seen in figures 7 and 6. This means that difference in the yaw moment is not hedged. PCH will lower the commanded signals down to a level, which is obtainable by the control surface deflections.

6. Synchronisation Filter

In previous research, it was found that it is important for INDI that u_{k-1} is in sync with the angular acceleration measurements [23]. Time delays, originating from for example sensors, could make the difference in timing too large, degrading the performance of the FCS. To minimize this effect, a synchronisation filter is applied. This synchronisation filter consists of the same second-order filter that is applied to obtain the angular accelerations and a time delay. The time delay was set to be $2ms$ higher than the time delay of the angular rate sensor, to have room for unaccounted time delays

C. Flight Envelope Protection

The Flight Envelope Protection (FEP) consists of three different parts. Angle of Attack protection, load factor, and roll angle protection. The angle of attack and load factor protections limits the commanded load factor in the C^* controller, as is shown in figure 5 [24]. The roll angle protection does this with the commanded roll rate, as can be seen in 7.

1. Angle of Attack Protection

As the Flight Envelope Protection is implemented to ensure the Flying-V will stay in its flight envelope at all times, the angle of attack protection is very important, to prevent it from reaching pitch break-up. It is found that while the pitch

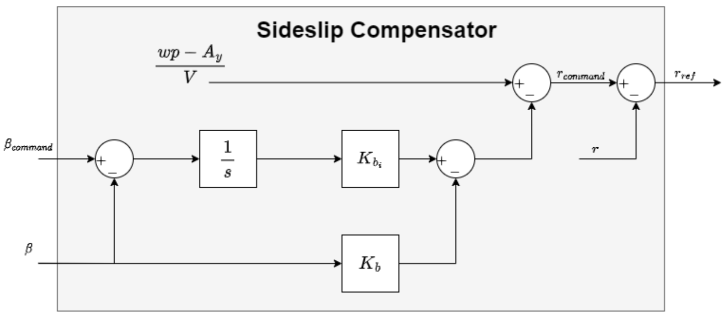

Fig. 8 Block diagram of the Sideslip compensator

break-up effect already starts at angles of attack above 20 degrees, it is important that the Flying-V does not reach an angle of attack higher than 34 degrees, as after this the aircraft can no longer recover itself, even with maximum control deflections. It should be kept in mind that this is in an optimal case, where the control surfaces could be deflected from maximum deflection to minimum, in practice, the maximal recoverable angle of attack will be lower. The maximum load factor, due to the angle of attack protection, $n_{z_{\alpha_{max}}}$ is calculated with equation 22, as well as the minimum $n_{z_{\alpha_{min}}}$ [24].

$$n_{z_{\alpha_{max}}} = n_z + K_{\alpha_{max}} (\alpha_{max} - \alpha) \quad \text{and} \quad n_{z_{\alpha_{min}}} = n_z + K_{\alpha_{min}} (\alpha_{min} - \alpha) \tag{22}$$

The maximum angle of attack protection only becomes active for angles of attack higher than 15 degrees, and the minimum for angles of attack below 0 degrees, this is done to make sure the protection does not limit the Flying-V's maneuverability in normal flight. The signals are respectively 2.5 and -1 when the protections are inactive.

2. Load factor protection

The maximum load factor can be calculated using equation 23 [20]. In this equation $C_{L_{max}}$ is set to the C_L at an angle of attack of 25 degrees, and $\Delta C_{L_{max}}$ is set to 0.01.

$$n_{z_{max}} = \max\left(1, \min\left(2.5, 1 + \frac{(C_{L_{max}} - \Delta C_{L_{max}})\overline{q}S}{W}\cos(\phi) - n_y \sin(\phi) - \cos(\gamma) + \frac{T}{W}\sin(\alpha)\cos(\phi)\right)\right) \tag{23}$$

The minimum load factor, $n_{z_{min}}$ is equal to -1 [20].

3. Roll angle protection

The maximum roll angle (in degrees) can be calculated with equation 24 [20]. This is then transformed to a maximum and minimum roll rate signal with equation 25.

$$\phi_{max} = \min\left(66, \arccos\left(\frac{mg\cos(\gamma)}{T\sin\alpha + (C_{L_{max}} - \Delta C_{L_{max}})\overline{q}S}\right)\right) \tag{24}$$

$$\dot{\phi}_{max} = K_{\phi_{protec}}(\phi_{max} - \phi) \text{ and } \dot{\phi}_{min} = K_{\phi_{protec}}(-\phi_{max} - \phi) \tag{25}$$

The roll angle protection is only active when the roll angle is within two degrees of the limit, so the protection does not limit the maneuverability in normal flight.

IV. Tuning and Performance evaluation

In this section it is presented how the performance of the FCS will be evaluated. First, the tuning of the FCS parameters is explained. After this, additional performance evalutation metrics are presented. Next to that it is given how the effects of sampling time and aerodynamic uncertainties will be evaluated. Finally the method of testing the FEP laws is presented.

A. Tuning

For tuning of the gains of the control laws, multi-objective optimisation is used. The longitudinal design parameters (C^*-controller, pitch reference model, and the v_q control law) is tuned separately from the lateral parameters. This can be done as they do not influence the scoring of the other part.

The tuning is done using an optimization algorithm, that for the first run will generate a list of 200 numbers for the gains, following a normal distribution. For these gains, a score is calculated, using the objectives given in the next section. The best scoring combinations of gains then is used to generate the next list of gains. The tuning algorithm stops when the score does not improve for two runs in a row.

This method of tuning the gains does converge on a minimum score. However as it is a problem with many local minima, this does not mean the gains that are found is the combination of gains that are the best solution for the problem. It is therefore important to use multiple different initial guesses for tuning.

1. Tuning Objectives

The longitudinal tuning objectives can be found in table 2. The lateral tuning objectives are given in table 3. The constraint objectives are based on requirements from MIL-STD-1797A [25], and will have a score of 0 when in level 1 flying qualities, a score of 100 plus extra for the distance from level 1 when in level 2, and a score of 1000 plus extra for the distance from level 2 when in level 3 or worse. The distance is the difference in the value of the two levels, and is multiplied respectively with 50 and 500.

Table 2 Longitudinal tuning objectives

Description	Type	Min level 2	Min Level 1	Max Level 1	Max Level 2
		Linear Analysis			
Gain Margin v_q $[dB]$	Constraint	0	6	-	-
Phase Margin v_q $[deg]$	Constraint	0	45	-	-
ω_{sp} $[rad/s]$	Constraint	0.6	1	-	-
ζ_{sp} $[-]$	Constraint	0.25	0.35	1.3	2
CAP $[g^{-1}s^{-2}]$	Constraint	0.038	0.085	3.6	10
ω_{BW} $[rad/s]$	Constraint	1	3	-	-
τ_p $[s]$	Constraint	-	0	0.1	-
$score_{LOES}$ $[-]$	Constraint	-	-	15	100
ω_{CO} $[rad/s]$	Minimize	-	-	-	-
		Simulation with C^*_{comm} step input of 1.8 at t = 1s. T_{sim} = 20s			
$\max(\delta_{CS})$ $[deg]$	Minimize	-	-	-	-
$\delta_{CS_{activity}}$ $[deg/s]$	Minimize	-	-	-	-
Settling Time C^* $[s]$	Minimize	-	-	-	-
Overshoot C^* $[-]$	Minimize	-	-	-	-

For the simulations, the actuator activity will be determined with equation 26, and will be the average of all the five control surfaces. The settling time is the time from the start of the step input until the signal is within 1% of the commanded signal. Overshoot (OS) will be calculated with equation 26. These extra parameters are used to minimise control surface activity.

$$\delta_{CS_{activity}} = \frac{\int_0^T |\dot{\delta}_{CS}| dt}{T} \quad \text{and} \quad OS = max\left(\frac{y_{actual} - y_{command}}{y_{command}}\right) \tag{26}$$

2. Gain and Phase Margins

The gain and phase margins are determined by opening the loop after the summation point after the Linear Controller in figure 4. The objective for the crossover frequency is to be minimised, however, a too low crossover frequency can reduce the disturbance rejection capabilities of the FCS [26], to ensure enough disturbance rejection capabilities, a minimum crossover frequency of 5 rad/s was set.

3. Low Order Equivalent System

To obtain the short period parameters, as well as the Control Anticipation Parameter, a Low Order Equivalent System (LOES) is fitted on the pitch rate transfer function. To get the LOES fit, the pitch rate response and load factor response should be fit simultaneously. The reduced order model of the pitch rate can be found in equation 27. [25]

$$\frac{q(s)}{\delta_{es}(s)} = \frac{K_q s \left(s + \frac{1}{T_{\theta_1}}\right)\left(s + \frac{1}{T_{\theta_2}}\right) e^{-\tau_e s}}{\left(s^2 + 2\zeta_{sp}\omega_{sp}s + \omega_{sp}^2\right)\left(s^2 + 2\zeta_{ph}\omega_{ph}s + \omega_{ph}^2\right)} \tag{27}$$

If the natural frequency of the phugoid and short-period is separated sufficiently, with at least a factor 10, the two modes can be looked at separately [25]. This reduces the model to equation 28 [27].

Table 3 Lateral tuning objectives

Description	Type	Min level 2	Min Level 1	Max Level 1	Max Level 2
Linear Analysis					
Gain Margin ν_p $[dB]$	Constraint	0	6	-	-
Phase Margin ν_p $[deg]$	Constraint	0	45	-	-
Gain Margin ν_r $[dB]$	Constraint	0	6	-	-
Phase Margin ν_r $[deg]$	Constraint	0	45	-	-
$1/T_s$ $[s^-1]$	Constraint	-0.087	-0.058	-	-
T_r $[s]$	Constraint	0	-	1	1.4
ω_{dr} $[rad/s]$	Constraint	0.4	0.5	-	-
ζ_{dr} $[-]$	Constraint	0.02	0.08	-	-
$\omega_{dr}\zeta_{dr}$ $[rad/s]$	Constraint	0.05	0.015	-	-
$score_{LOES}$ $[-]$	Constraint	-	-	15	100
ω_{CO_p} $[rad/s]$	Minimize	-	5	-	-
ω_{CO_r} $[rad/s]$	Minimize	-	5	-	-
Simulation with $\dot{\phi}_{comm}$ block input of 3 deg between t = 1s and t = 14s. T_{sim} = 18s					
$\max(\delta_{CS})$ $[deg]$	Minimize	-	-	-	-
$\delta_{CS_{activity}}$ $[deg/s]$	Minimize	-	-	-	-
Settling Time $\dot{\phi}$ $[s]$	Minimize	-	-	-	-
Simulation with Wind step w_{wind} = 16 m/s at t = 1s. T_{sim} = 15s					
$\delta_{CS_{activity}}$ $[deg/s]$	Minimize	-	-	-	-

$$\frac{q(s)}{\delta_{es}(s)} = \frac{K_q\left(s + \frac{1}{T_{\theta_2}}\right)e^{-\tau_e s}}{\left(s^2 + 2\zeta_{sp}\omega_{sp}s + \omega_{sp}^2\right)} \quad \text{and} \quad \frac{n_z'(s)}{\delta_{es}(s)} = \frac{K_n e^{-\tau_n s}}{\left(s^2 + 2\zeta_{sp}\omega_{sp}s + \omega_{sp}^2\right)} \tag{28}$$

The reduced load factor model that should be fitted simultaneously, in accordance with MIL-STD-1797A [25] is given in the same equation. n_z' is the normal acceleration at the instantaneous center of rotation.

The LOES is fitted on the linearized High Order System (HOS), by matching its frequency response between 0.1 and 10 [rad/s] [25]. MIL-STD-1797A [25] however mentions that there is insufficient data on how to best score the matching of the LOES and HOS, but suggests using equation 29, in which G is the gain in dB and ϕ the phase in degrees over 20 frequency points evenly spaced on a logarithmic scale, with K having a value around 0.02 [28].

$$M = \Sigma(G_{HOS} - G_{LOES})^2 + K\Sigma(\phi_{HOS} - \phi_{LOES})^2 \tag{29}$$

The disadvantage of this method is that it weighs the error at every frequency point the same, where it was found that the match at frequencies around 1-4 rad/s was more important than at other frequencies. Therefore the Maximum Unnoticeable Added Dynamics envelopes were developed. These envelopes can be approximated with the transfer functions in table 4.

Table 4 MUAD envelope transfer functions

	Upper bound	Lower bound
Gain	$\frac{3.16s^2+31.61s+22.79}{s^2+27.14+1.84}$	$\frac{9.55\cdot10^{-2}s^2+9.92s+2.15}{s^2+11.60s+4.95}$
Phase	$\frac{68.89s^2+1100.12s-275.22}{s^2+39.94+9.99}$	$\frac{475.32s^2+184100s+29456.1}{s^2+11.66s+3.89\cdot10^{-2}}e^{-0.0072s}$

For this research, a weighting factor is applied which is the inverse of the maximum allowable gain or phase mismatch, according to the MUAD envelope. It should be noted that the envelopes are not symmetric so that the weight can be different depending if the LOES has a higher or lower value at the same frequency than the HOS [29]. The score is calculated with equation 30.

$$M = \Sigma((G_{HOS} - G_{LOES}) * w_G) + \Sigma((\phi_{HOS} - \phi_{LOES}) * w_\phi) \tag{30}$$

After the low order model is fitted, the short period frequency and damping ratio can be found. The Control Anticipation Parameter (CAP) can be found with equation 31.

$$CAP = \frac{\dot{q}}{n_{z_{ss}}} = \frac{\omega_{sp}^2}{n_\alpha} \quad \text{and} \quad n_\alpha = \frac{V}{gT_{\theta_2}} \tag{31}$$

For the lateral tuning, there is another low-order equivalent system required. The LOES for roll angle is given in equation 32, which should be fitted together with the sideslip LOES given in the same equation [25]. The method of fitting the LOES to the HOS is the same as for the longitudinal case.

$$\frac{\phi}{\delta_{as}} = \frac{K_\phi\left(s^2 + 2\zeta_\phi\omega_\phi s + \omega_\phi^2\right)e^{-\tau_{ep}s}}{\left(1+\frac{1}{T_s}\right)\left(1+\frac{1}{T_r}\right)\left(s^2+2\zeta_d\omega_d s+\omega_d^2\right)} \quad \text{and} \quad \frac{\beta}{\delta_{rp}} = \frac{\left(A_3s^3 + A_2s^2 + A_1s + A_0\right)e^{-\tau_{e\beta}s}}{\left(1+\frac{1}{T_s}\right)\left(1+\frac{1}{T_r}\right)\left(s^2+2\zeta_d\omega_d s+\omega_d^2\right)} \tag{32}$$

The spiral mode is allowed to be unstable, as long as the time to double the amplitude T_2 is larger than 20 s. The relation between the time constant and doubling time is given in equation 33 [28].

$$T_2 = -T_s \ln(2) \tag{33}$$

4. Attitude Bandwidth

Bandwidth is defined as the highest frequency with either a phase margin of 45 degrees, or a gain margin of 6 dB. It is found by finding the frequency $\omega_{BW_{phase}}$ where the phase equals -135 deg. Then find the frequency $\omega_{BW_{gain}}$ where the gain is 6 dB higher than the gain where the phase is -180 deg. The lower frequency of $\omega_{BW_{phase}}$ and $\omega_{BW_{gain}}$ is the bandwidth [25].

As not only the bandwidth frequency itself influence how the pilot experiences the aircraft, but also the phase roll-of, the equivalent time delay parameter τ_p needs to be evaluated. τ_p can be calculated with equation 34, in which ω_{180} is the frequency at phase = -180 deg, and $\phi_{2_{\omega_{180}}}$ is the phase at ω_{180} [25].

$$\tau_p = -\frac{(\phi_{2_{\omega_{180}}} + 180^\circ)}{57.3 \cdot 2 \cdot \omega_{180}} \tag{34}$$

B. Additional evaluation criteria

The first measurement of the performance of the controller is the ability to be tuned to level 1 flying qualities for set objectives. However, there are also other handling requirements, that are not used for tuning.

1. Extra Handling qualities

The evaluated extra requirements are Pitch attitude dropback, Gibson phase rate, Flight-path angle bandwidth, and the equivalent time delays of the low order equivalent systems.

The pitch attitude dropback was developed to evaluate highly augmented control systems by Gibson [30]. This criterion can be used to predict the possibility of Pilot Induced Oscillations. If this criterion is combined with the bandwidth and equivalent phase delay, the criterion is a good predictor for PIO [31]. The criterion can be evaluated by time-domain analysis from a block longitudinal stick input.

The Gibson phase rate criterion looks at the phase roll of around the crossover frequency, making it comparable with the equivalent time delay parameter.

The flight path bandwidth requirement is a requirement to make sure that the relation between the flight path and pitch attitude response appears reasonable to the pilot. The flight path bandwidth ω_{BW_γ} is defined as the frequency where the phase of the flight path lags the stick input by 135 degrees [31].

To ensure that the perceived time delay caused by the sensors and filters is not too large, which could degrade the tracking capabilities of the pilot, there are limits on the maximum equivalent time delay of the pitch rate and roll LOES model. [25]. To be within level 1, the equivalent time delay should be no more than 0.1 s [25].

2. Sampling time and Aerodynamic uncertainties

As there is not much aerodynamic data for the Flying-V available yet, there are quite some uncertainties for this data. Especially as the data that is used for this research is based on a combination of two data-sets, and is linearly interpolated between two Mach numbers.

To evaluate the effect of aerodynamic uncertainties, 100 simulations will be run, with all the aerodynamic parameters being varied with a normal distribution with a standard deviation of 20% of the parameter. The aerodynamic data used for the INDI control law and pseudo-control hedging will not change, introducing a difference in what the control law uses as aerodynamic data, and what the actual data is.

In reality, when the Flying-V is getting closer to being a commercial aircraft, more accurate aerodynamic data will be available, but there will still be a difference in the actual aerodynamic properties.

The simulation will be of 25 s, and have a step roll rate input of 5 $[deg/s]$ between 5 and 15 s. As the C^* input gets multiplied with the roll angle, this manoeuvre will also contain a changing longitudinal input. The first parameter that will be evaluated is the tracking RMS error, for the C^* and roll rate tracking, which are calculated with equation 35

$$\epsilon_{RMS} = \sqrt{\frac{1}{n}\Sigma(y_{actual} - y_{command})^2} \tag{35}$$

The other parameter that is evaluated is the control surface activity, which is calculated with equation 26.

The effect of sampling time will be analysed with the same method, with 100 simulations varying the sampling frequency from 1000 Hz down to 10 Hz, the tuning will be done for a sampling frequency of 100 Hz.

3. FEP testing

To test the flight envelope protection, the following requirements for the FEP were set:

- The FEP laws should not engage when flying well within the normal flight envelope [32]
- The normal acceleration n_z should not go out the limit of -1g ≤ Nz ≤ 2.5g [33]
- The angle of attack should not go over 30 degrees

For the evaluation, two different simulations will be done, as they were found to be the most challenging for the flight envelope protection laws. The first simulation will have a step C^* input of 2, with thrust set to 0. The second simulation will have the same C^* input, but for t = 5s until t = 15s also have a $\dot{\phi}_{comm}$ of 5 degrees. Both simulations will run for 250 seconds. The simulations will be done starting from a height of 13 km and 1 km.

V. Results and discussion

In this section the results of this research will be presented and discussed. First, the results from tuning the FCS will be given in cruise and approach conditions, with and without the contribution of sensor dynamics and discretization effects. After this, in section V.B the other handling qualities will be evaluated for the Flying-V with the sensor dynamics. The effects of different sampling frequencies is evaluated in section V.C. Then the effects of aerodynamic uncertainties are presented in section V.D and finally the FEP laws are evaluated in section V.E.

A. Tuning results

An overview of the results for tuning in cruise conditions can be seen in figure 9. The complete longitudinal tuning results are given in table 5a, and in table 5b the complete lateral tuning results.

The handling qualities of the model without sensor dynamics and without the discretization effects are all well within level 1. The gain and phase margins are also larger than required. It should be noted that the gain margin for pitch is negative, indicating that the open-loop is unstable, but the closed-loop is not.

When adding the sensor dynamics and making the controller discrete, the gain and phase margins become smaller, as expected. Where all the handling quality requirements are still within level 1, the gain and phase margin requirements are no longer met. Therefore a third model was made, with an angular rate sensor with less time delay. For the new sensors, the time delay for the angular rates is changed to 0.04 s, with a filter time constant of 0.03. These values for the sensor parameters will be used for the next results, as well as the tuning for the adjusted sensors. It should be noted that when the sampling frequency of the angular rate sensor was set to 100 Hz, and the time delay to 0.05 s, the FCS could also be tuned to be within level 1 handling requirements, with enough gain and phase margins. For higher time delays a compromise between enough bandwidth and phase margin could no longer be found.

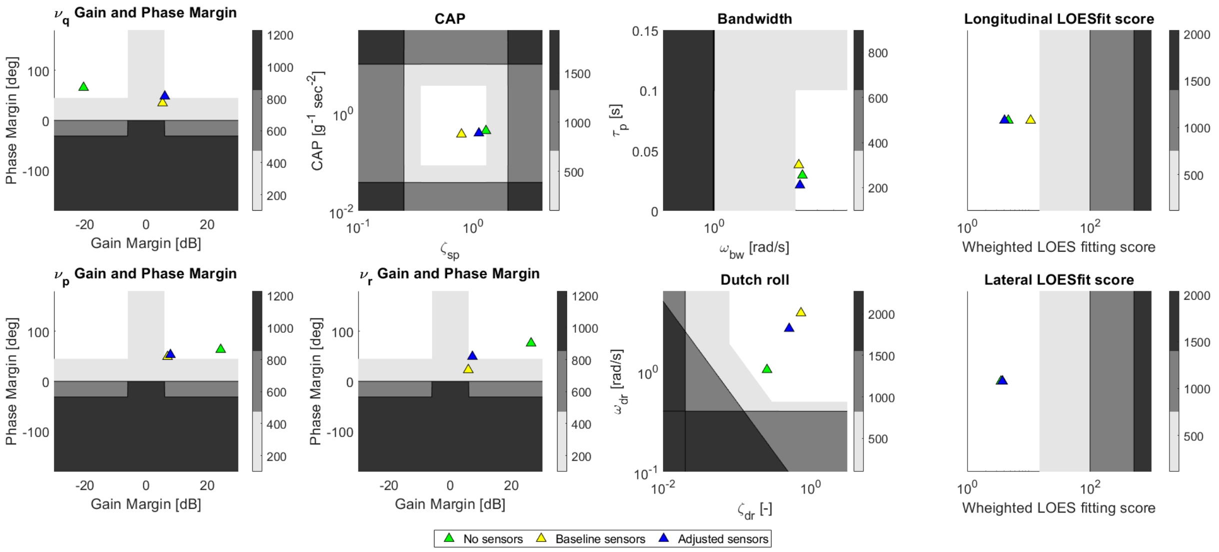

Fig. 9 Tuning scores for tuning in cruise conditions

Table 5 Tuning results. Green being within level 1, and yellow being within level 2 Handling Qualities

(a) Longitudinal tuning results for cruise conditions.

Description	No sensors	Adjusted sensors	Baseline sensors
Linear Analysis			
GM ν_q $[dB]$	20.37	6.08	5.35
PM ν_q $[deg]$	65.34	48.06	34.5
ω_{sp} $[rad/s]$	1.81	1.82	2.18
ζ_{sp} $[-]$	1.29	1.12	0.79
CAP $[g^{-1}s^{-2}]$	0.433	0.388	0.368
ω_{BW} $[rad/s]$	3.27	3.17	3.12
τ_p $[s]$	0.029	0.021	0.038
$score_{LOES}$ $[-]$	4.67	4.05	10.79
ω_{CO} $[rad/s]$	34.7	7.72	6.19
Simulation with C^*_{comm} step input of 1.8 at t = 1s. T_{sim} = 20s			
max(δ_{CS}) $[deg]$	10.97	11.21	11.20
$\delta_{CS_{activity}}$ $[deg/s]$	0.17	0.69	0.77
ST C^* $[s]$	3.89	2.72	4.48
OSC* $[-]$	0.08	0.08	0.13

(b) Lateral tuning results for cruise conditions

Description	No sensors	Adjusted sensors	Baseline sensors
Linear Analysis			
GM ν_p $[dB]$	24.28	7.91	6.97
PM ν_p $[deg]$	63.16	52.95	48.98
GM ν_r $[dB]$	26.29	7.19	5.85
PM ν_r $[deg]$	75.95	49.28	22.82
$1/T_s$ $[s^{-1}]$	0.074	0.065	0.07
T_r $[s]$	0.513	0.604	0.52
ω_{dr} $[rad/s]$	1.036	2.66	3.81
ζ_{dr} $[-]$	0.26	0.52	0.74
$\omega_{dr}\zeta_{dr}$ $[rad/s]$	0.27	1.37	2.83
$score_{LOES}$ $[-]$	3.54	3.74	3.77
ω_{CO_p} $[rad/s]$	36.29	6.69	5.10
ω_{CO_r} $[rad/s]$	29.75	5.96	5.56
Simulation with $\dot{\phi}_{comm}$ block input of 3 deg between t = 1s and t = 14s. T_{sim} = 18s			
max(δ_{CS}) $[deg]$	6.04	7.74	4.1
$\delta_{CS_{activity}}$ $[deg/s]$	0.75	1.78	1.29
ST ϕ $[s]$	5.27	4.42	5.53
Simulation with Wind step v_{wind} = 16 m/s at t = 1s. T_{sim} = 15s			
$\delta CS_{activity}$ $[deg/s]$	1.89	3.07	6.91

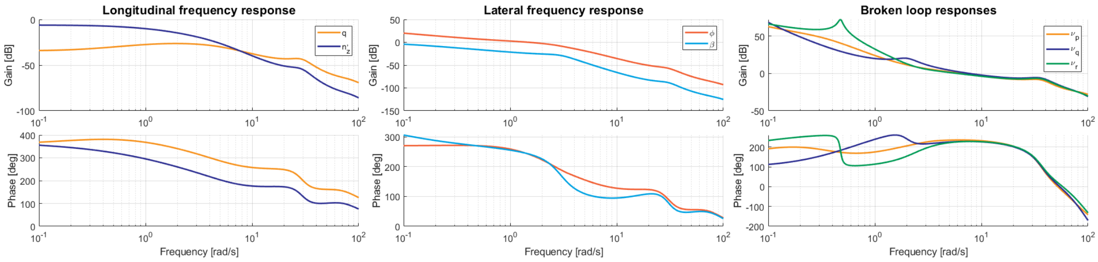

Fig. 10 Frequency responses in cruise condition with the adjusted sensor model

In figure 10 the frequency responses for the adjusted sensors model and tuning is given, as well as the broken-loop frequency responses. The two bumps present around 20 and 40 rad/s are caused by the sensor and actuator dynamics.

In figure 11 the response to a C^* block input is given for the three models, with the best found tuning for each case. There are two main differences, the first one is that the model with the baseline sensors shows multiple oscillations in the C^* response, whereas the other two models do not show this behavior. This is in accordance with the fact that this case has a lower phase margin than the two other models. The other main difference is the deflection of the rudder. The rudder in the model without sensors does not move, which is as expected, as the maneuver is purely longitudinal. However, the rudder oscillates a lot in the other two models. This is caused by the noise from the sideslip sensor. To improve on this behavior, the time constant of the sideslip filter was changed to 0.1 for the adjusted sensors case. This reduces the chatter of the rudder marginally, but the behavior is still apparent.

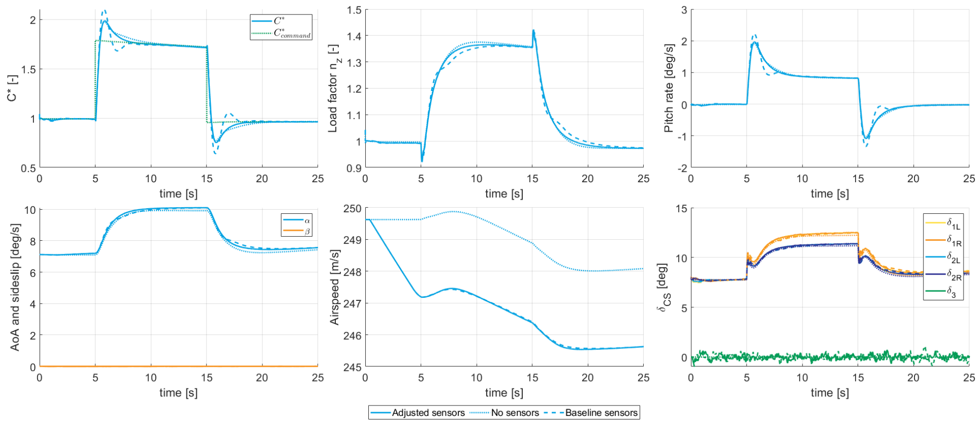

Fig. 11 C^* step response in cruise conditions

The time response to a $\dot{\phi}_{comm}$ block input is presented in figure 12. Here the model with the adjusted sensors response has more overshoot, but also a smaller settling time, indicating that the tuning for this model was more aggressive. This is also shown in the control surface deflections, which are larger for the adjusted sensor model. This difference is however not inherent on the model, but is a different solution found by the tuning algorithm. The chatter of the rudder is also present here for the baseline and adjusted sensors.

After the tuning was done for cruise conditions, and sensor parameters were determined for which level 1 handling qualities could be obtained, the FCS in approach conditions was evaluated. The results for this can be found in figure 13. As can be seen in this figure, retuning was required, as the cruise condition tuning no longer met the bandwidth requirement, as well as the LOES had a large mismatch. After retuning all handling qualities are again in level 1. Furthermore, after the retuning, the new handling quality parameters are close to the values of the cruise tuning, in cruise conditions. This indicates that the aircraft would react in a comparable way in this condition, as in cruise conditions, making the aircraft more predictable, and easier to fly.

B. Other Handling Qualities

An overview of the handling qualities parameters in cruise conditions is given in table 6.

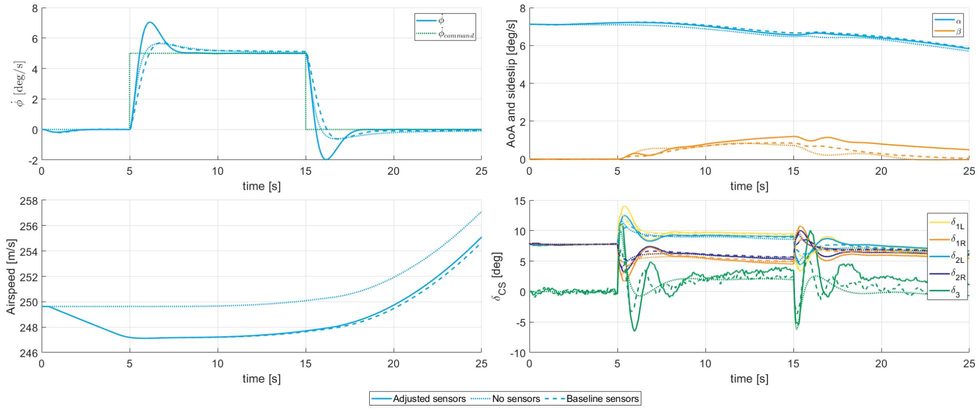

Fig. 12 Roll rate step input response in cruise conditions

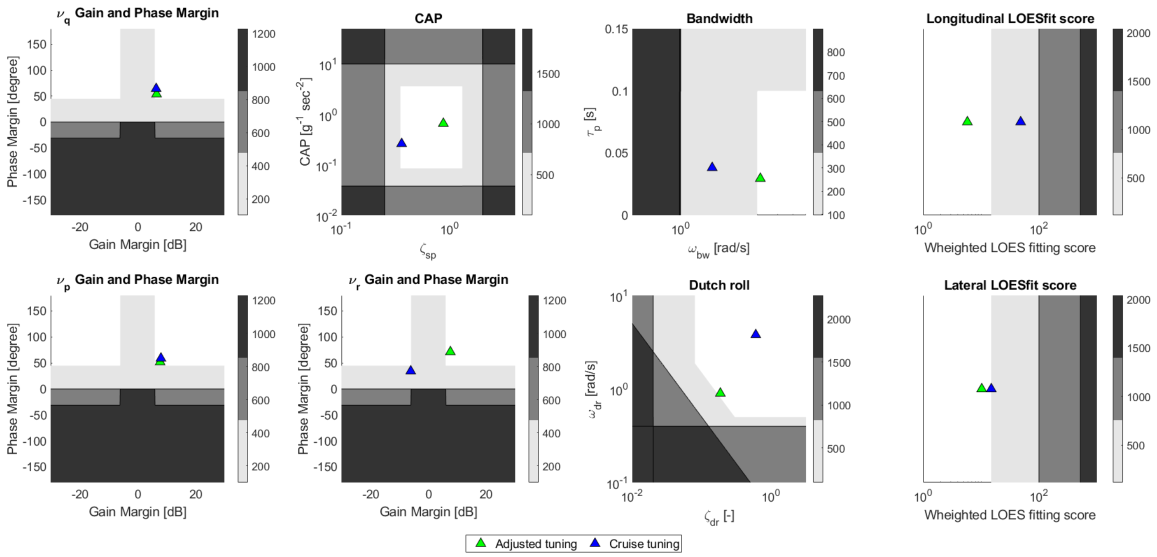

Fig. 13 Tuning scores for tuning in approach conditions

As can be seen in figure 14, the pitch attitude dropback is in the acceptable region. Next to that, it can also be seen that the phase rate criterion is also met, which was as expected, as the bandwidth requirement was also met. The phase rate is even in the optimum design region.

The flight path bandwidth is on the edge of the requirement, as shown in figure 14, but is in the level 1 area. All the time delays are lower than 0.1 s, except for the sideslip time delay. However, this is not a problem, as the 0.1s requirement is only applicable for the other time delays, where for sideslip higher time delays are acceptable [25].

C. Influence of sampling time

In figure 15 the RMS tracking error and control surface activity for varying sampling frequency is given. The trend in the tracking error and controller activity that can be observed is that with a longer sampling time, the error gets larger. This is as expected. However, for the range that is looked at, the error does not increase much, and there is a lot of variance. The chosen sampling frequency of 100 Hz that is used previously is deemed sufficient, as the error does not seem to decrease much with higher sampling frequencies.

In figure 16 the time traces for the varying sampling times are given. Where it also can be observed that for the range between 1000 and 10 Hz, the FCS is capable of tracking the roll rate reference signal, without much difference in tracking error, or control surface deflections. When increasing the sampling time above 0.1 s, the system becomes

Table 6 Extra Handling qualities parameters in cruise condition

Parameter	Value	Parameter	Value
$\frac{q_{peak}}{q_{ss}}$ [-]	1.9255	τ_{eq} [s]	0.057
$\frac{\Delta\theta_{peak}}{q_{ss}}$	1.33	τ_n [s]	0.047
Average phase rate [deg/Hz]	18.53	τ_{ep} [s]	0.079
ω_{-180} [deg]	1.079	$\tau_{e\beta}$ [s]	0.156
ω_{BW_γ} [rad/s]	0.61		

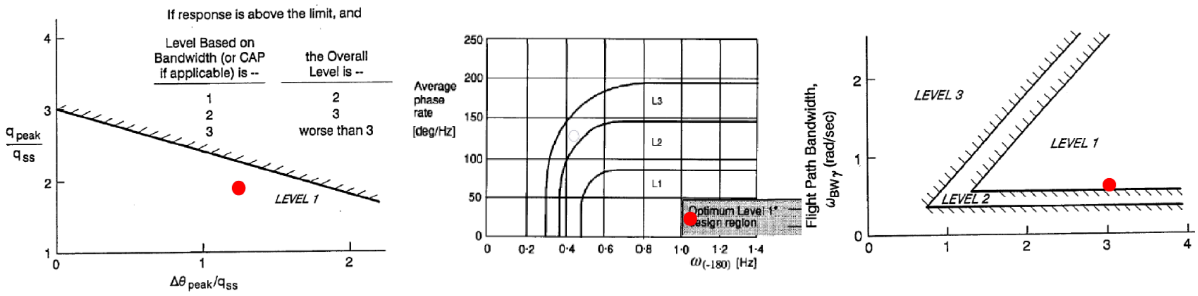

Fig. 14 Pitch attitude dropback, phase rate and Flight path bandwidth results in cruise, adapted from Mitchell [31] and Gibson [30]

unstable. As a sample rate of 100 Hz for a control system is easily obtainable, it can be concluded that the sampling rate will not be a problem for the FCS, as the performance, as well as the gain and phase margins for a sampling rate of 100 Hz are all within the requirements that were set.

D. Aerodynamic uncertainties

The variance of the tracking error and control surface activity, with varying aerodynamic uncertainties is given in figure 17. For the C^* and roll rate tracking error, there is little spread. With the maximum difference in C^* tracking error being 25 %, and also in roll rate tracking the difference between the highest and lowest value is roughly two thirds. This indicates that the FCS is robust in roll and C^* tracking for varying model parameters.

The variance of the inboard and outboard control surface activity is also small, and is caused by the variance in control surface effectiveness. The spread in rudder activity is however larger.

To explain the larger in variance, the time responses are plotted in figure 18. There you can see large oscillations in rudder deflection, as well as a large initial deflection, with for certain cases even reaching the deflection limit. As the

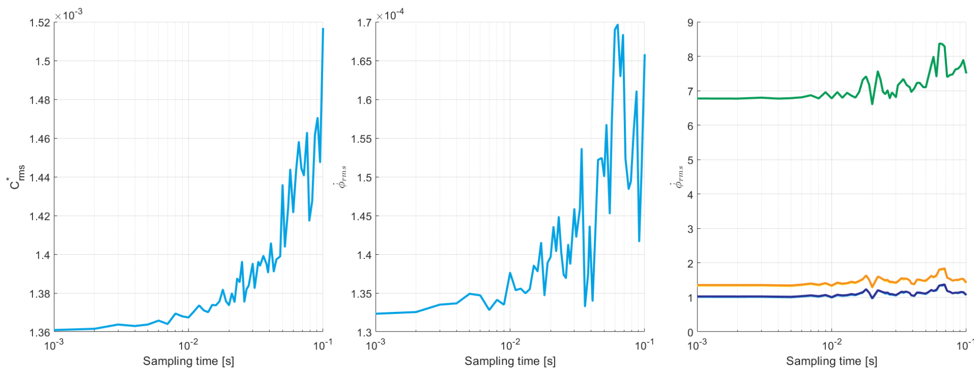

Fig. 15 Tracking error and controller activity for varying sampling times

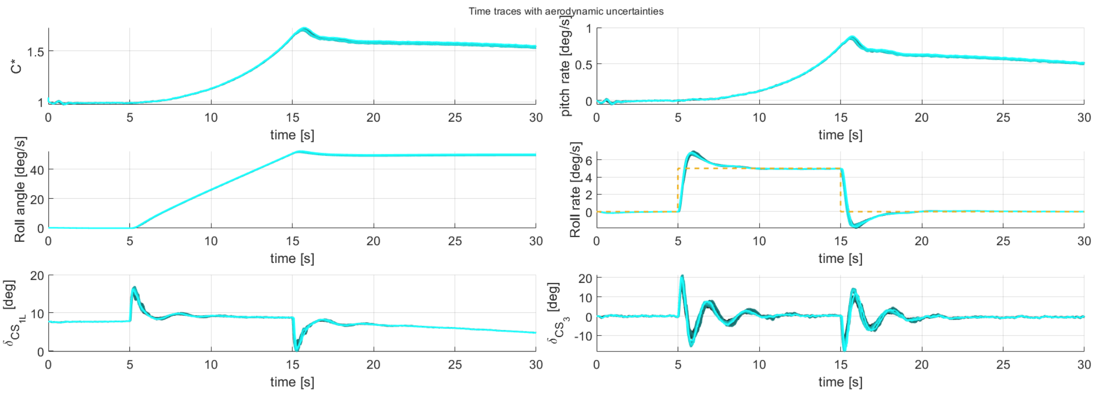

Fig. 16 Response to roll rate step, with varying sampling time, where lighter color = higher sampling time

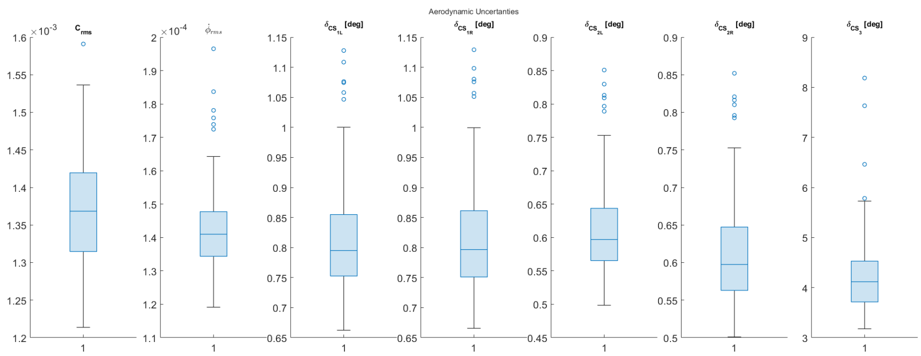

Fig. 17 Boxplots showing the variance in tracking error and control surface activity, with varying aerodynamic uncertainty

control authority of the rudder is already low in nominal conditions, the extra oscillations can be explained by the fact that the simulations with extra rudder activity, are the simulations where the rudder effectiveness is reduced. In the figure, it can also be seen that all simulations reach a trim position within 5 seconds and that there is almost no variation in roll rate and C^* tracking after the first five seconds. This shows that the FCS is robust for aerodynamic uncertainties, but if the control authority of the rudder is found to be lower than expected, this could be problematic.

E. Flight Envelope Protection

To improve the performance of the Flight Envelope Protection, first gain scheduling was implemented, as the airspeed during the manoeuvres changes a lot. The gain scheduling is dependent on the airspeed and is linearly interpolated between the cruise condition tuning, and tuning done at a airspeed of 100 m/s at an altitude of 1 km. For the lateral gains, a third point was added tuning at 70 m/s at an altitude of 1 km.

After tuning the Flight Envelope Protection control law gains, it was found that the angle of attack protection gain should be made air density dependant, to ensure that for all altitudes, the FEP is able to prevent the Flying-V reaching angle of attacks higher than 30 degrees. The FEP parameters that were used are given in table 7. The gain for minimum and maximum angle of attack was set to the same value.

Table 7 Flight envelope protection parameters

Parameter	Value for $\rho = 1.225$	Value for $\rho = 0.26$
$\alpha_{max}[deg]$	22	24
K_α	0.025	0.01
$K_{\phi_{protec}}$	0.3	0.3

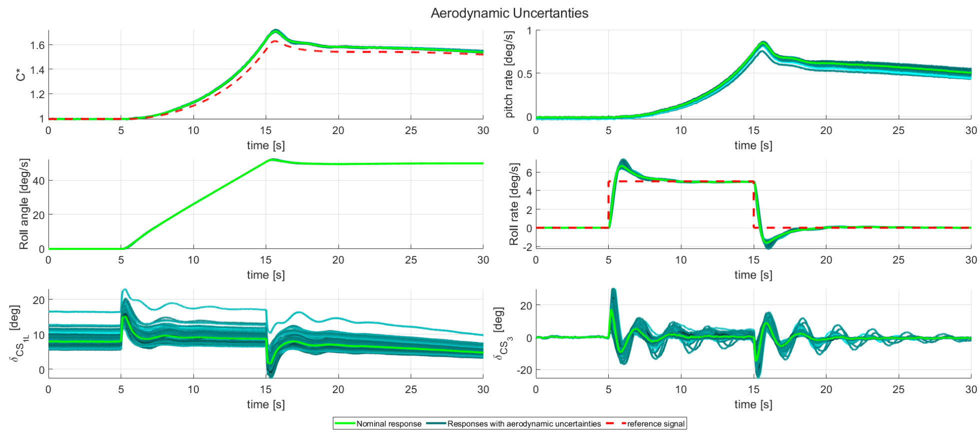

Fig. 18 Response to roll rate step, with varying aerodynamic uncertainty, where lighter color = more uncertainty

In figure 19 the results are given from the simulation starting at 13 km altitude, with only the C^* input. It can be seen that around t = 35s the angle of attack protection becomes active, after the angle of attack is above 15 degrees. However, the protection only starts limiting the load factor after t = 45 s. There is then an overshoot of just under 3 degrees, but keeping the angle of attack well below the maximum of 30 degrees. The angle of attack goes down to 20 degrees, while in the meantime the pitch angle goes down from just above 45 degrees to around -5 degrees. After t = 100s, the angle of attack converges at α_{max}. It should further be noticed that the oscillations of the rudder around t = 50s and t = 120s increases. This coincides with the moments the airspeed of the aircraft is the lowest at around 100 m/s. As the tuning at 100 m/s was done at an altitude of 1 km, and it is now at an altitude of 13 km, there is less dynamic pressure, than what the controller was tuned for.

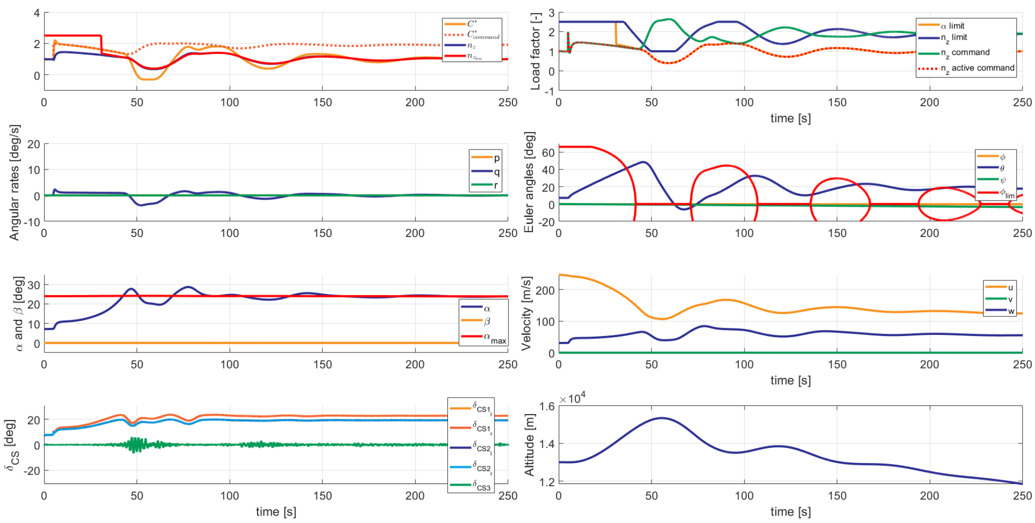

Fig. 19 Flight Envelope Protection starting from cruise height

In figure 20 the simulation starting from cruise conditions, with a roll rate input is given. When looking at the longitudinal protection, it is nearly identical to the values in figure 19. This is a good sign, as this means that the added roll angle, and roll protection is not degrading the performance of the longitudinal flight envelope protection. After t = 55s, the max roll angle becomes smaller than the current roll angle, and the protection starts to demand a negative roll angle. The roll angle becomes zero around t = 70 s. During this period, the rudder is oscillating from maximum to minimum deflections, this is because of the low dynamic pressure, combined with the tuning that was not done for this point.

The last simulation for the flight envelope protection is given in figure 21. This is the simulation that starts at an

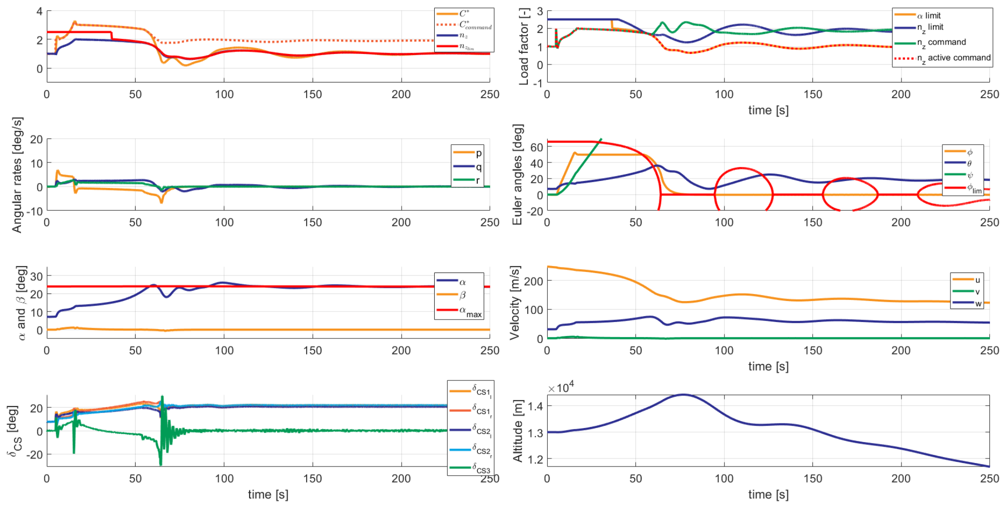

Fig. 20 Flight Envelope Protection starting from cruise height, with roll

altitude of 1 km, with the roll rate input. It should be kept in mind that the simulation time is 100 s instead of 250, as the aircraft reaches the angle of attack limit faster in this condition. The pitch angle goes below zero twice, instead of only once. The rudder oscillation in this case seems to have a lower frequency, but higher amplitude. The oscillations occur at an airspeed of around 50 m/s, which could be resolved by scheduling gains for this low velocity. Because of the lower starting airspeed, the roll limits already limits the roll, when there is still an roll input. The controller is able to deal with this, even though the rudder, as well as two control surfaces are at their saturation limit during this period, indicating that the aircraft is at its limit for this manoeuvre. The angle of attack during this period is not getting above 30 degrees and the roll angle is getting to zero, this however takes more time, then for the cruise condition time, which can be explained by the fact that the control surfaces are at their limit. And while the rudder is also at its saturation limit, the sideslip angle is not becoming to large.

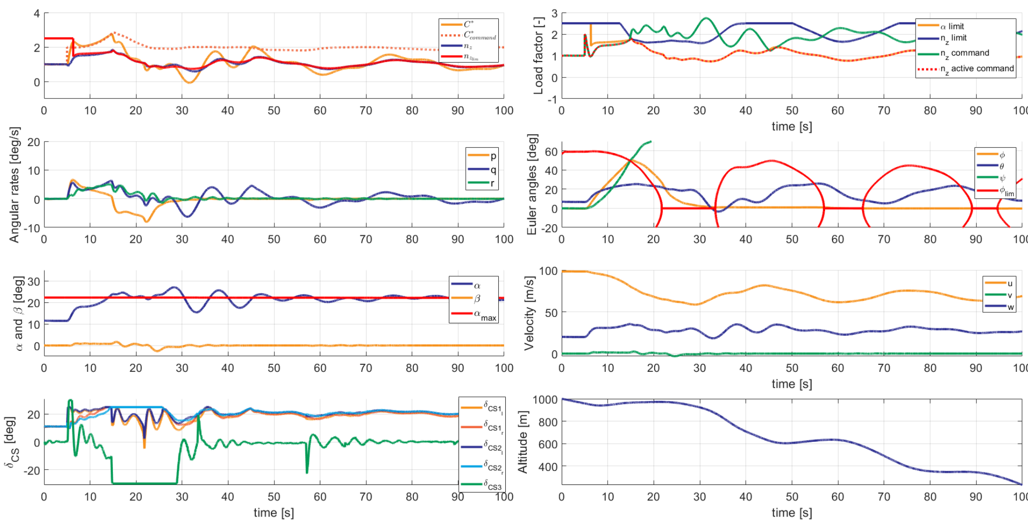

Fig. 21 Flight Envelope Protection starting from from 1 km altitude, with roll

VI. Conclusion

In this research a Flight Control System for the Flying-V is proposed. The FCS is based on an innerloop INDI control law, with a C^* control law for longitudinal control and a Rate Control Attitude Hold control law for roll. It is shown that this controller can be tuned to be within Level 1 Handling Qualities, for the selected cruise and approach conditions. When sensor dynamics and discrete effects are taken into account, the gain and phase margins decreases. As long as the body rate sensor is fast enough, the FCS can still be tuned into level 1 handling qualities. The effect of sampling frequency is evaluated, and a sampling frequency of 100 Hz is fast enough to not introduce extra tracking errors. It is also shown that the FCS is robust to aerodynamic uncertainties, as the response does not change much for differences in aerodynamic parametersup to 20 %.

Finally the Flight Envelope Protection is evaluated. For the cases evaluated, the angle of attack stays under the set limit of 30 degrees. As the FEP only activates for higher angles of attack, and when the roll angle is close to its limit, it also does not influence the aircraft response when well within its flight envelope. Lastly the load factor does not exceeds the limits meaning that the FEP meets all the requirements that were set, for the cases that are tested.

However there are some factors that should be further investigated. This research only looks at one position of the c.g. of the aircraft, which is also perfectly known. Further research could investigate the effects of changing c.g. location, as well as c.g. location mismatch. The Flight Envelope protection could also be improved, by for example also take the angle of attack rate into account, making the angle of attack protection more gradual, and possibly being able to make the maximum angle of attack larger. The minimum angle of attack and load factor protection laws are also not tested yet. Another improvement that could be done is adding a V_{max} and V_{min} protection.

There are also other effects that could degrade the performance of the control laws, that are not taken into account yet. These are for example aero-elasticity effects, which could have a big impact on the controllers performance, and time delay within the flight control computer.

It should also be investigated if improving the gain scheduling, and making it also dependant on the air density, is enough to reduce the rudder oscillations, or that the lateral control authority should be increased in another way. Lastly it could be investigated if the required sensors in this research are feasible for the Flying-V, or that the control laws should be changed, to control laws that are less sensitive for time delays induced by the sensors, to ensure enough gain and phase margin.

References

[1] Lee, D., Pitari, G., Grewe, V., Gierens, K., Penner, J., Petzold, A., Prather, M., Schumann, U., Bais, A., Berntsen, T., Iachetti, D., Lim, L., and Sausen, R., "Transport impacts on atmosphere and climate: Aviation," *Atmospheric Environment*, Vol. 44, No. 37, 2010, pp. 4678–4734. https://doi.org/10.1016/j.atmosenv.2009.06.005, transport Impacts on Atmosphere and Climate: The ATTICA Assessment Report.

[2] Faggiano, F., "Aerodynamic Design Optimization of a Flying V Aircraft," Master's thesis, TU Delft, 2016. URL http://resolver.tudelft.nl/uuid:0b1472a5-3aad-433c-9a64-242c84b114fd.

[3] Benad, J., "The Flying V - A new Aircraft Configuration for Commercial Passenger Transport," *Deutscher Luft- und Raumfahrtkongress 2015, Rostock*, Deutsche Gesellschaft für Luft- und Raumfahrt, 2015. https://doi.org/10.25967/370094.

[4] Palermo, M., "The Longitudinal Static Stability and Control Characteristics of a Flying V Scaled Model," Master's thesis, TU Delft, 2019. URL http://resolver.tudelft.nl/uuid:6286f9e2-c24a-430c-a4fa-9fb67b9558b4.

[5] Cappuyns, T., "Handling Qualities of a Flying V Configuration," Master's thesis, TU Delft, 2019. URL http://resolver.tudelft.nl/uuid:69b56494-0731-487a-8e57-cec397452002.

[6] Horwitz, J., "Parametric Design of the Flying-V Winglets for Improved Lateral-Directional Stability and Control," Master's thesis, TU Delft, 2021. URL http://resolver.tudelft.nl/uuid:d7513b36-b9fd-4f8a-8726-f5c7ee7f3a6b.

[7] van Overeem, S., "Modelling, Control, and Handling Quality Analysis of the Flying-V," Master's thesis, TU Delft, 2021. URL http://resolver.tudelft.nl/uuid:7fd04eec-41d4-4967-b246-89fdfac2446e.

[8] Smith, P., "A simplified approach to nonlinear dynamic inversion based flight control," *23rd Atmospheric Flight Mechanics Conference*, American Institute of Aeronautics and Astronautics, 1998. https://doi.org/10.2514/6.1998-4461.

[9] Wang, X., van Kampen, E.-J., Chu, Q., and Lu, P., "Stability Analysis for Incremental Nonlinear Dynamic Inversion Control," *Journal of Guidance, Control, and Dynamics*, Vol. 42, No. 5, 2019, pp. 1116–1129. https://doi.org/10.2514/1.G003791.

[10] Sieberling, S., Chu, Q. P., and Mulder, J. A., "Robust Flight Control Using Incremental Nonlinear Dynamic Inversion and Angular Acceleration Prediction," *Journal of Guidance, Control, and Dynamics*, Vol. 33, No. 6, 2010, pp. 1732–1742. https://doi.org/10.2514/1.49978, URL https://doi.org/10.2514/1.49978.

[11] van Overeem, S., Wang, X., and Kampen, E.-J. V., "Modelling and Handling Quality Assessment of the Flying-V Aircraft," *MST-05, Modeling and Simulation of Air and Space Vehicle Dynamics, Systems, and Environments I, January 4*, AIAA SciTech 2022, 2021. https://doi.org/10.2514/6.2022-1429.

[12] Garcia, A. R., Vos, R., and de Visser, C., "Aerodynamic Model Identification of the Flying V from Wind Tunnel Data," *AIAA AVIATION 2020 FORUM*, 2020. https://doi.org/10.2514/6.2020-2739.

[13] Matamoros, I., and de Visser, C. C., "Incremental Nonlinear Control Allocation for a Tailless Aircraft with Innovative Control Effectors," *2018 AIAA Guidance, Navigation, and Control Conference*, AIAA, 2018. https://doi.org/10.2514/6.2018-1116, URL https://arc.aiaa.org/doi/abs/10.2514/6.2018-1116.

[14] European Union Aviation Safety Agency, "Type-Certificate Data Sheet No. E.111 for Trent XWB Series Engines," , 2019. URL https://www.easa.europa.eu/document-library/type-certificates/engine-cs-e/easae111.

[15] van 't Veld, R., Kampen, E.-J. V., and Chu, Q. P., "Stability and Robustness Analysis and Improvements for Incremental Nonlinear Dynamic Inversion Control," *2018 AIAA Guidance, Navigation, and Control Conference*, 2018. https://doi.org/10.2514/6.2018-1127, URL https://arc.aiaa.org/doi/abs/10.2514/6.2018-1127.

[16] Stevens, B. L., Lewis, F. L., and Johnson, E. N., *Aircraft Control and Simulation: Dynamics, Controls Design, and Autonomous Systems*, John Wiley & Sons, Ltd, 2015. https://doi.org/https://doi.org/10.1002/9781119174882.ch7.

[17] Grondman, F., Looye, G., Kuchar, R. O., Chu, Q. P., and Kampen, E.-J. V., "Design and Flight Testing of Incremental Nonlinear Dynamic Inversion-based Control Laws for a Passenger Aircraft," *2018 AIAA Guidance, Navigation, and Control Conference*, AIAA, 2018. https://doi.org/10.2514/6.2018-0385, URL https://arc.aiaa.org/doi/abs/10.2514/6.2018-0385.

[18] Li, M., Li, J., Tang, Y., and Sun, S., "An Extended INDI Approach and Application to Pitch Rate Control Laws Design of an Aircraft," *AIAA AVIATION 2021 FORUM*, AIAA, 2021. https://doi.org/10.2514/6.2021-3005.

[19] Durham, W., Bordignon, K. A., and Beck, R., *Aircraft Control Allocation*, John Wiley & Sons, 2017. URL https://app.knovel.com/hotlink/khtml/id:kt011B38E1/aircraft-control-allocation/direct-allocation.

[20] Lombaerts, T., Looye, G., Ellerbroek, J., and Martin, M. R. y., "Design and Piloted Simulator Evaluation of Adaptive Safe Flight Envelope Protection Algorithm," *Journal of Guidance, Control, and Dynamics*, Vol. 40, No. 8, 2017, pp. 1902–1924. https://doi.org/10.2514/1.G002525.

[21] Favre, C., "Fly-by-wire for commercial aircraft: the Airbus experience," *International Journal of Control*, Vol. 59, No. 1, 1994, pp. 139–157. https://doi.org/10.1080/00207179408923072.

[22] Delannoy, S., and Oudin, S., "Longitudinal control law for modern long range civil aircrafts," *EuroGNC 2013, 2nd CEAS Specialist Conference on Guidance, Navigation & Control*, 2013. URL https://aerospace-europe.eu/media/books/delft-0027.pdf.

[23] Smeur, E. J. J., Chu, Q., and de Croon, G. C. H. E., "Adaptive Incremental Nonlinear Dynamic Inversion for Attitude Control of Micro Air Vehicles," *Journal of Guidance, Control, and Dynamics*, Vol. 39, No. 3, 2016, pp. 450–461. https://doi.org/10.2514/1.G001490.

[24] Oudin, S., "Low Speed Protections for a Commercial Airliner : a Practical Approach," *AIAA Guidance, Navigation, and Control Conference*, American Institute of Aeronautics and Astronautics, 2017. https://doi.org/10.2514/6.2017-1023.

[25] Department of Defense, *MIL-STD-1797A, FLYING QUALITIES OF PILOTED AIRCRAFT*, 1990.

[26] Mansur, M. H., Lusardi, J. A., Tischler, M. B., and Berger, T., "Achieving the Best Compromise between Stability Margins and Disturbance Rejection Performance," *American Helicopter Society 65th Annual Forum*, 2009.

[27] Cook, M. V., *Flight Dynamics Principles: A Linear Systems Approach to Aircraft Stability and Control*, Butterworth-Heinemann, 2013. https://doi.org/10.1016/C2010-0-65889-5.

[28] Falkena, W., "Investigation of practical flight control systems for small aircraft," Ph.D. thesis, TU Delft, 2012. https://doi.org/10.4233/uuid:22554e85-9506-4410-9fb3-9ad6af4b2c8d.

[29] Hodgkinson, J., and Lamanna, W., "Equivalent system approaches to handling qualities analysis and design problems of augmented aircraft," *Guidance and Control Conference*, McDonnel Aircraft Company, 1977. https://doi.org/10.2514/6.1977-1122.

[30] Gibson, J., "Development of a design methodology for handling qualities excellence in fly by wire aircraft," Ph.D. thesis, TU Delft, 1999. URL http://resolver.tudelft.nl/uuid:6b564b35-cb74-436c-8c47-845bfbbb8b4d.

[31] Mitchell, D. G., Hoh, R. H., Aponso, B. L., and Klyde, D. H., "Proposed Incorporation of Mission-Oriented Flying Qualities into MIL-STD-1797A." 1994.

[32] Lambregts, A. A., "Flight Envelope Protection for Automatic and Augmented Manual Control," *Proceedings of the EuroGNC 2013, 2nd CEAS Specialist Conference on Guidance, Navigation & Control*, Council of European Aerospace Societies (CEAS), 2013, pp. 1364–1383.

[33] Puyou, G., and Losser, Y., "Clearance Benchmark for a Civil Aircraft," *Optimization Based Clearance of Flight Control Laws: A Civil Aircraft Application*, edited by A. Varga, A. Hansson, and G. Puyou, Springer Berlin Heidelberg, Berlin, Heidelberg, 2012, pp. 11–36. https://doi.org/10.1007/978-3-642-22627-4_2, URL https://doi.org/10.1007/978-3-642-22627-4_2.

II

Literature Study

This part has been graded previously for the AE4020 Literature Study course

2
Flying-V

In this chapter, research about the flying characteristics of the Flying-V is presented. First, the Layout of the Flying-V is described. After this, some of the flying characteristics are given and finally, an aerodynamic model of the Flying-V is given. The goal of this chapter is to answer research question 1:

> ”What are the challenges associated with the Flying-V in terms of stability and control characteristics?”

2.1. Flying-V layout

The Flying-V was first proposed by Benad [7] in 2015 as a commercial passenger aircraft flying wing, with the Airbus A350-900 as a reference aircraft. The Flying-V was designed to have the same capacity of 315 passengers and a cruise speed of $0.85Ma$ as the Airbus A350-900. Preliminary estimates indicated that the Flying-V would have a 10% higher Lift over drag ratio and a 2% lower mass. [7] The configuration consists of two pressurised cylindrical sections, that are swept back, giving it the V shape.

This design was further iterated on by Faggiano [11], where the design was optimised for cruise conditions at an altitude of $13.000m$. In this research this design was also compared to the NASA Common Research Model, where it was shown that the Flying-V is 25% more aerodynamically efficient at the designed cruise condition. A comparison between the original planform and the one proposed layout by Faggiano can be found in Figure 2.1. The design parameters of the Flying-V can be found in Table 2.1

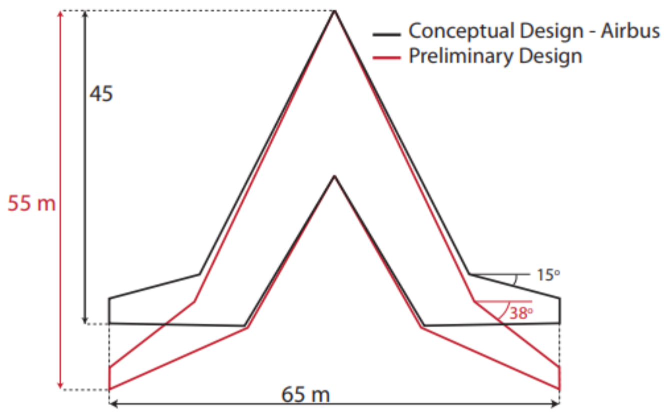

Figure 2.1: Flying-V planform comparison [11]

The engines of the Flying-V are located on the top of the wing, as can be seen in Figure 2.2. For control surfaces, there are three elevons on the trailing edge of the wing on both sides, and a rudder

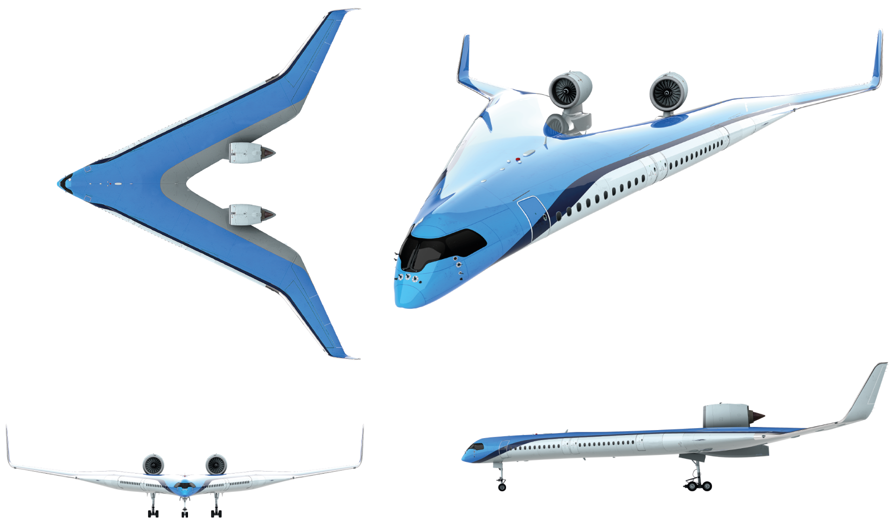

Figure 2.2: Renders Flying-V TU Delft, 28 October 2021, https://www.tudelft.nl/en/ae/flying-v

is integrated into the winglet. There are multiple control surface layouts for the Flying-V that are used. Palermo [29] and Garcia [14] use the following layout: Control surface one (CS1) is the most inboard elevon, and is primarily used as the main elevator, Control surface two (CS2), the centre elevon is used for longitudinal and lateral control, and the outer control surface, CS3, is mainly used for lateral control. However, Cappuyns [8] uses a layout with two elevons, where the inner is used for longitudinal control and the outer for lateral control and a rudder for lateral control. The aerodynamic model used in this report uses the layout of Cappuyns.

Parameter	**Value**	**Unit**
Length	55	$[m]$
Wingspan	65	$[m]$
Height	17	$[m]$
Max. Passengers	314	[-]
Fuel capacity	$140,000$	$[l]$
Cargo capacity	160	$[m^3]$
Design Mach number	0.85	$[-]$
Cruise altitude	$43,000$	$[ft]$

Table 2.1: Design Parameters for Flying-V conceptual design [8]

2.2. Stability and Control characteristics

To determine the stability and control characteristics of the Flying-V, first wind tunnel experiments were conducted. Vliet [40] accessed the flight characteristics of the Flying-V for approach speed and high angles of attack. It was concluded that the aircraft showed unstable behaviour when the angle of attack is larger than $20°$. The range of the center of gravity for trimmable flight was also found, as well as the stall and approach speed. The center of gravity for the sub-scale model was found to be bound between 1.345 and 1.425 meters to be trimmable. This gives it a static margin of about 9%. Palermo [29] determined that the Flying V is trimmable for angles of attack up to $20°$. Palermo also found that the Flying-V has pitch break up tendencies at an angle of attack above $20°$ and that the control surface deflections does not influence the angle of attack where this happens, as can be seen in Figure 2.3. The control surface deflections shift the aerodynamic centre with about 6% of the chord length. It was also determined that the maximum lift coefficient in landing conditions equals 0.66.

In the report of Johnson [20], it was found that rudder deflections decrease the lift coefficient by a

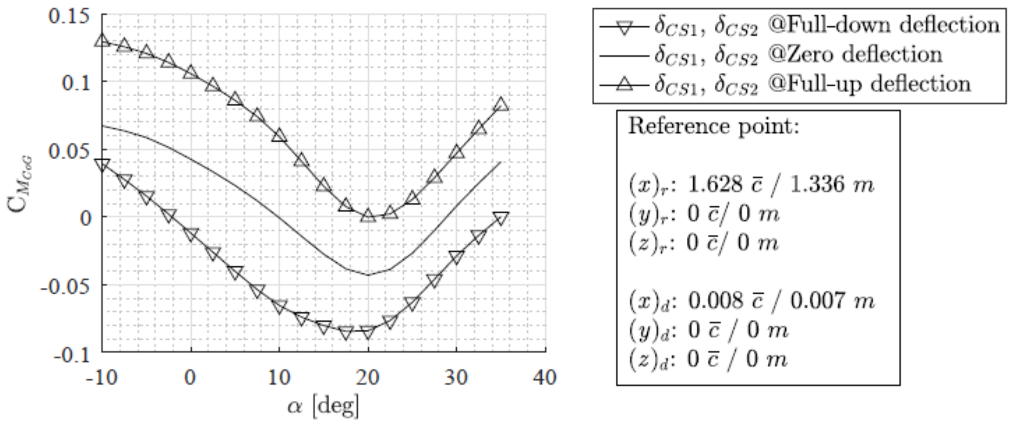

Figure 2.3: Moment coefficient with the centre of gravity at an optimal position [29]

maximum of 0,0024 and increase the drag by the same amount. Johnson also found that the Flying-V does not encounter control reversal. Positive and negative rudder deflections oppositely affect the rolling moment until higher angles of attack.

Horwitz [18] found that with the in the report proposed winglet geometry the Flying-V exhibits strong lateral and satisfactory directional stability. The target value for the yawing moment due to rudder deflections was not met in any configuration, meaning it has less directional control than desired. A Yaw damper in closed-loop control might be required to ensure certifiable departure and dutch roll performance.

Van Empelen [10] looked at the influence of engine integration on the aerodynamic properties. An increased pitch down moment is observed between angles of attack between $5°$ and $12°$. If the angle of attack increases to $12.5°$ until $25°$ a nose-up pitching moment is observed. There is also a small effect on the required control surface deflection for trimming the aircraft, with about $2.5°$.

Cappuyns [8] looked at the handling qualities of the Flying-V, for which the Vortex Lattice Method was used to get the aerodynamic coefficients. It was concluded that the dutch roll was unstable, especially in approach conditions, as well as having limited lateral directional controllability in case of one engine inoperative conditions at low speed. Van Overeem [28] used the research of Cappuyns and also looked at the handling qualities of the Flying-V, and proposed an INDI controller with an outer loop NDI controller to improve the Handling qualities. This controller will be further elaborated on in chapter 4. This research looked at cruise and approach flying conditions. For the analysis of this FCS different effects, as nuisance dynamics and sensor delay was not yet taken into account.

2.3. Aerodynamic model

To be able to simulate the behaviour of the Flying-V, an aerodynamic model is necessary. Van Overeem [28] proposed a combination of two different data sets, to have an aerodynamic model which captures the control and stability characteristics of the Flying-V. In this section this aerodynamic model is explained.

2.3.1. Different models

Garcia [14] used the work of Palermo [29] and Vliet [40] to make an aerodynamic model of the Flying-V scale model. In this work the aerodynamic coefficients were determined. The longitudinal coefficients with respect to the airspeed, angle of attack and elevon deflections were determined. For the lateral coefficients, zero sideslip was assumed. The coefficients were determined for angle of attack values between, as can be seen in Figure 2.4

The unstable dutch roll behaviour is only obtained from the model obtained by use of the Vortex Lattice Method (VLM) [8], where the pitch break tendencies for angles of attack larger then 20 degrees are observed from the Wind Tunnel Experiments [14]. To get a model that has captures both unwanted aerodynamic behaviours Overeem suggests a combination of both models [28]. The VLM model has the Aerodynamic coefficients for angles of attack in the range of $0°$ to $15°$ for cruise and approach

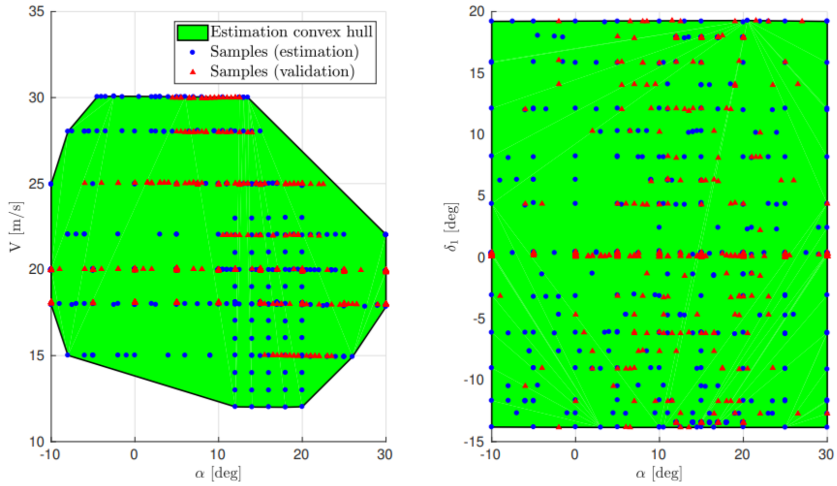

Figure 2.4: Convex hull of the estimation dataset (α − V and α − δ_1 cuts)

conditions. The coefficients are all defined as in Equation 2.1, where C_* is either C_X, C_Y, C_Z, C_m, C_n or C_l, p^*, p^* and p^* are calculated with Equation 2.2 [8].

$$C_* = C_{*_\alpha}(\alpha) + C_{*_\beta}(\beta) + C_{*_{p^*}}(p^*) + C_{*_{q^*}}(q^*) + C_{*_{r^*}}(r^*) + C_{*_{\delta_{CS1}}}(\delta_{CS1}) + C_{*_{\delta_{CS2}}}(\delta_{CS2}) + C_{*_{\delta_{CS3}}}(\delta_{CS3}) \tag{2.1}$$

$$p^* = p\frac{c}{V}, q^* = q\frac{c}{V}, r^* = r\frac{c}{V} \tag{2.2}$$

For the wind tunnel experiment (WTE) model, the equations as in Equation 2.3 are used. Because of the high uncertainty of the C_Y coefficient, this coefficient will not be used from this dataset, but only from the VLM model.

$$\begin{aligned}
C_X &= C_{X_0} + C_{X_\alpha}\alpha + C^2_{X_{\alpha^2}}\alpha^2 + C_{X_{\alpha^3}}\alpha^3 + C_{X_{\alpha^4}}\alpha^4 + C_{X_{\delta_{CS1}}}\delta_{CS1} + C_{X_{\delta_{CS2}}}\delta_{CS2} + C_{X_{\delta_{CS3}}}\delta_{CS3} \\
&\quad + C_{X_{\delta^2_{CS1}}}\delta^2_{CS1} + C_{X_{\delta^2_{CS2}}}\delta^2_{CS2} + C_{X_{\hat{V}}}\hat{V} + C_{X_{\hat{V}^2}}\hat{V}^2 \\
C_Z &= C_{Z_0} + C_{Z_\alpha}\alpha + C^2_{Z_{\alpha^2}}\alpha^2 + C_{Z_{\alpha^3}}\alpha^3 + C_{Z_{\delta_{CS1}}}\delta_{CS1} + C_{Z_{\delta_{CS2}}}\delta_{CS2} + C_{Z_{\delta_{CS3}}}\delta_{CS3} + C_{Z_{\hat{V}}}\hat{V} \\
C_l &= C_{l_0} + C_{l_\alpha}\alpha + C_{l^2_\alpha}\alpha^2 + C_{l^3_\alpha}\alpha^3 + C_{l^4_\alpha}\alpha^4 + C_{l_{\delta_{CS1}}}\delta_{CS1} + C_{l_{\delta_{CS2}}}\delta_{CS2} + C_{l_{\delta_{CS3}}}\delta_{CS3} + C_{l_{\hat{V}}}\hat{V} \\
C_m &= C_{m_0} + C_{m_\alpha}\alpha + C_{m^2_\alpha}\alpha^2 + C_{m^3_\alpha}\alpha^3 + C_{m^4_\alpha}\alpha^4 + C_{m_{\delta_{CS1}}}\delta_{CS1} + C_{m_{\delta_{CS2}}}\delta_{CS2} + C_{m_{\delta_{CS3}}}\delta_{CS3} \\
&\quad + C_{m_{\delta^2_{CS1}}}\delta^2_{CS1} + C_{m_{\delta^2_{CS2}}}\delta^2_{CS2} + C_{m_{\delta_{CS1}\delta_{CS2}}}\delta_{CS1}\delta_{CS2} + C_{m_{\alpha\delta^2_{CS1}}}\alpha\delta^2_{CS1} + C_{m_{\alpha\delta^2_{CS2}}}\alpha\delta^2_{CS2} \\
&\quad + C_{m_{\alpha^2\delta_{CS1}}}\alpha^2\delta_{CS1} + C_{m_{\alpha^2\delta_{CS2}}}\alpha^2\delta_{CS2} + C_{m_{\hat{V}}}\hat{V} + C_{m_{\hat{V}\delta_{CS1}}}\hat{V}\delta_{CS1} \\
C_n &= C_{n_0} + C_{n_\alpha}\alpha + C_{n_{\alpha^2}}\alpha^2 + C_{n_{\alpha^3}}\alpha^3 + C_{n_{\alpha^4}}\alpha^4 + C_{n_{\delta_{CS1}}}\delta_{CS1} + C_{n_{\delta_{CS2}}}\delta_{CS2} + C_{n_{\delta^2_{CS1}}}\delta^2_{CS1} + C_{n_{\delta^2_{CS2}}}\delta^2_{CS2} \\
&\quad + C_{n_{\hat{V}}}\hat{V}
\end{aligned} \tag{2.3}$$

2.3.2. Combining VLM and WTE models

There are some differences between both models, that needs to be accounted for, to be able to combine both models. The VLM model is based on the full-scale aircraft, where the WTE data is obtained from a 4.6% scale model [14]. The VLM model is a linear model, where the WTE is nonlinear and the VLM has a different control layout, with two elevons and a rudder integrated into the winglet, where the WTE had three elevons, and no rudder or winglets. The combined model uses the VLM control surface layout.

For the combination of models, the VLM is used as a baseline [28], also meaning that this model will use the control surface layout of the VLM data. As WTE will be used to have the pitch breakup effects in the model, the lateral coefficients will be used from the VLM, and only the longitudinal coefficients will be combined. As the two models are made for different speed regimes Froude scaling needs to be applied [4].

In the combined aerodynamic model, the values for the longitudinal coefficients for angles of attack in the range of $[-5° - 15°]$ are from the VLM model, where the values for angles of attack in the range $[15° - 30°]$ are from the WTE model. As this model does not include zero lift drag, the zero lift drag from the Airbus A350-900 was added [28].

2.3.3. Assumptions

For the design of the aerodynamic model, a number of assumptions were made, that limits the usability of the model. An overview of the assumptions for the model:

1. Only the angle of attack contributes non-linearly to the force and moment coefficients, where in reality the other components, such as the control surface deflections, will also have a non-linear contribution, limiting the fidelity of the contribution of these components. [28]
2. To combine the VLM and WTE models Froude scaling was applied. For this it is required that the relative density factor and moment of inertia must be the same, which was not the case, leading to inaccuracies in the combined model [14].
3. As the VLM model is used as a baseline model, the combined model does not include frictional drag [8]. Due to scaling it is not possible to obtain an estimate from the WTE model, therefore the combined model uses the frictional drag from the Airbus A350-900 [28].
4. The influences of the Earth's curvature and angular velocity are neglected. When the flight time of the simulation is short, this will have a negligible effect, but it can introduce large errors for longer flight times.
5. The gravity vector is assumed to be constant, where in reality it changes depending on the place on Earth, as the Earth has no constant mass distribution.
6. For the simulation zero wind is assumed, with an atmosphere that corresponds to the International Standard Atmosphere. [28]

2.4. Conclusion

In this chapter, an overview of research into the Flying-V was given. The layout of the Flying-V was also described, as well as an aerodynamic model for the Flying-V.

Also, an answer was found to research question 1, "What are the current challenges in controlling the Flying-V?" The Flying-V has an unstable dutch roll and has pitch break up tendencies when the angle of attack is larger than twenty degrees. For this van Overeem proposed an INDI controller, however, this controller was not tested yet in high angle of attack conditions, and the influence of some effects that change the robustness of a controller was not yet taken into account.

3

Incremental Nonlinear Dynamic Inversion

This chapter gives the background of Incremental Nonlinear Dynamic Inversion control. After the derivation of Nonlinear Dynamic Inversion and INDI are given, current developments on INDI is given, answering research question 2:

> ”What is the state of the art in INDI flight control?”

After this different uncertainties that influence the robustness of controllers are presented.

3.1. Nonlinear Dynamic Inversion

Nonlinear Dynamic Inversion, sometimes also called feedback linearization, was developed to eliminate the need for gain scheduling and to improve performance.

For NDI it is assumed that the equations of motion can be described by Equation 3.1, where $\boldsymbol{x}$ is the state vector $(n \times 1)$, $\boldsymbol{u}$ the input vector $(m \times 1)$, $\boldsymbol{y}$ the output vector $(m \times 1)$, $\boldsymbol{f}$ and $\boldsymbol{h}$ are smooth vector fields and G is a $(n \times m)$ matrix with smooth vector fields as columns.

$$\begin{aligned} \dot{\boldsymbol{x}} &= f(\boldsymbol{x}) + G(\boldsymbol{x})\boldsymbol{u} \\ \boldsymbol{y} &= h(\boldsymbol{x}) \end{aligned} \tag{3.1}$$

To find the NDI control law, the output equation is differentiated, which leads to Equation 3.2, in which $L_f h(\mathbf{x})$ is the Lie derivative defined as $\nabla h(\boldsymbol{x}) f(\boldsymbol{x})$ and $L_g h(\boldsymbol{x})$ the Lie derivative along $G(\mathbf{x})$. [42]

$$\frac{dh(\boldsymbol{x})}{dt} = L_f h(\boldsymbol{x}) + L_g h(\boldsymbol{x})\boldsymbol{u} \tag{3.2}$$

If $L_g h(\boldsymbol{x})$ is not equal to 0 for any $\mathbf{x}$, a control law can be formulated as in Equation 3.3, where the relation between the input and output is in Equation 3.4

$$\boldsymbol{u} = L_g h(\boldsymbol{x})^{-1}[v - L_f h(\boldsymbol{x})] \tag{3.3}$$

$$\dot{\boldsymbol{y}} = \boldsymbol{v} \tag{3.4}$$

If $L_g h(\mathbf{x})$ is equal to zero, the output is differentiated until the moment that there specific relation between control input and output vector, which results in the following general equation Equation 3.5.

$$\boldsymbol{y}^{(i)} = L_f^i \boldsymbol{h}(\boldsymbol{x}) + L_G L_f^{i-1} h(\boldsymbol{x})\boldsymbol{u} \tag{3.5}$$

If the output vector is equal to the state vector, the relation in Equation 3.6 can be obtained.

$$\begin{aligned} \dot{\boldsymbol{y}} &= \dot{\boldsymbol{x}} \\ \dot{\boldsymbol{y}} &= f(\boldsymbol{x}) + G(\boldsymbol{x})\boldsymbol{u} \end{aligned} \tag{3.6}$$

If $G(\mathbf{x})$ is invertible, a control input that cancels the nonlinear system dynamics can be found with Equation 3.7.

$$\boldsymbol{u} = G(\boldsymbol{x})^{-1}(\boldsymbol{v} - f(\boldsymbol{x})) \tag{3.7}$$

As this control law give a linear relation between the output and the virtual input, the virtual input can be made with the use of linear control techniques. In Figure 3.1 a layout for a closed-loop system with a NDI controller can be found.

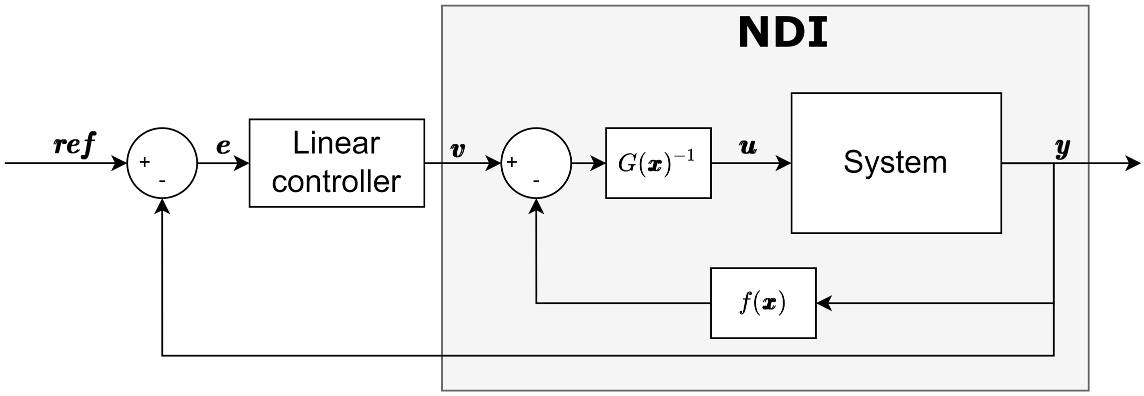

Figure 3.1: Nonlinear Dynamic Inversion controller

3.2. Incremental Nonlinear Dynamic Inversion

One of the problems with NDI is that it is sensitive to model inaccuracies. To solve this, Incremental Nonlinear Dynamic Inversion (INDI) was developed. This version of NDI was initially also known as Simplified Nonlinear Dynamic Inversion. [37]. The general system is the same as for the NDI derivation in Equation 3.5.

To get the incremental form of this equation, Taylor series expansion is applied, where second derivatives and higher terms are neglected in Equation 3.8 [32].

$$\begin{aligned} \dot{\boldsymbol{x}} &\approx \dot{\boldsymbol{x}}_0 + \frac{\partial}{\partial \boldsymbol{x}}[\boldsymbol{f}(\boldsymbol{x}) + G(\boldsymbol{x})\boldsymbol{u}]_{\boldsymbol{u}_0,\boldsymbol{x}_0}(\boldsymbol{x} - \boldsymbol{x}_0) + \frac{\partial}{\partial \boldsymbol{u}}[\boldsymbol{f}(\boldsymbol{x}) + G(\boldsymbol{x})\boldsymbol{u}]_{\boldsymbol{u}_0,\boldsymbol{x}_0}(\boldsymbol{u} - \boldsymbol{u}_0) \\ &= \dot{\boldsymbol{x}}_0 + \frac{\partial}{\partial \boldsymbol{x}}[\boldsymbol{f}(\boldsymbol{x}) + G(\boldsymbol{x})\boldsymbol{u}]_{\boldsymbol{u}_0,\boldsymbol{x}_0}(\Delta \boldsymbol{x}) + G(\boldsymbol{x}_0)(\Delta \boldsymbol{u}) \end{aligned} \tag{3.8}$$

If the sample rate is high enough, time scale separation can be applied, as surface deflections are assumed to be faster than the aircraft dynamics. With this assumption $\Delta\boldsymbol{x}$ will be zero, leading to Equation 3.9

$$\dot{\boldsymbol{x}} \approx \dot{\boldsymbol{x}}_0 + G(\boldsymbol{x}_0)\Delta\boldsymbol{u} \tag{3.9}$$

Inverting this leads to Equation 3.10, which then gives the control law in Equation 3.11.

$$\Delta\boldsymbol{u} = G^{-1}(\boldsymbol{x}_0)(\boldsymbol{v} - \dot{\boldsymbol{x}}_0) \tag{3.10}$$

$$\boldsymbol{u} = \boldsymbol{u}_0 + G^{-1}(\boldsymbol{x}_0)(\boldsymbol{v} - \dot{\boldsymbol{x}}_0) \tag{3.11}$$

A block diagram of an INDI controller is in Figure 3.2.

When comparing Equation 3.7 with Equation 3.11, the main difference is that the NDI control law depends directly on the knowledge of the dynamics of the system, due to the $f(\boldsymbol{x})$ part of the equation. However, the INDI controller will be dependent on the accuracy of the measurements of $\boldsymbol{u}_0$ and $\boldsymbol{x}_0$

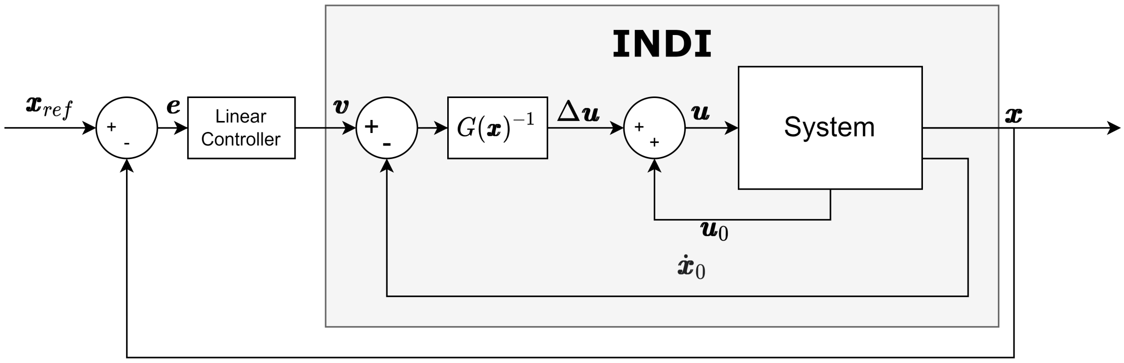

Figure 3.2: Incremental Nonlinear Dynamic Inversion controller. Adapted from [42]

3.3. State of the art

INDI is a relatively new control technique, that was first formulated in the 90's when it was still called Simplified NDI [37]. Smith and Berry [38] in 2000 applied INDI to the Harrier aircraft, where it was performing well for higher speeds, but at transitional and hovering conditions it worked less, as it developed oscillatory behaviour.

One of the challenges for INDI is that it requires measurements of the angular accelerations. In 2000 Bacon and Ostroff [5] proposed a way to get the angular accelerations with differentiated angular velocity and three angular rate measurements. In a following research a washout filter was used in combination with the measurements, as the differentiation introduces noise [6]. Sieberling [32] in 2010 presented an INDI implementation, where a linear predictive filter was used to obtain the angular accelerations, which also compensates for signal delay.

Kumtepe [22] and Kim [21] propose a Hybrid INDI, which combines the normal sensor-based INDI, with a model-based control system. Measurement delays, which are a main challenge for normal INDI, can be compensated by using this Hybrid version. One of the drawbacks is the noise filtering capability of Hybrid INDI. A trade-off between noise filtering and response time has to be made for good performance.

Lu [24] looks at an INDI aircraft trajectory controller in the presence of model uncertainties and actuator faults. This controller is compared with a NDI controller with model identification. The INDI controller is shown to be more robust to model uncertainties. In 2019 Wang et al. [42] reformulate INDI so it can be used without time scale separation, and a stability and robustness analysis is applied, with a comparison with NDI, where it is shown that INDI is more robust.

Simplicio [33] combined INDI with Pseudo Control Hedging (PCH). PCH automatically changes the signal sent to the controller by an estimated amount to compensate for actuator dynamics. This prevents wind up when the control surface deflections are saturated.

The first application of INDI on a CS25-certified aircraft was done by Grondman et al. [16], who tested an INDI controller on the Cessna Citation II. Van 't Veld [1] first looked at what practical problems would be for applying the INDI to the Citation, and suggested solutions for possible problems with the Fly By Wire system. Also it was proposed to use PCH to prevent actuator saturation, which was used by Grondman et al. The proposed INDI controller with PCH by van 't Veld can be seen in Figure 3.3. The controller consists of an angular rate inner loop based on INDI, and a attitude outer loop consisting of roll, pitch and sideslip angle. The first part of the PCH is a first-order reference model, which is the RM in the figure. The reference model imposes the desired dynamics on the output, with Equation 3.12 and Equation 3.13.

$$\boldsymbol{v}_{rm} = K_{rm}(\boldsymbol{\omega}_c - \boldsymbol{\omega}_{rm}) \tag{3.12}$$

$$\boldsymbol{\omega}_{rm} = \frac{\boldsymbol{v}_{rm} - \boldsymbol{v}_h}{s} \tag{3.13}$$

The RM also provides the derivative of the command signal, $\boldsymbol{v}_{rm}$. The RM is then changed to an actually achievable level by the command hedge $\boldsymbol{v}_h$ as defined as in Equation 3.14

$$\boldsymbol{v}_h = G(\boldsymbol{x}_{k-1}, \boldsymbol{u}_{k-1})(\boldsymbol{u}_{ck} - \boldsymbol{u}_k) \tag{3.14}$$

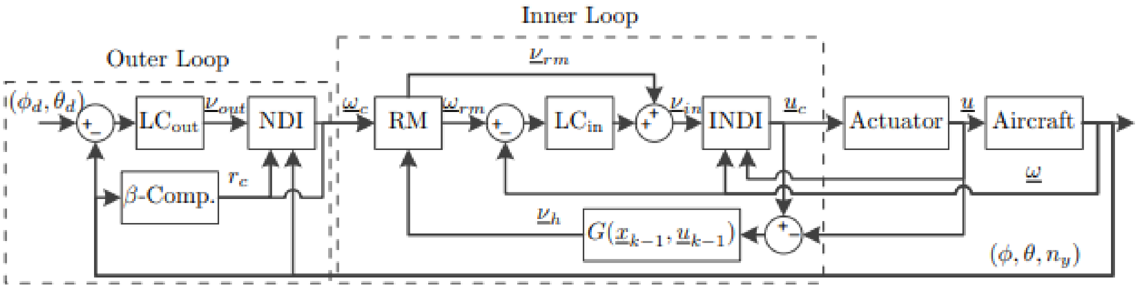

Figure 3.3: Proposed Attitude controller structure based on NDI, INDI and PCH by van 't Veld [1]

Smeur [34] proposed an adaptive INDI FCS, which is able to handle changes in control effectiveness. Smit [36] in 2021 suggests multiple adaptive INDI control techniques. After investigation it was concluded that the LMS parameter estimation shows to have the most potential, and it is shown that this approach decreases the variation in Handling quality and stability. Smit [36] also uses a command filter which is applied directly, in combination with a PI compensator, instead of the linear controller as shown in Figure 3.2. With this method the controller follows the input accurately while being more robust to perturbations. A block diagram of Smits controller can be found in Figure 3.4.

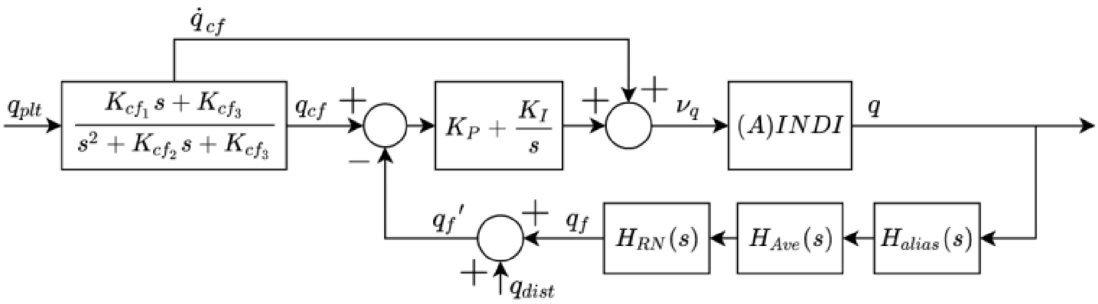

Figure 3.4: Adaptive INDI control system block scheme including pitch rate disturbance input location [36]

Jayaraman et al. [19] compares NDI with INDI for a lightweight aircraft, where INDI was shown to have better performance.

In 2021 Li et al. [23] proposed a novel INDI based flight control strategy, with the name angular acceleration estimation-based INDI (EINDI). This method combines an adaptive technique with control surface deflections to estimate the angular accelerations. This would reduce the influence of sensor noise and time delay, making the method more robust. The method was also capable of overcoming cg shifts and a number of model inaccuracies.

The combination of INDI and flying wing aircraft also has been investigated. Zhang et al. [44] and Zhang and Meng [45] propose a two-loop attitude control scheme for flying wing aircraft with actuator faults. To prevent actuator saturation an optimal anti-windup compensator is introduced. Simulations indicate that this is a valid and effective proposal and that INDI is able to deal with the nonlinearities of the flying wing aircraft that were investigated. It was also found that the INDI control law was able to handle the coupled control surfaces. Jiannan Zhang et al. [43] looked at the performance of INDI for aircraft with highly redundant control surfaces, it was shown that the controller had sufficient tracking performance and was able to fully utilise the control power.

When looking at all the research that has been done on INDI, it becomes clear that the first main challenge in a practical implementation of INDI control laws was to get the angular accelerations. After this research was done on how to deal with control surface saturation, and in showing the robustness of INDI. From this research, it can be concluded that INDI control laws have robustness against external disturbances and model inaccuracies while having high performance. The previous research on INDI with flying wings is also promising for the use of INDI control laws on the Flying-V. The ability to deal with coupled control surfaces of INDI control laws could also be useful for the Flying-V.

3.4. Robustness

The robustness of a Flight Control System is the ability of the system to deal with uncertainties. These uncertainties can be, for example, model inaccuracies or time delay. Another influence on the Robustness of a control law can be the sampling frequency. The ability of a FCS to reject disturbances can also be seen as part of robustness.[42]

3.4.1. Model inaccuracies

Sieberling [32] looked at the influence of model uncertainties on INDI. If model uncertainties are present, the system response is no longer represented by Equation 3.9, but with Equation 3.15.

$$\dot{\boldsymbol{x}} = \dot{\boldsymbol{x}}_0 + G(\boldsymbol{x}_0)\Delta\boldsymbol{u} + \Delta G(\boldsymbol{x}_0)\Delta\boldsymbol{u} \tag{3.15}$$

When filling in the control law of INDI in Equation 3.15, will lead to Equation 3.16

$$\begin{aligned}\dot{\boldsymbol{x}} &= \dot{\boldsymbol{x}}_0 + G(\boldsymbol{x}_0)G^{-1}(\boldsymbol{x}_0)(\boldsymbol{v} - \dot{\boldsymbol{x}}_0) + \Delta G(\boldsymbol{x}_0)G^{-1}(\boldsymbol{x}_0)(\boldsymbol{v} - \dot{\boldsymbol{x}}_0)\\ \dot{\boldsymbol{x}} &= \left(I + \Delta G(\boldsymbol{x}_0)G^{-1}(\boldsymbol{x})\right)\boldsymbol{v} - \Delta G(\boldsymbol{x}_0)G^{-1}(\boldsymbol{x}_0)\dot{\boldsymbol{x}}_0\end{aligned} \tag{3.16}$$

When ideal sensor measurements and small sampling time can be assumed that the new and current state derivatives are approximately equal. With this assumption, the equation can be simplified to Equation 3.17 [33].

$$(I + \Delta G(\boldsymbol{x}_0)G^{-1}(\boldsymbol{x}_0))\dot{\boldsymbol{x}} \approx (I + \Delta G(\boldsymbol{x}_0)G^{-1}(\boldsymbol{x}_0))\boldsymbol{v} \tag{3.17}$$

From this, it can be concluded that the system response with model inaccuracies is approximately equal to the response without the model inaccuracies. However, this approximation is only valid with a small enough sampling time, and ideal sensor measurements [1].

Van 't Veld [1] also looked at the relation between control effectiveness uncertainty and sampling frequency. For the analysed system the stable region can be seen in Figure 3.5. The uncertainty ratio γ is calculated with Equation 3.18

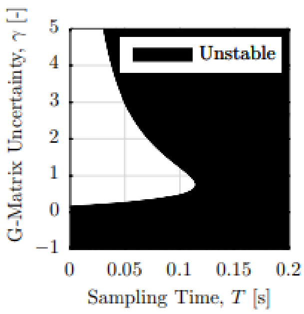

Figure 3.5: Stability of analysed system with control effectiveness uncertainty by van 't Veld [1]

$$\gamma = \frac{G}{G + \Delta G} \tag{3.18}$$

From the figure it can be seen that the uncertainty can be quite large if the sampling frequency is small enough.

Another form of model uncertainties are unmodeled dynamics. This could be for example aeroelastic effects that were not taken into account [12]. There are multiple common ways to describe the deviation from the nominal model G_m in an aggregation of multiple model inaccuracies. Three of these ways can be seen in Equation 3.19 [2].

$$\begin{aligned} \text{Additive perturbation } G &= G_n + \Delta_m \\ \text{Multiplicative perturbation } G &= G_n(1+\Delta_m) \\ \text{Feedback perturbation } G &= \frac{G_n}{1+G_n\Delta_m} \end{aligned} \tag{3.19}$$

Most of the time, the low-frequency behaviour of a control system is mostly influenced by uncertain physical parameters, whereas higher frequencies are more influenced by unmodeled dynamic uncertainties [2].

Pollack [30] gives an analysis of the effect of unmodeled dynamics on INDI. It was concluded that the upper bound of the error goes to zero, when the $\mathcal{L}_2$ gain of the causal perturbations $\boldsymbol{\Delta}_i$ goes to zero. However, this is only the case when actuator dynamics and sampling frequency is not taken into account. It is also stated that the norm of the INDI error will be small when the time-scale separation assumption is valid.

3.4.2. Time delay and lag

Time delay can be introduced by sensors and actuators or by a fly-by-wire system [12]. Choices made for the control design can introduce lag, as filters are used [35]. The difference between lag and time delay, is that with time delay the signal is not changed, but only delayed, where with lag, the signal changes in shape, as it takes more time to go to the final value.

A difference in delay between the state derivative and actuator position has negative effects on the controllers performance [32]. To counter act this a predictive filter can be used [12], which has the downside that this filter needs to be trained, and the filter is influenced by noise. A simpler first or second order filter can be used, but this introduces artificial delays to the system [1], Smeur [35] proved that by applying a similar filter to the gyro and actuator measurements the delays will become synchronised. When the signals are synchronised, the impact on the performance is minimised.

3.4.3. Noise

The ability of dealing with random disturbances is an important part of control robustness. This noise can either be introduced by atmospheric disturbances or sensor noise from measured feedback signals. Lu [24] and Wang [42] proved that INDI has better disturbance rejection capabilities then NDI, without the use of any additional robust or adaptive techniques. However INDI is still sensitive to noise in the form of sensor noise, as the control law is dependent on the measured angular accelerations.

3.4.4. Sampling frequency

A high sampling frequency is required for INDI, to ensure that $\boldsymbol{x} \approx \boldsymbol{x}_0$ [33]. The high sampling frequency is also required to ensure that $\dot{\boldsymbol{x}} \approx \boldsymbol{v}$ when model inaccuracies are present [1]. The advantage of a lower sampling frequency is that it is computationally less intensive.

3.5. Conclusion

The goal of this chapter was to answer research question 2. From this chapter it can be concluded that a lot of research has been done on INDI. It is shown that INDI shows that FCS based on INDI have high performance, and show good robustness against input perturbations and model uncertainties. There are also different solutions that are proposed to counter some of the possible disadvantages of INDI control. So can PCH help with actuator saturation problems and can hybrid INDI help with problems caused by measurement delays. EINDI could help reduce the influence of sensor noise and time delay. Finally the different effects that influence the robustness of a FCS are given, which is partly answering research question 4a.

4

INDI for the Flying-V

There are multiple ways of measuring the performance of a flight control system. One of these is measuring the tracking performance of the controller, an other way is by looking at the handling qualities of an aircraft. In this chapter some of the requirements of handling qualities that are relevant for the Flying-V are given. Next to that a flight control system for the Flying-V which uses INDI, as proposed by van Overeem [28] is described.

4.1. Handling Qualities of the Flying-V

Handling qualities of an aircraft are defined as a description of the adequacy of the short term dynamic response to controls during the execution of a flight task [9]. To have good handling qualities, the aircraft must have enough control authority to maintain steady, straight, horizontal flight. The aircraft must also be able to go from one steady state to another in a safely manner. Finally, the cockpit control forces should be on an acceptable level [31]. To ensure aircraft are safe to fly, civilian certification authorities have set certain certification criteria on handling qualities. However, these tend to be not very specific [41]. The U.S. Air Force developed their own specifications, which are different for multiple classes of aircraft. The Flying-V falls in class III, as it is a large aircraft with a MTOM which is larger then 30000 kg[8][9] . For each behaviour the aircraft falls into one of three levels, where only level 1 is acceptable during nominal flight, where no faults are present. The requirements for each behaviour also depends on the current flight phase, which is divided in three categories. The different flight phases can be found in Table 4.1. As these requirements were originated from military, not all conditions are relevant for the Flying-V, the relevant conditions are in bold.

4.1.1. Longitudinal Handling Qualities

For the longitudinal handling qualities, the military requirements are divided for the Short period and the Phugoid. Another possible metric are the Gibson Criteria [15]. The dropback criteria puts requirements on the dropback and overshoot ratio of the short period. There are also criteria for flight path delay, maximum pitch rate and time to reach steady state [15].

The Neal-Smith criteria can also be used to assess the longitudinal handling qualities. The Neal-Smith criteria is a mathematical compensator, which models the pilot. The compensator is tuned to achieve a certain bandwidth, while keeping the resonant peak to a minimum. The height of the peak, and the lead compensation of the compensator can be used to predict the workload for the pilot. [26].

Short Period

The short period is the fast oscillating pitch rate transient response of an elevator input. To be able to track a reference signal sufficiently, it is important that this motion is well damped [17]. The quantifiable measurement for how well the response of the aircraft can be anticipated is the Control Anticipation Parameter (CAP) [9]. The CAP can be calculated with Equation 4.1

$$CAP = \frac{\dot{q}}{n_{z_{ss}}} = \frac{\omega_{n_{sp}}^2}{n_\alpha}, n_\alpha = \frac{V}{gT_{\theta_2}} \tag{4.1}$$

Flight phase category	Flight phase
A	Air-to-air combat Ground attack Weapon delivery/launch Reconnaissance In-flight refuel (Reciever) Terrain following Maritime search Aerobatics Close formation flying
B	**Climb** **Cruise** **Loiter** In-flight refuel (tanker **Descent** Aerial delivery
C	**Take off** **Approach** **Overshoot** **Landing**

Table 4.1: Flight phase categories for handling qualities [9]

In Equation 4.1 $\omega_{n_{sp}}$ is the undamped natural frequency of the short period and n_α is the load factor sensitivity of the aircraft. For the calculation of n_α, g is the gravitational acceleration, V the airspeed and T_{θ_2} can be obtained from the short period reduced pitch rate transfer function. [9] If the CAP is too low, the aircraft reacts sluggish on an elevator input, where as if the CAP is too high, it reacts quicker then expected. Cappueyns [8] found that the CAP of the Flying-V for approach and cruise is within level 1 requirements.

Phugoid

The Phugoid is the slow pitch angle and velocity response. During the phugoid the aircraft interchanges potential and kinetic energy, following a sinusoidal path. The phugoid dynamics are of level 1 flying qualities if the damping ratio is at least 0.04 [9].

4.1.2. Lateral Handling Qualities

For the Lateral handling qualities, the flying levels look at the aperiodic roll, spiral mode and dutch roll.

Aperiodic Roll

The aperiodic roll is the quick response of the roll rate to an aileron input, and can be seen as the damping of the roll rate [17]. The minimum time constants for the aperiodic roll can be found in Table 4.2 [9].

Flight phase	Level 1	Level 2	Level 3
Cat A, C	1.0	1.4	10
Cat B	1.4	3.0	10

Table 4.2: Roll mode time constant [s] maximum values [9]

Spiral mode

The spiral mode is a slow developing turning flight, if this mode is stable the aircraft automatically levels after a roll disturbance, otherwise the roll angle increases after a roll disturbance [17]. As this is a slow movement, it is acceptable to be unstable, as long as the doubling time is large enough. For the Flying-V to have level one flying capabilities it should be at least 12 seconds for cruise and 20 for approach conditions [9].

Dutch Roll

The dutch roll is a coupled yaw and roll movement. It starts with a sideslip deviation, which induces a yawing motion, which results, due to aerodynamic coupling, into rolling [17]. the dutch roll is an important factor for the lateral handling qualities. The requirements for level 1 flying qualities are in Table 4.3

Flight phase	ζ_d	$\zeta_d \omega_d$	ω_d
Cat A	0.19	0.35	0.5
Cat B	0.08	0.15	0.5
Cat C	0.08	0.10	0.5

Table 4.3: Dutch roll frequency and Damping minimum values for level 1 flying qualities [9]

4.2. INDI controller

The flight control system for the Flying-V proposed by van Overeem [28] has an inner loop stability augmentation system consisting of an INDI angular rate control and a PID airspeed controller. The INDI controller is based on the rotational equation of motion, which can be found in Equation 4.2, where $\boldsymbol{\omega}$ are the angular rates, $\boldsymbol{I}$ is the inertia matrix and $\boldsymbol{M}$ are the moments acting on the Flying-V.

$$\dot{\boldsymbol{\omega}} = \boldsymbol{I}^{-1}\boldsymbol{M} - \boldsymbol{I}^{-1}(\boldsymbol{\omega} \times \boldsymbol{I}\boldsymbol{\omega}) \tag{4.2}$$

To get $G(\boldsymbol{x})$ Equation 4.2 needs to be differentiated with respect to the control surface deflections, leading to Equation 4.3

$$G(\mathbf{x}) = \frac{\rho V^2 Sc}{2}\boldsymbol{I}^{-1}\begin{bmatrix} C_{l_{\delta_{CS1}}} & C_{l_{\delta_{CS2}}} & C_{l_{\delta_{CS3}}} \\ C_{m_{\delta_{CS1}}} & C_{m_{\delta_{CS2}}} & C_{m_{\delta_{CS3}}} \\ C_{n_{\delta_{CS1}}} & C_{n_{\delta_{CS2}}} & C_{n_{\delta_{CS3}}} \end{bmatrix} \tag{4.3}$$

Using Equation 3.11 the control surface deflections can be calculated with Equation 4.4

$$\mathbf{u} = \mathbf{u}_0 + \frac{2\boldsymbol{I}}{\rho V^2 * S * c}\begin{bmatrix} 0 & C_{l_{\delta_{CS2}}} & 0 \\ C_{m_{\delta_{CS1}}} & 0 & C_{m_{\delta_{CS3}}} \\ C_{n_{\delta_{CS1}}} & 0 & C_{n_{\delta_{CS3}}} \end{bmatrix}^{-1} (\boldsymbol{v} - \dot{\boldsymbol{x}}_0) \tag{4.4}$$

The control effectiveness coefficients that are equal to zero, are in this equation already replaced with zeros. The value of the other coefficient can be found in Table 4.4. These values are obtained from the aerodynamic model described in chapter 2.

Coefficient	$Cruise$	$Approach$
$C_{l_{\delta_{CS2}}}$	0.0081	0.0061
$C_{m_{\delta_{CS1}}}$	−0.0042	0.0034
$C_{m_{\delta_{CS3}}}$	−0.0009	−0.0006
$C_{n_{\delta_{CS1}}}$	0.0005	0.0005
$C_{n_{\delta_{CS3}}}$	−0.0013	−0.0011

Table 4.4: Control effectiveness coefficients

As Control surface 1 (The inner elevon) will only be used for pitch control, and Control surface 3 (The rudder) only for yaw control, $C_{m_{\delta_{CS3}}}$ and $C_{n_{\delta_{CS1}}}$ will be set to zero in the controller.

A block diagram of the inner control loop can be found in Figure 4.1.

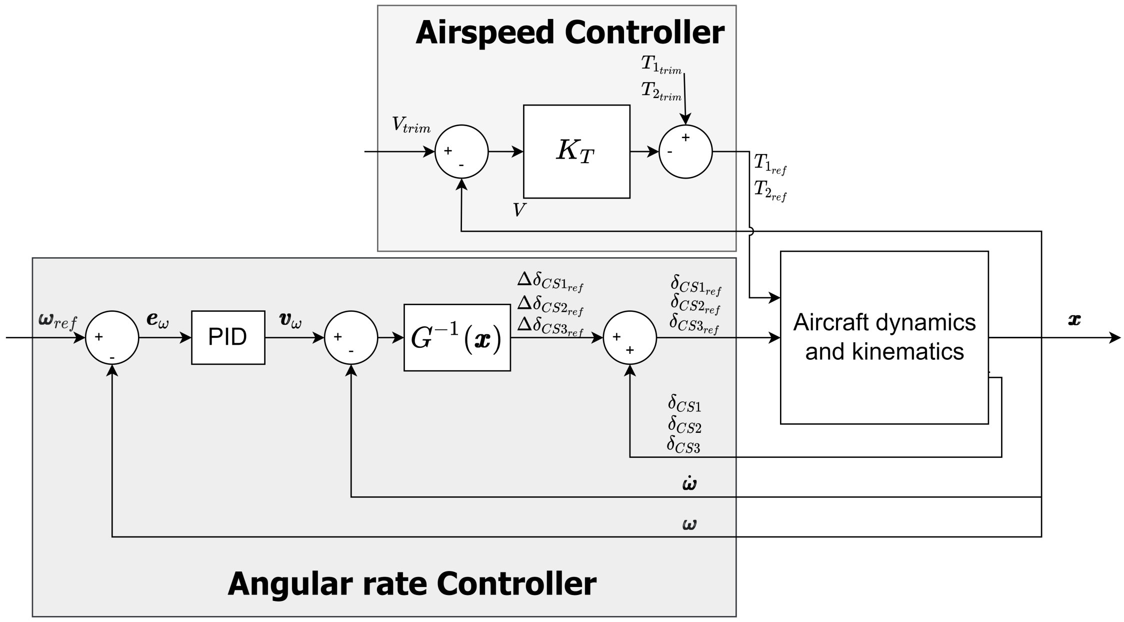

Figure 4.1: Flying-V inner control loops adapted from [28]

4.3. Flight path angle controller

The outer loop of the controller is a control augmentation system, which controls the roll, flight path and sideslip angles. Van Overeem [28] selected these variables to control as this is the same for the Airbus A350-900, which is the reference aircraft for the Flying-V [11]. It should be noted that for this controller it is assumed that $\gamma \approx \theta$, which is only true for small angles of attack.

The relation between the angular rates and the attitude angles, can be found in Equation 4.5 [1].

$$\begin{bmatrix} \dot{\phi} \\ \dot{\theta} \end{bmatrix} = \begin{bmatrix} 1 & \sin\phi\tan\theta & \cos\phi\tan\theta \\ 0 & \cos\phi & -\sin\phi \end{bmatrix} \begin{bmatrix} p \\ q \\ r \end{bmatrix} \tag{4.5}$$

To be able to perform coordinated turns, a sideslip dynamic inversion loop is used. β can be calculated with Equation 4.6.

$$\beta = \arcsin\frac{v}{V} \tag{4.6}$$

To get the NDI control law, Equation 4.6 needs to be differentiated, which leads to Equation 4.7.

$$\dot{\beta} = \frac{\dot{v}V - v\dot{V}}{V\sqrt{u^2 + w^2}} \tag{4.7}$$

This equation can be rewritten to Equation 4.8, in which A_x, A_y and A_z are defined by Equation 4.9, these accelerations are possible to be measured during flight [28].

$$\dot{\beta} = \left(\frac{1}{\sqrt{u^2 + w^2}}\right)(A_x + A_y + A_z) + \begin{bmatrix} \frac{w}{\sqrt{u^2+w^2}} & 0 & \frac{-u}{\sqrt{u^2+w^2}} \end{bmatrix} \begin{bmatrix} p \\ q \\ r \end{bmatrix} \tag{4.8}$$

$$\begin{aligned} A_x &= \frac{uv}{V^2}\left(\frac{F_x}{m} - g\sin\theta\right) \\ A_y &= \left(1 - \frac{v^2}{V^2}\right)\left(\frac{F_y}{m} + g\sin\phi\cos\theta\right) \\ A_z &= -\frac{vw}{V^2}\left(\frac{F_z}{m} + g\cos\phi\cos\theta\right) \end{aligned} \tag{4.9}$$

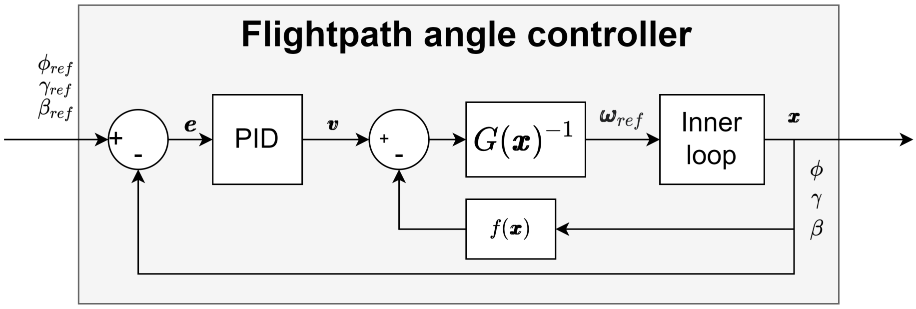

Figure 4.2: Flying-V flight path controller adapted from [28]

Combining Equation 4.2 and Equation 4.8 will give the NDI control law, as given in Equation 4.10 [28].

$$\omega_{ref} = \begin{bmatrix} 1 & \sin\phi\tan\theta & \cos\phi\tan\theta \\ 0 & \cos\phi & -\sin\phi \\ \frac{w}{\sqrt{u^2+w^2}} & 0 & \frac{-u}{\sqrt{u^2+w^2}} \end{bmatrix}^{-1} \left(\begin{bmatrix} v_{\phi_{ref}} \\ v_{\theta_{ref}} \\ v_{\beta_{ref}} \end{bmatrix} - \begin{bmatrix} 0 \\ 0 \\ \left(\frac{1}{\sqrt{u^2+w^2}}\right)(A_x + A_y + A_z) \end{bmatrix} \right) \tag{4.10}$$

The block diagram of the outer control loop can be found in Figure 4.2. In which $G(\boldsymbol{x})$ is equal to the first matrix in Equation 4.10 and $f(\boldsymbol{x})$ is equal to the right matrix of the equation.

4.4. Conclusion

In this chapter some ways of measuring the performance of an FCS were described, which partly answers research question 3a, as the handling qualities can be used to measure the performance of an INDI controller. The INDI controller as proposed by van Overeem was also described in this chapter.

5

Preliminary Analysis

In this chapter a preliminary analysis is done on an INDI controller applied on a Flying-V simulation. The goal of this preliminary analysis is to obtain some experience with the simulation of the Flying-V and the INDI controller as well as to find out where current challenges for the control system of the Flying-V are.

First in section 5.1 the simulation model of the Flying-V is described, after this in section 5.4 the design of the INDI controller and PID controller that will be compared is elaborated further on. In section 5.2 the two flying conditions which will be used for the simulation are described. After this in section 5.5 the results of the preliminary analysis are given and finally in section 5.7 the results are discussed in the conclusion.

5.1. Simulation Model

For the preliminary analysis a simulation of the Flying-V made by van Overeem [28] is used. In this section this simulation is described. As it is based on the aerodynamic model from section 2.3, the assumptions that applied there, also apply for this simulation.

5.1.1. Equations of motion

After the aerodynamic coefficients are determined with the previous state, using the aerodynamic model from section 2.3, the change in the states are calculated with the equations of motion, given in Equation 5.1.

$$
\begin{aligned}
\dot{x} &= (u\cos(\theta) + (v\sin(\phi) + w\cos(\phi))\sin(\theta))\cos(\psi) - (v\cos(\phi) - w\sin(\phi))\sin(\psi)\\
\dot{y} &= (u\cos(\theta) + (v\sin(\phi) + w\cos(\phi))\sin(\theta))\sin(\psi) + (v\cos(\phi) - w\sin(\phi))\cos(\psi)\\
\dot{z} &= -u\sin(\theta) + (v\sin(\phi) + w\cos(\phi))\cos(\theta)\\
\dot{u} &= vr - wq - g\sin(\theta) + \frac{F_x}{m}\\
\dot{v} &= wp - ur + g\sin(\phi)\cos(\theta) + \frac{F_y}{m}\\
\dot{w} &= uq - vp + g\cos(\phi)\cos(\theta) + \frac{F_z}{m}\\
\dot{p} &= \frac{I_{zz}}{I^*}M_x + \frac{I_{xz}}{I^*}M_z + \frac{\left(I_{xx} - I_{yy} + I_{zz}\right)I_{xz}}{I^*}pq + \frac{((I_{yy} - I_{zz})I_{zz} - I_{xx}^2)}{I^*}qr\\
\dot{q} &= \frac{M_y}{I_{yy}} + \frac{(r^2 - p^2)I_{xz}}{I_{yy}} + \frac{(I_{zz} - I_{xx})}{I_{yy}}pr\\
\dot{r} &= \frac{I_{xx}}{I^*}M_x + \frac{I_{xx}}{I^*}M_z + \frac{((I_{xx} - I_{yy})I_{xx} + I_{xz}^2)}{I^*}pq + \frac{(-I_{xx} + I_{yy} - I_{zz})I_{xz}}{I^*}qr\\
\dot{\phi} &= p + \sin(\phi)\tan(\theta)q + \cos(\phi)\tan(\theta)r\\
\dot{\theta} &= \cos(\phi)q - \sin(\phi)r\\
\dot{\psi} &= \frac{\sin(\phi)}{\cos(\theta)}q + \frac{\cos(\phi)}{\cos(\theta)}r
\end{aligned}
\tag{5.1}
$$

The forces and moments in Equation 5.1 F_x, F_y, F_z, M_x, M_y and M_z are defined as in Equation 5.3 and where I^* is calculated with Equation 5.2. The results of the Equation 5.1 are integrated to get the new state.

$$I^* = I_{xx}I_{yy} - I_{xx}^2 \tag{5.2}$$

$$
\begin{aligned}
F_x &= F_{x_{aero}} + T_1 + T_2\\
F_y &= F_{y_{aero}}\\
F_z &= F_{z_{aero}}\\
M_x &= M_{x_{aero}}\\
M_y &= M_{y_{aero}} - (T_1 + T_2)T_{dy} + F_{z_{aero}}(p_{ref} - p_{cg})\\
M_z &= M_{z_{aero}} + T_1T_{dz} - T_2T_{dz} - F_{y_{aero}}(p_{ref} - p_{cg})
\end{aligned}
\tag{5.3}
$$

5.1.2. Assumptions

For the simulation, the actuator and engine dynamics where approximated with a first order lag system, for which the transfer functions are given in Equation 5.4 [28]. The deflection limits of the control surfaces are 25 degrees in both directions [14] and the maximum thrust is equal to $3.79 * 10^5 N$ [3].

$$H_{act} = \frac{1}{\frac{1}{35.2}s + 1}, H_{thrust} = \frac{1}{0.2s + 1} \tag{5.4}$$

A block diagram of the simulation of the Flying-V dynamics are given in Figure 5.1, where the Aerodynamic model calculates the aerodynamic coefficients and the equations of motion calculates the change of the state, using Equation 5.1.

Furthermore it is assumed that the current state is instantly available for the controller, without any sensor lag or noise, and all states are available. Next to that are there no aerodynamic uncertainties. This means that the aerodynamic coefficients for the NDI controller and the control effectiveness for the INDI controller are known and accurate. There are also no external perturbations. Finally the simulation uses a time step of $0.005[s]$, which is also the sampling frequency for the controller.

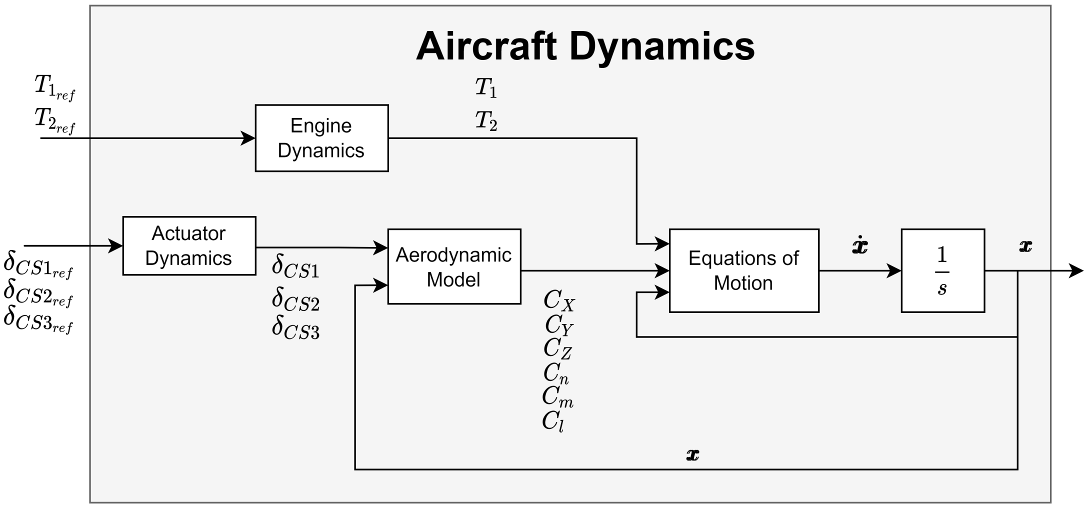

Figure 5.1: Flying-V model block diagram

5.2. Flight conditions

The preliminary analysis will look at two different flight conditions: cruise and approach. These conditions are chosen because van Overeem [28] and Cappuyns [8] identified these two conditions as the most critical conditions for having satisfactory handling qualities. Furthermore the aerodynamic data is available for both conditions. The parameters that are used for these conditions can be found in Table 5.1, in which a is the speed of sound. The mass from both conditions are obtained form Cappuyns [8]. For both conditions the most forward centre of gravity position is used (45% of MAC [8]).

	Cruise	Approach
$Mach[-]$	0.85	0.2
$a[m/s]$	295	343
$\rho[kg/m^3]$	1.225	0.2655
$Mass[kg]$	210000	240000

Table 5.1: Flight Condition parameters

5.3. Flying-V response to control surface deflections

To get a feeling for how the aircraft reacts to control surface deflections, the Flying-V was first simulated without any feedback control loops.

First a step input was given at two seconds to deflect control surface one with five degrees. The response can be found in Figure 5.2

In this figure the quick short period response as well as the slower phugoid can be clearly seen. It can also be observed that the phugoid response is stable, as the variation of θ slowly gets smaller. It should also be noted that control surface one does not influence the lateral rates.

After this a step input of $1°$ was applied to control surface two. The response of the Flying-V is plotted in Figure 5.3. The response to the same step input applied on control surface three can be seen in Figure 5.4

In these two figures the unstable dutch roll can be observed. The roll and yaw rate are clearly coupled, and amplify each others. It can also be observed that the pitch rate is also influenced, as well as that the aircraft is now in an unstable condition. Furthermore the sign of the response of the Flying-V is the opposite for surface one and two.

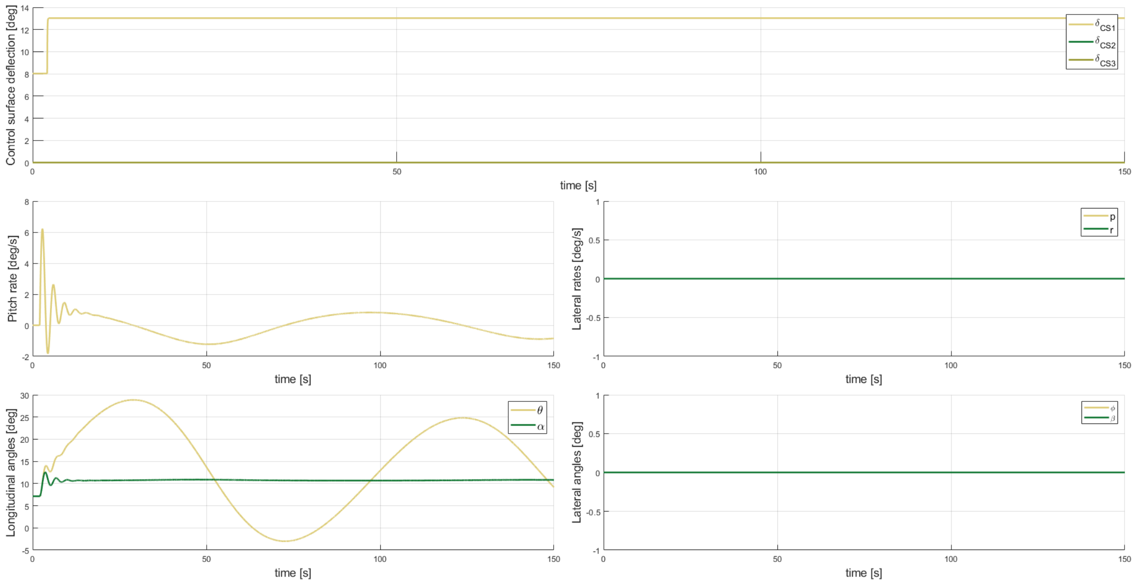

Figure 5.2: Flying-V response to deflection of control surface one

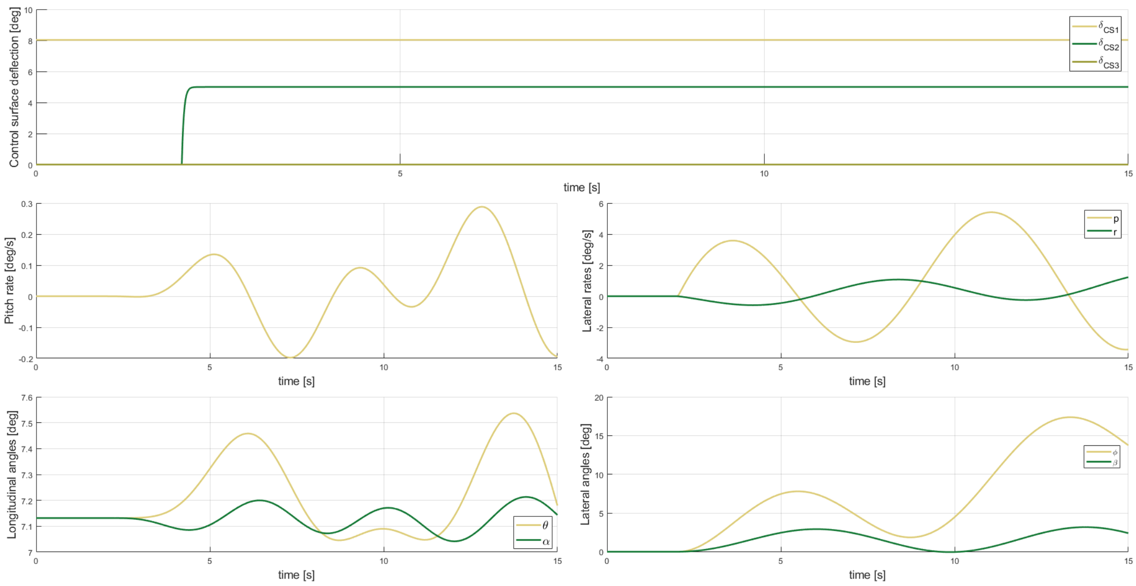

Figure 5.3: Flying-V response to deflection of control surface two

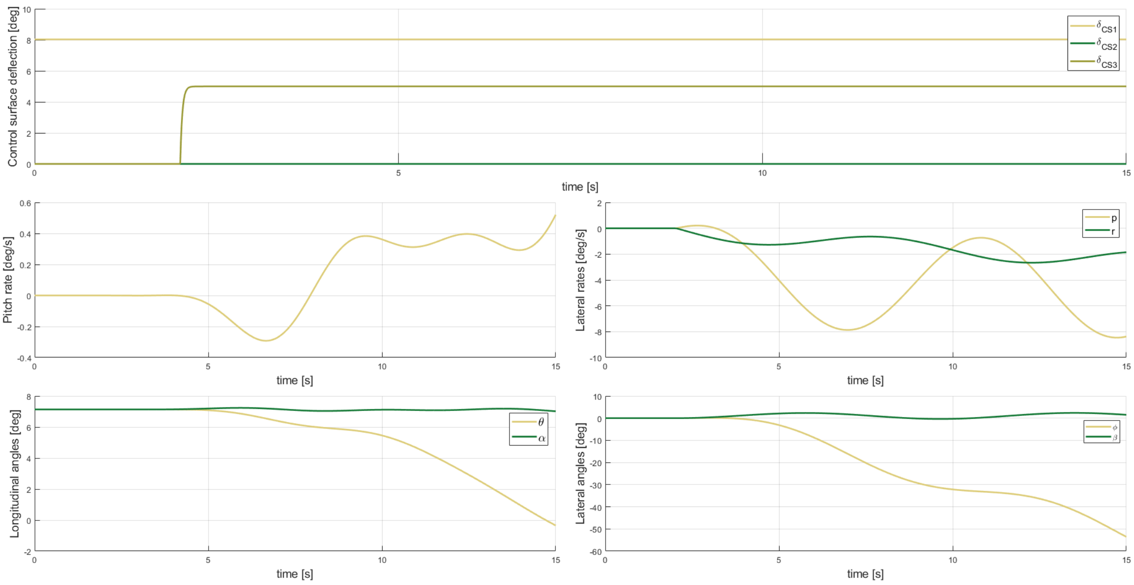

Figure 5.4: Flying-V response to deflection of control surface three

5.4. Controller design

To improve the flying and handling qualities of the Flying-V, a control augmentation system is required. In the preliminary analysis a PID controller is compared to an INDI controller, in this section the design of both controllers are given.

5.4.1. Inner loop controller

For the INDI controller, the inner loop controller will that will be used is described in Chapter 4.2. A block diagram of the PID controller which will be compared with the INDI controller can be found in Figure 5.5. The PID controller for the INDI control loop will have the same structure as the PID controller. To limit the bandwith of the differentiators, they are paired with a first order filter, which leads to Equation 5.5, where N is set to 10.

$$H(s) = \frac{Ns}{1 + Ns} \tag{5.5}$$

5.4.2. Outer loop controller

For the outer loop controller the NDI controller will be used, as described in Chapter 4.3 for both FCS. The block diagram of the PID can be found in Figure 5.6.

5.4.3. Gains

To tune the gains of the different controllers a Monte Carlo simulation was set up. The simulation was run separately for the gains of roll, pitch and yaw rate, as well for the roll, flight path and sideslip angles.

The simulation generates for the first iteration a list of 200 numbers following a normal distribution with parameters that can be found in Table 5.2. For all these numbers a simulation is run, tracking the rate which the gains control.

	INDI		**PID**	
	Mean	σ	Mean	σ
K_p	10	10	500	500
K_i	10	10	1000	1000
K_d	10	10	500	500

Table 5.2: Initial parameters gain tuning simulation inner loop

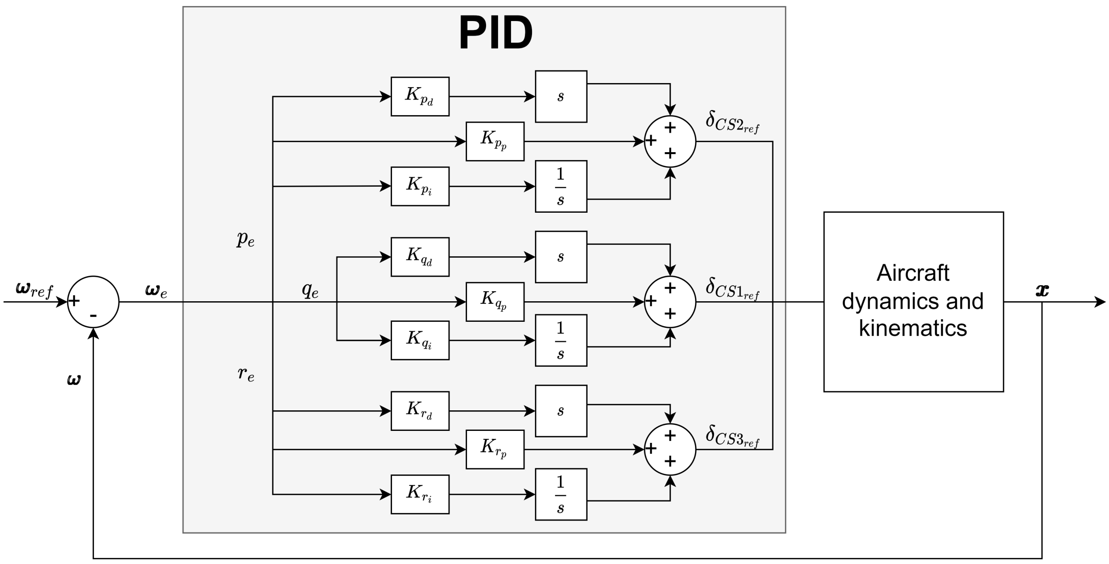

Figure 5.5: PID innerloop controller

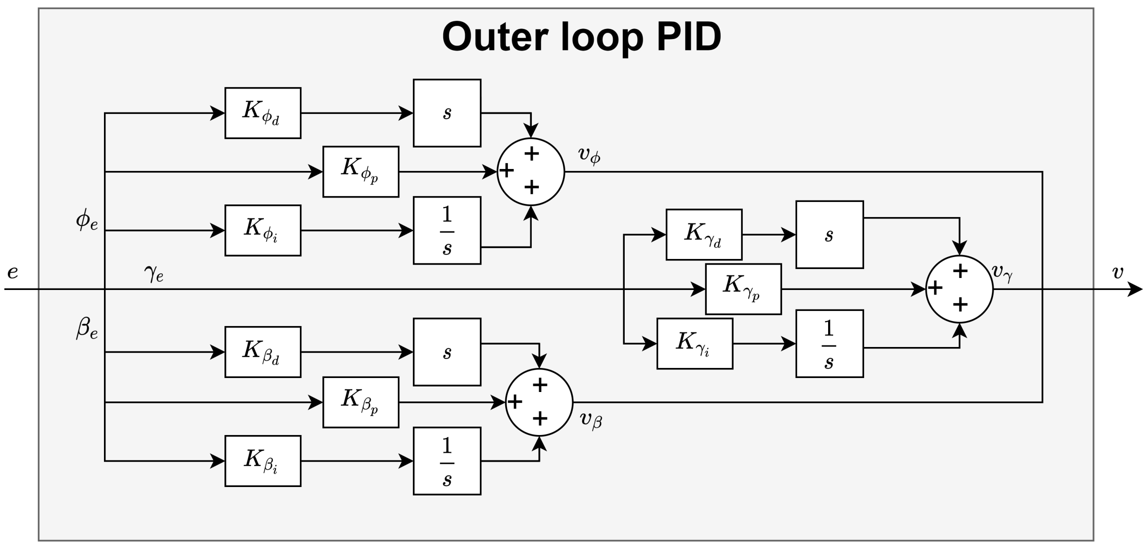

Figure 5.6: Linear controller of the control augmentation system

For each run a score is calculated using Equation 5.6 for the inner loop gains, and Equation 5.7 was used for the outer loop gains. The weights are selected to ensure that the different parts have the same order of magnitude.

$$Score = 100 \cdot e_{RMS} + 5 \cdot (T_{ss_1} + T_{ss_2}) + 2 \cdot (n_{osc_1} + n_{osc_2}) + 20 * (|e_{SS_1}| + |e_{SS_2}|) \tag{5.6}$$

$$Score = 100 \cdot e_{RMS} + 5 \cdot (T_{ss_1} + T_{ss_2}) + 2 \cdot (n_{osc_1} + n_{osc_2}) + 20 * (|e_{SS_1}| + |e_{SS_2}|) + 3 \cdot (OS_1 + OS_2) \tag{5.7}$$

In these equations e_{RMS} is the Root Mean Squared error, T_{SS} the settling time in seconds, n_{osc} the number of oscillations after the step input is applied, e_{SS} the steady state error and OS the overshoot. The 1 subscript is for the first step input and the 2 for the second step input.

The gains of the best scoring 10% given their scores are less then double of the best score, are used to determine the new mean and standard deviation for the gain list of the next iteration. If the score of the second best run is more then double of the best score of that run, the mean for the next iteration is equal to the gain of the best score, and the standard deviation is equal to 90% of the last standard deviation.

All iterations after the first one contain 50 runs. The simulation keeps running, until the best score does not improve for two iterations in a row. When the best score does not improve for one iteration, the standard deviation is set to 110% of the previous standard deviation.

For the generation of the gain list the MATLAB function $normrnd()$ is used, with seed = 1.

The reference signal for the inner loop tuning can be found in Table 5.3.

$t < 5s$	$S_{ref} = 0°/\text{s}$
$5s \leq t < 15s$	$S_{ref} = -2°/s$
$15s \leq t \leq 30$	$S_{ref} = 2°/s$

Table 5.3: Inner loop tuning reference signal

As the gains for the yaw and roll rate have influence on each other, the roll rate was tuned first, after which the yaw rate was tuned, to then retune the roll rate with the newly founded yaw rate gains. As the difference in roll rate gains was small, the yaw rate was not tuned again. The initial yaw rate gains can be found in Table 5.4. It should also be noted that the initial mean for the gains for the yaw rate of the PID controller where set to be negative.

	INDI	**PID**
K_{r_p}	2.5	-430
K_{r_i}	1.2	-500
K_{r_d}	0	-400

Table 5.4: Initial yaw rate gains for gain tuning

For the outer loop gains, the reference signal is given in Table 5.5. For the sideslip angle gains a different reference was used, given in Table 5.6. The signal for the sideslip angle is different, as the tuning method had troubles finding stable gains for the reference signal given in Table 5.5.

$t < 20s$	$S_{ref} = 0°$
$20s \leq t < 60s$	$S_{ref} = -5°$
$60s \leq t \leq 100s$	$S_{ref} = 5°$

Table 5.5: Outer loop tuning reference signal

The order of tuning the gains was for the outer loop the same as for the inner loop, the initial gains for the sideslip angle can be found in Table 5.8

The initial parameters for the tuning can be found in Table 5.7. In Figure 5.7 the best and average score of each iteration for the tuning of the pitch rate gains for the INDI controller are given. In the figure

$$
\begin{array}{ll}
t < 10s & \beta_{ref} = 0^\circ \\
10s \leq t < 40s & \beta_{ref} = -1^\circ \\
40s \leq t \leq 70s & \beta_{ref} = 1^\circ
\end{array}
$$

Table 5.6: Sideslip tuning reference signal

	Mean	σ
K_p	4	3
K_i	4	3
K_d	4	3

Table 5.7: Initial parameters gain tuning simulation outer loop

	Gain [-]
K_{β_p}	1.5
K_{β_i}	0
K_{β_d}	3

Table 5.8: Initial sideslip compensator gains

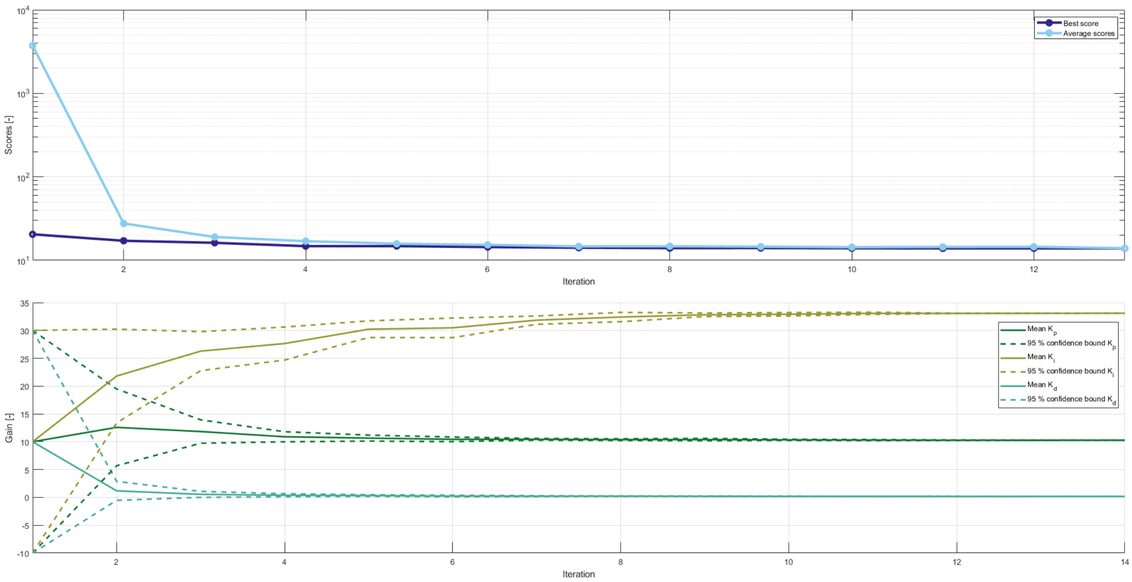

Figure 5.7: Scores and gain statistics for tuning the INDI pitch tracking in approach conditions

the mean of each gain, and the bounds for which 95% of the samples are located are given, where it clearly that the confidence bounds for all the three gains converges.

The resulting scores for all the gains that were tuned can be found in Table 5.9. It should be noted that the scores for the INDI controller are for all the different conditions are higher then for the PID controller. The resulting gains that where found from the tuning, can be found in Table 5.10. The gains for the yaw rate for the PID controller are negative, as the response gives negative yaw rates for positive deflections. The INDI controller already reverses the sign with the control effectiveness matrix.

	INDI		**PID**	
	Cruise	Approach	Cruise	Approach
p	17.10	120.25	20.42	136.79
q	16.29	13.90	37.18	24.72
r	55.92	10008	128.92	10005.5
ϕ	90.99	[−]	238.6	[−]
γ	89.75	[−]	206.44	[−]
β	47.35	[−]	196.90	[−]

Table 5.9: Tuning scores

	PID		**INDI**	
	Cruise	Approach	Cruise	Approach
K_{p_p}	506.9	115.9	10.10	8.941
K_{p_i}	23010	3039.6	28.50	22.239
K_{p_d}	126.3	244.6	0.412	0.059
K_{q_p}	210.1	1131.5	17.33	20.95
K_{q_i}	4364.3	4085	37.80	33.09
K_{q_d}	38.80	14.04	0.398	0.181
K_{r_p}	−724.4	−1459.6	8.837	14.53
K_{r_i}	−2938	−332.3	11.795	2.967
K_{r_d}	−813.5	−2.679	2.299	15.87

Table 5.10: Gains of the PID controller and PID part of the INDI controller

The gains for the outer loop linear controller are in Table 5.11. The tuning for the gains was done

	INDI	**PID**
K_{ϕ_p}	1.38	0.60
K_{ϕ_i}	0.75	0.15
K_{ϕ_d}	0.36	$2.6 \cdot 10^{-3}$
K_{γ_p}	2.27	1.97
K_{γ_i}	$6.97 \cdot 10^{-3}$	0.15
K_{γ_d}	2.81	1.21
K_{β_p}	2.54	0.54
K_{β_i}	0	0.11
K_{β_d}	1.82	0.26

Table 5.11: Outer loop PID gains

in nominal conditions, where the tracking performance was optimised. The disadvantage of this is that extra effects, as for example sensor delay or nuisance dynamics were not taken into account, which can degrade the performance, and might make the gains founded here unstable, where other gains would perform better.

When running the simulation for the PID flight path angle tracking, it was found that the controller had problems with control surface deflection saturation and oscillations. To try to improve its performance, the pitch rate gains were tuned again, with a different cost function, that penalises control surface deflections. The cost function can be found in Equation 5.8, in which var_{CS_x} is calculated with Equation 5.9.

$$Score = 100 \cdot e_{RMS} + 5 \cdot (T_{ss_1} + T_{ss_2}) + 2 \cdot (n_{osc_1} + n_{osc_2}) + 20 * (|e_{SS_1}| + |e_{SS_2}|) + 50 \cdot (var_{CS_1} + var_{CS_2} + var_{CS_3}) \tag{5.8}$$

$$var_{CS_x} = \frac{1}{N-1} \sum_{i=1}^{N} \left(\delta_{CS_x} - \mu_{\delta_{CS_x}} \right) \tag{5.9}$$

After retuning the inner loop, the outer loop flight path angle controller was also retuned, the gains that where found can be seen in Table 5.12.

	q	γ
K_p	207.98	1.72
K_i	3951	$1.73 \cdot 10^{-3}$
K_d	18.3	0.41

Table 5.12: PID gains for the retuned pitch rate and flying path tracking

5.5. Results

To be able to compare the tracking performance of the two controllers, the following metrics are used:

- Rise time: time between the step input and the tracking signal reaching 90% of that value
- Overshoot: Ratio between the step value and the maximum (or minimum if the step is negative) value of the tracking signal
- Settling time: Time until the tracking signal stays within 1% of the reference signal
- Steady state error: The difference between the the reference signal and the tracking signal after the tracking signal reached its steady state. Calculated as a percentage with Equation 5.10
- Root Mean Square (RMS) error, calculated with Equation 5.11.

$$e_{ss} = \frac{S_{SS} - S_{ref}}{S_{ref}} \cdot 100 \tag{5.10}$$

$$e_{RMS} = \sqrt{\frac{1}{n} \sum \left(S_{track} - S_{ref} \right)^2} \tag{5.11}$$

Next to these parameters, the control surface deflections will also be evaluated.

For the comparison of the inner loop controllers the pitch rate and roll rate tracking will be compared in cruise and approach conditions. The PID gains are tuned according to the method described in the previous section. The flight path angle and roll angle tracking performance will also be compared, where the outer loop is the same for both controllers. This comparison will only be done in cruise condition. After this both inner loop controllers are tested to see if they meet the Gibson criteria for dropback and flight path angle delay. These criteria are chosen, as they can be evaluated using only the the pitch and flight path angle response, and do not require extra analysis, like a low order equivalent system.

5.5.1. Pitch rate tracking

To compare the pitch rate tracking performances of the PID and INDI controllers, a reference signal given in Table 5.13 is applied as input to the inner loop controller.

$t < 10s$	$q_{ref} = 0°/s$
$10s \leq t < 20s$	$q_{ref} = -1°/s$
$20s \leq t$	$q_{ref} = 1°/s$

Table 5.13: Pitch rate reference signal

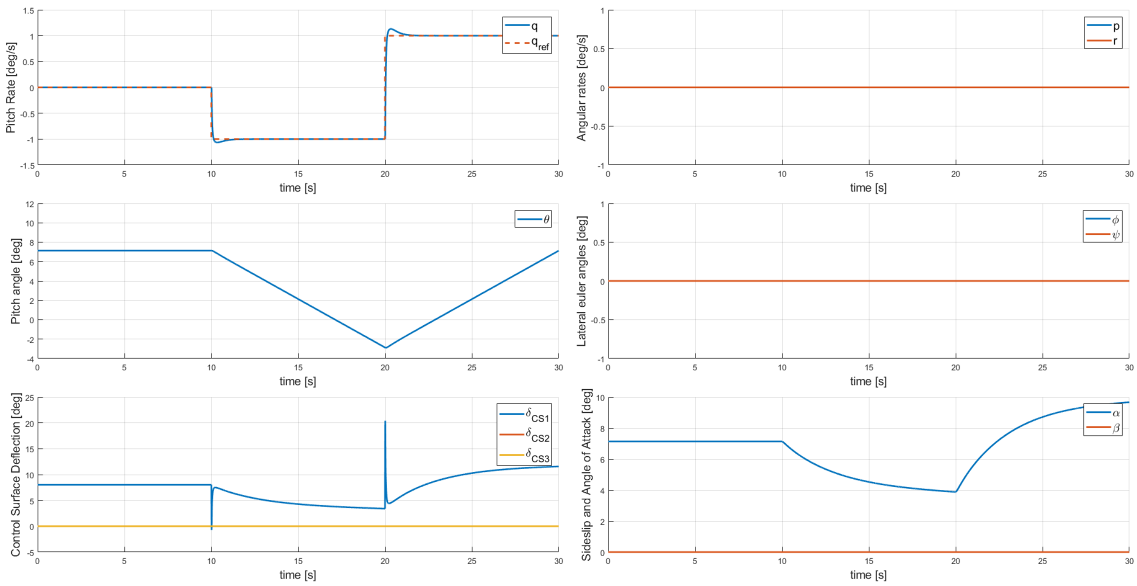

Figure 5.8: Pitch rate tracking performance INDI controller with cruise conditions

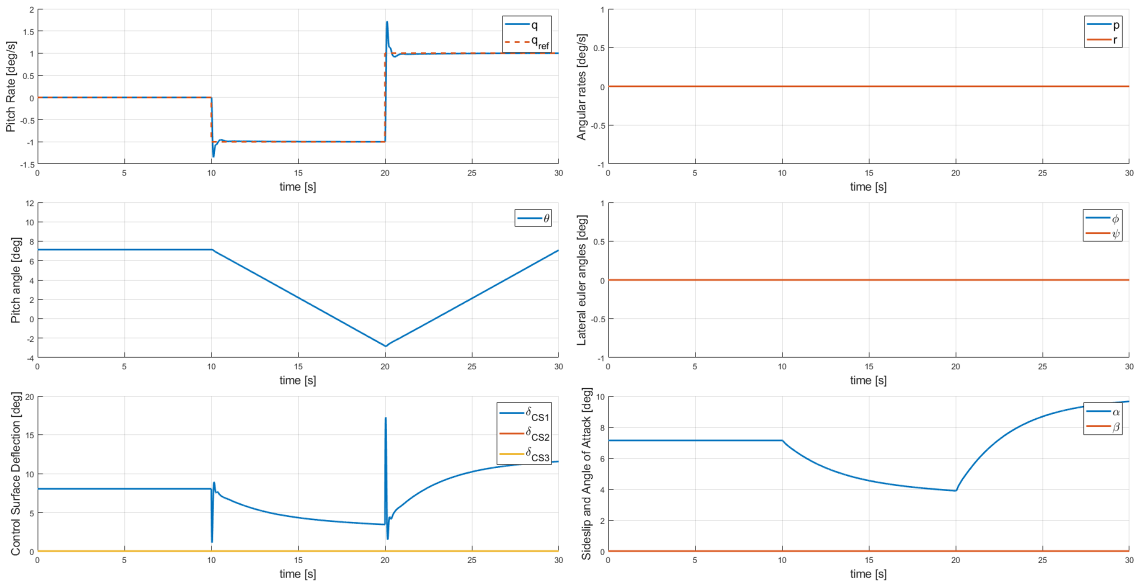

Figure 5.9: Pitch rate tracking performance PID controller with cruise conditions

Cruise conditions

In Figure 5.8 the time traces of the INDI controller are given for cruise condition.

Where in Figure 5.9 the time traces of the PID controller are given. The calculated statistics of the tracking by the INDI and PID controller are in Table 5.14.

When comparing both time traces it can be noted that the PID controller has more overshoot, and takes more time to reach the steady state. Which can also be seen in Table 5.14. The rise times of the PID controller are smaller than for the INDI controller, however after the initial rise the PID controller suffers from some oscillations in the pitch rate.

Another difference between the two, are the control surface deflections. The PID controller has smaller maximum deflections, but the deflections have a longer period of rapid changes. The difference between the maximum deflections is only minor.

	INDI	PID	$PID_{retuned}$
Rise Time 1 [s]	0.09	0.067	0.082
Rise Time 2 [s]	0.11	0.07	0.084
Overshoot 1 [-]	1.066	1.256	1.385
Overshoot 2 [-]	1.132	1.518	1.772
Settling time 1 [s]	1.22	1.93	2.30
Settling time 2 [s]	1.47	3.85	4.16
e_{SS_1} [%]	0.001	−0.15	−0.16
e_{SS_2} [%]	0.002	−0.16	−0.18
RMS error [deg/s]	$1.31 \cdot 10^{-3}$	$1.40 \cdot 10^{-3}$	$1.67 \cdot 10^{-3}$

Table 5.14: Pitch rate tracking statistics cruise condition

In Figure 5.10 the results of the retuned PID controller can be seen. When comparing with the other PID controller, the controller has a slightly longer rise time and slightly more overshoot, as well as longer settling times and steady state errors. However, the maximum control surface deflection is less, which are results that were expected.

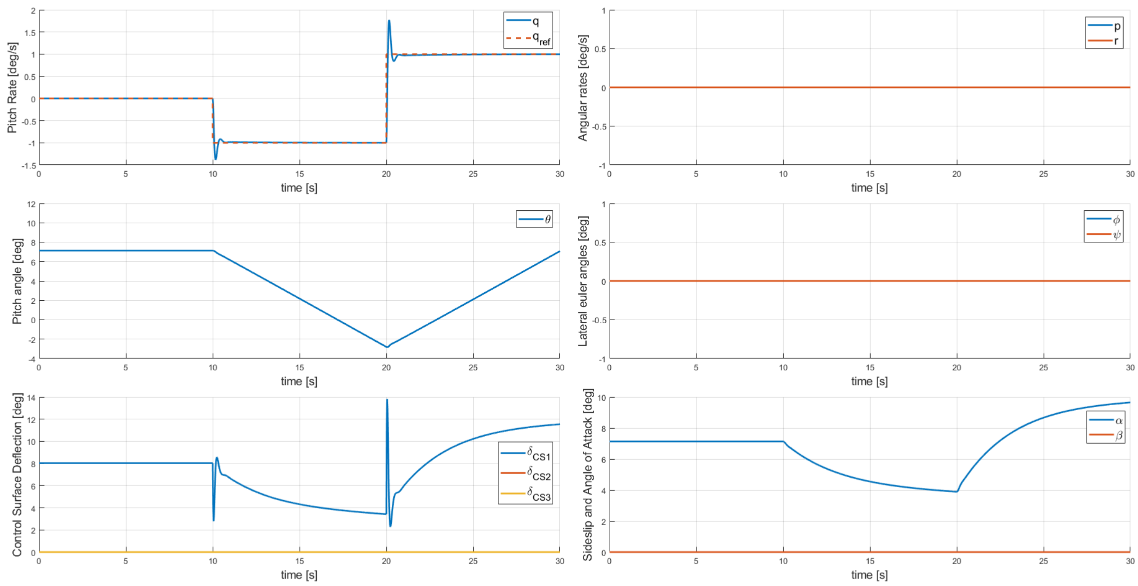

Figure 5.10: Pitch rate tracking performance retuned PID controller in cruise conditions

Approach Condition

The same reference signal is applied in approach condition, this leads to Figure 5.11 as the time trace of the INDI controller in approach condition and Figure 5.12 for the PID controller.

In Table 5.15 the measured metrics are given, and also the difference with the same controller in cruise conditions.

The performance of the INDI controller for approach for the first step input is only slightly different from the performance in cruise condition, however, the second step input has a slower response. This is can be explained by the fact that the $\delta_{CS1_{trim}}$ for approach is closer to the actuator limit, giving it only a small extra positive deflection. The rise times of the PID controller are both slower compared to the cruise conditions, however the settling times are really small, but the steady state error is larger compared to the cruise conditions.

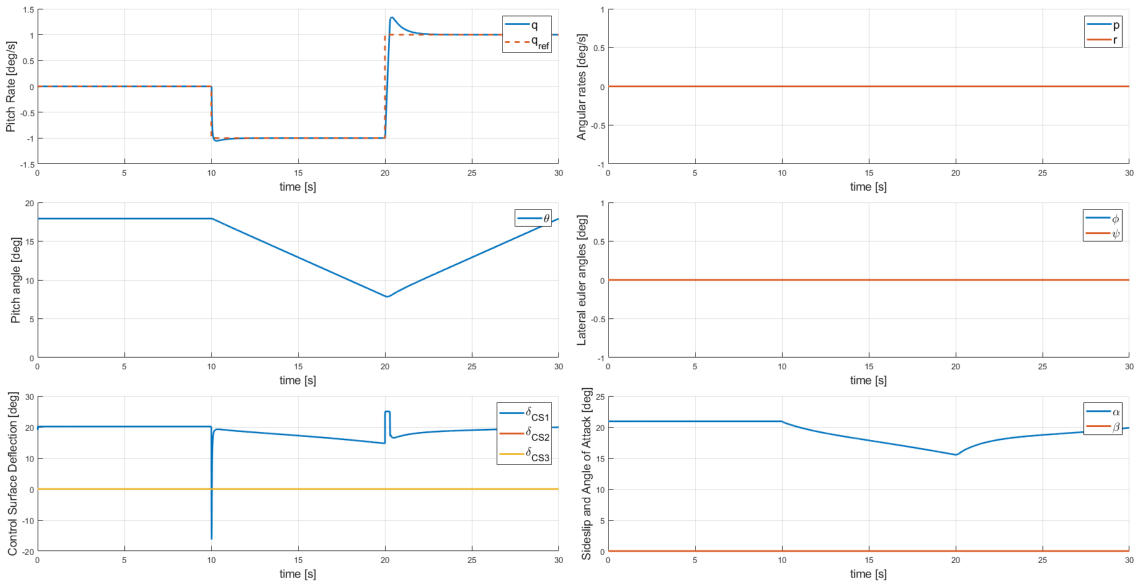

Figure 5.11: Pitch rate tracking performance INDI controller with approach conditions

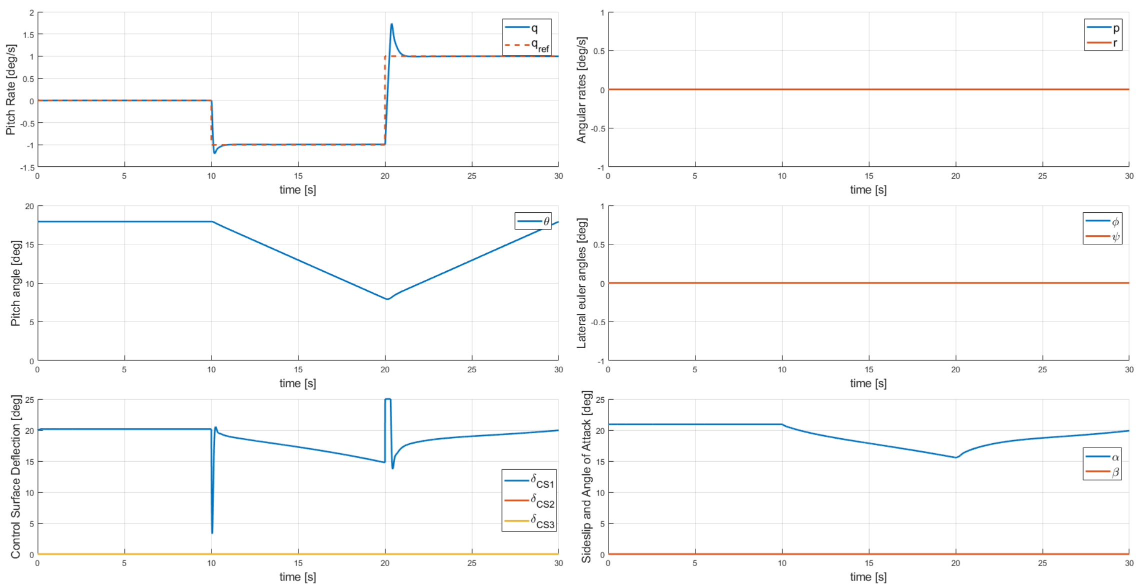

Figure 5.12: Pitch rate tracking performance PID controller with approach conditions

When comparing the INDI and PID controller in approach conditions, the PID controller has faster settling times, but the first rise time is slower, exactly the opposite of in cruise conditions. However, the steady state error of the PID controller is larger, as well as the RMS error. The control surface deflections are quite similar, with the exception of the peak at $t = 10s$, where the deflection for the INDI controller is considerably larger.

5.5.2. Roll rate tracking

For the roll rate tracking, the same reference signal as in Table 5.13 is given, only it is a reference signal for the roll rate instead of the pitch rate.

Cruise Condition

The time traces of the INDI and PID controllers in cruise condition are given in respectively Figure 5.13 and Figure 5.14.

	INDI	Difference with Cruise	PID	Difference with Cruise
Rise Time 1 [s]	0.08	−11.1%	0.11	+64.2%
Rise Time 2 [s]	0.25	+127.3%	0.25	+257.1%
Overshoot 1 [-]	1.053	−1.22%	1.201	−4.4%
Overshoot 2 [-]	1.338	+18.2%	1.738	14.5%
Settling time 1 [s]	1.325	+8.6%	0.74	−61.7%
Settling time 2 [s]	2.49	+69.4%	1.145	−70.3%
e_{ss_1} [%]	−0.001	0%	−0.82	+446.7%
e_{ss_2} [%]	$-4.5 \cdot 10^{-4}$	−77.5%	−0.32	+100%
RMS error [deg/s]	$2.1 \cdot 10^{-3}$	+60.3%	$2.3 \cdot 10^{-3}$	+64.3%

Table 5.15: Pitch rate tracking statistics approach condition

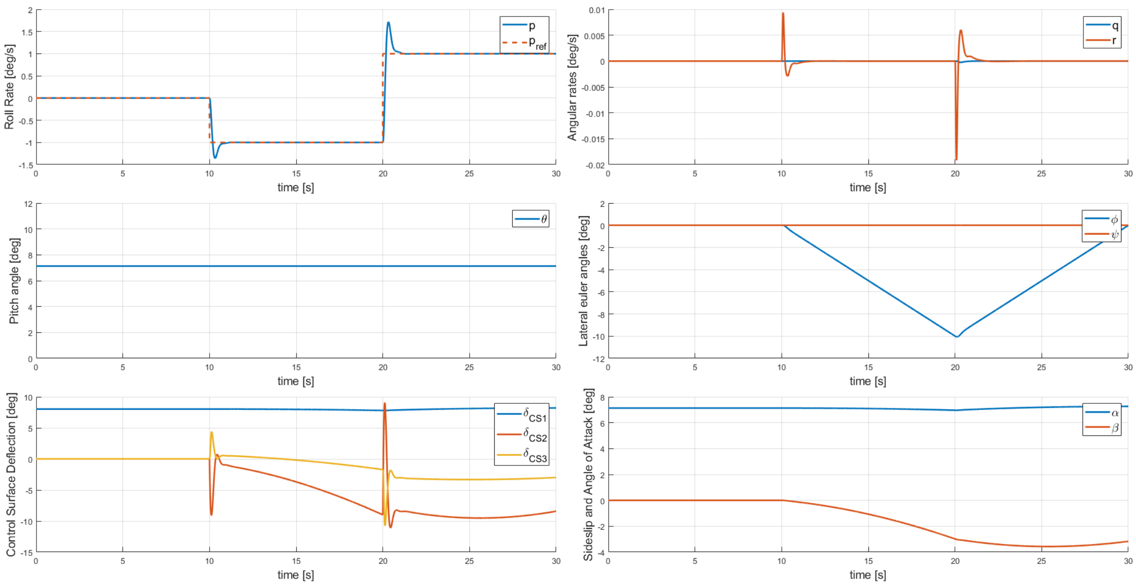

Figure 5.13: Roll rate tracking performance INDI controller with cruise conditions

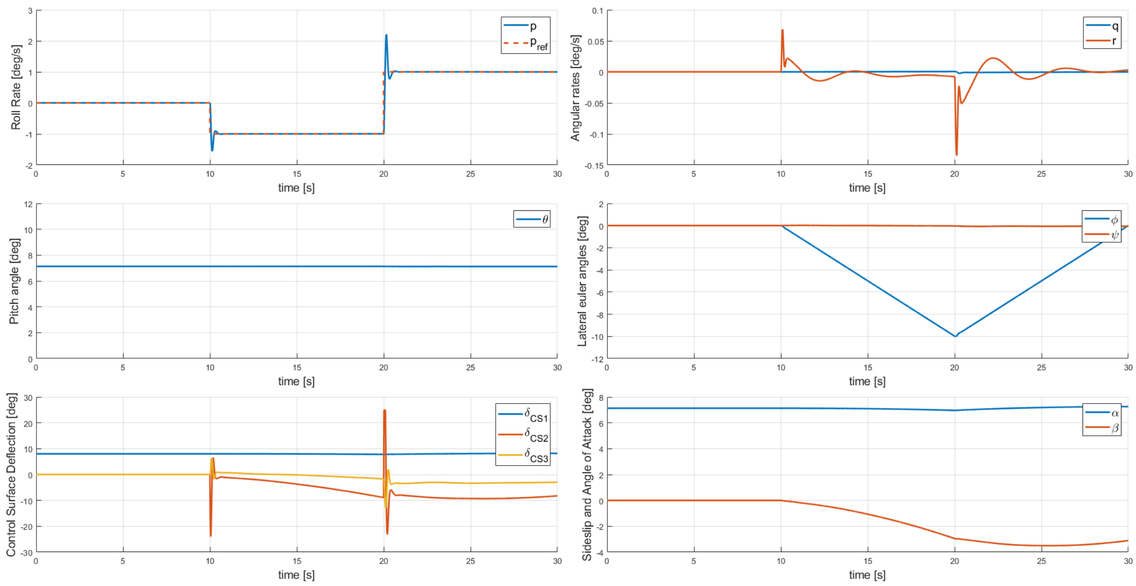

Figure 5.14: Roll rate tracking performance PID controller with cruise conditions

The different statistics are given in Table 5.16. The PID controller has a faster rise and settling time. The overshoot of the INDI controller is smaller. However, the steady state tracking error is smaller. The PID controller again has more oscillations than the INDI controller. Another big difference is with the yaw rate. Where the INDI controller is able to keep the yaw rate really small, with only minor spikes when the step input is applied, the PID controller has more difficulty keeping the yaw rate equal to zero. The better performance of the INDI controller can be an indication that INDI is better able to deal with the coupling between the roll and yaw rate.

	INDI	PID
Rise Time 1 [s]	0.17	0.07
Rise Time 2 [s]	0.175	0.085
Overshoot 1 [-]	1.358	1.561
Overshoot 2 [-]	1.719	2.213
Settling time 1 [s]	1.025	0.49
Settling time 2 [s]	1.1	0.755
e_{SS_1} [%]	-0.02	-0.31
e_{SS_2} [%]	-0.03	-0.12
RMS error [deg/s]	$2.363 \cdot 10^{-3}$	$1.903 \cdot 10^{-3}$

Table 5.16: Roll rate tracking statistics cruise condition

When looking at the control surface deflections another difference can be seen between both controllers, and that is that the PID controller has much larger deflections than the INDI controller.

Approach Condition

When the same signal is applied in the approach condition, the INDI reaction is given in Figure 5.15 and the PID in Figure 5.16.

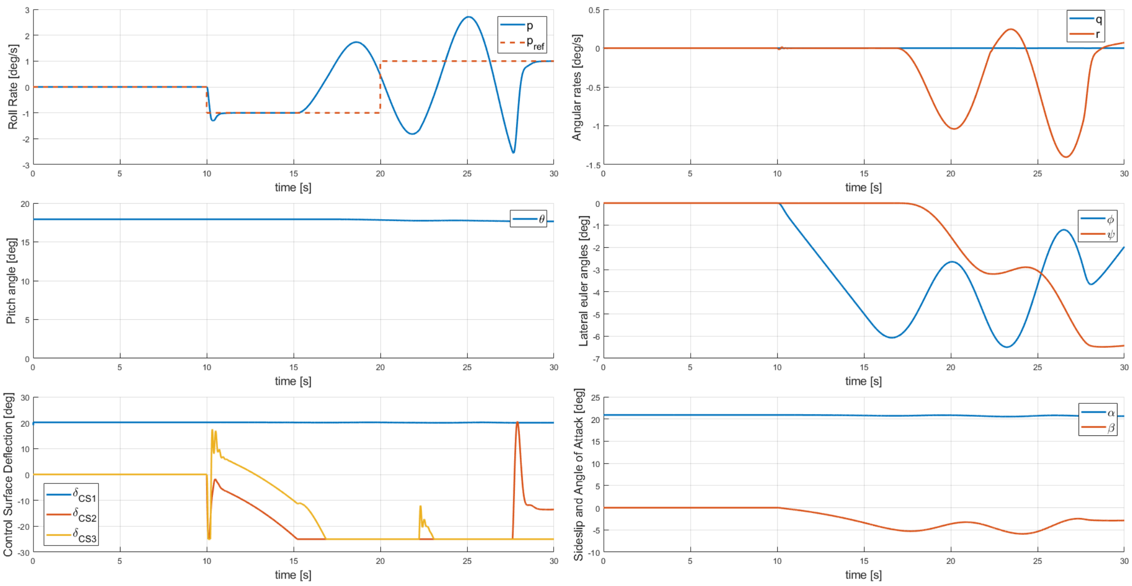

Figure 5.15: Roll rate tracking performance INDI controller with approach conditions

The measured statistics and the difference with the cruise condition are given in Table 5.17.

When looking at Figure 5.15 it can be seen that the roll rate tracking is good up to around 15 seconds, when it suddenly deviates. An explanation for this can be found in the control surface deflections, where control surface 2 reaches its actuator limit at 15 seconds. After this the natural roll damping starts to decrease the roll rate, which can no longer be compensated with more elevon deflection. The lack of lateral control authority for the Flying-V at low speeds was also found by Cappueyns [8].

To verify that control surface saturation is the problem here, a simulation was run, where the actuator

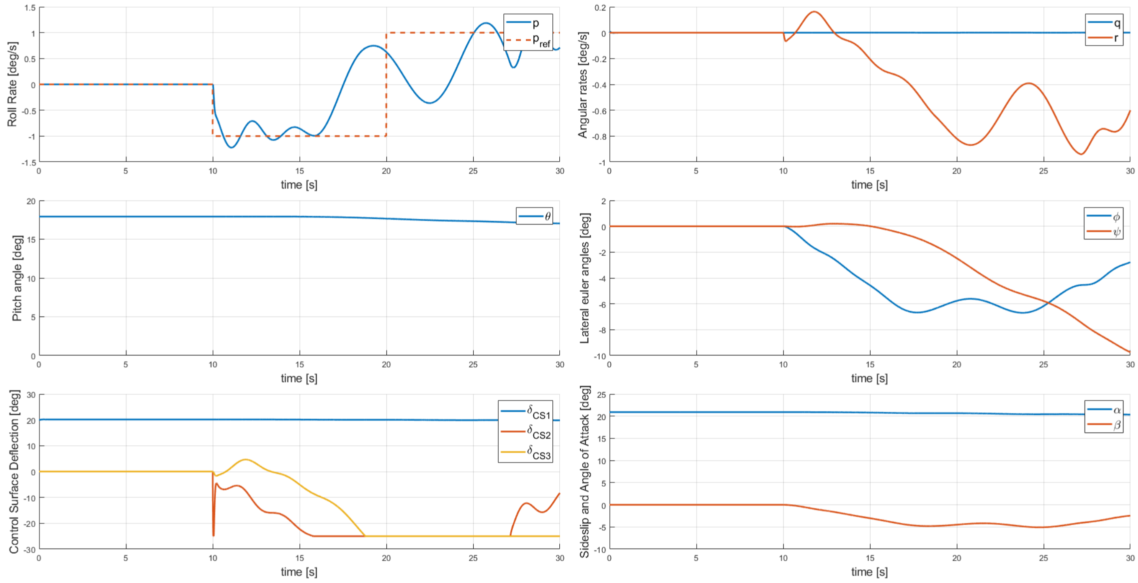

Figure 5.16: Roll rate tracking performance PID controller with approach conditions

limits were set to $[-70°, -70°]$, of which the results are plotted in Figure 5.17. In this situation the INDI controller is again able to follow the reference signal as expected.It should be noted that in the aerodynamic model that is used, the control surface layout of Cappueyns [8] is used, other control surface layouts may have fewer problems in this situation, the use of the inboard elevon also for lateral control will also help with the problem of lack of control authority.

The performance of the INDI controller might also be improved by applying pseudo-control hedging, as this could help prevent windup. However, the control authority should be improved first. When running the simulation with the normal actuator limits for a longer period, after 31 seconds the aircraft is able to again follow the reference signal, until 41 seconds, when the actuators reach the other deflection limit.

The PID controller also has problems, as it again struggles to follow the reference signal. For this approach condition it seems that there is not enough control authority to be able to follow this reference signal. However, the mean error is smaller for the PID controller.

	INDI	Difference with Cruise	PID	Difference with Cruise
Rise Time 1 [s]	0.19	$+11.8\%$	0.51	628.6%
Rise Time 2 [s]	$[-]$	$-$	$[-]$	$-$
Overshoot 1 [-]	1.31	-3.5%	1.22	-21.8%
Overshoot 2 [-]	$[-]$	$-$	$[-]$	$[-]$
Settling time 1 [s]	0.73	$+40,4\%$	$[-]$	$-$
Settling time 2 [s]	$[-]$	$-$	$[-]$	$-$
RMS error [deg/s]	$2.14 \cdot 10^{-2}$	$+805.6\%$	$1.09 \cdot 10^{-2}$	$+472.8\%$

Table 5.17: Roll rate tracking statistics approach condition

5.5.3. Flight path angle

For the flight path angle tracking the reference signal is given in Table 5.18.

The results can be found in Figure 5.18 and Figure 5.19, with the statistics in Table 5.19.

The INDI controller has faster rise and settling times, as well as less overshoot, and the RMS error is smaller. The PID controller does have a smaller second steady state error. However the PID controller suffers a lot from oscillations, and control surfaces that switch between maximum deflections to both limits of the actuators. Furthermore, the INDI controller performs better in terms of rise and settling

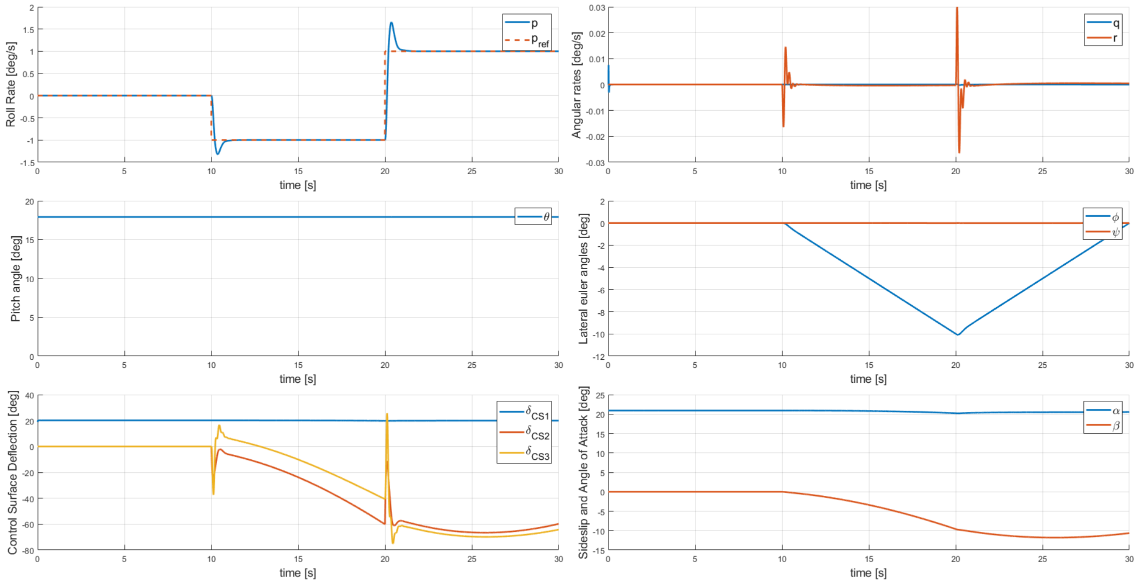

Figure 5.17: Roll rate tracking performance INDI controller with approach conditions and actuator limits set to $[-75°, 75°]$

$$
\begin{array}{ll}
t < 20 & \gamma_{ref} = 0° \\
20 \leq t < 60 & \gamma_{ref} = -2° \\
60 \leq t & \gamma_{ref} = 2°
\end{array}
$$

Table 5.18: Flight path angle reference signal

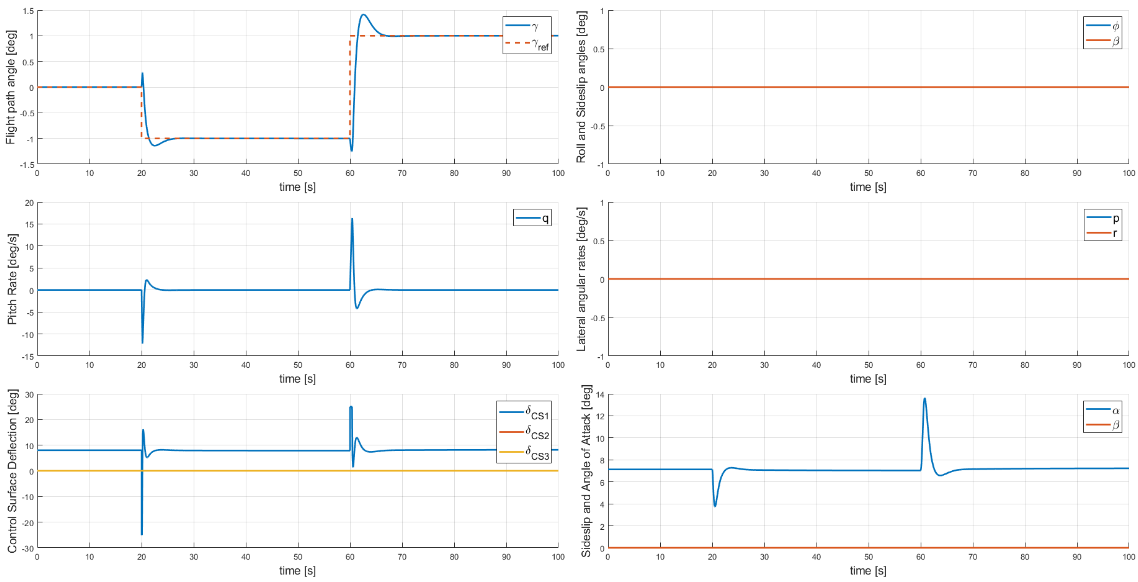

Figure 5.18: Flight path angle tracking performance INDI controller

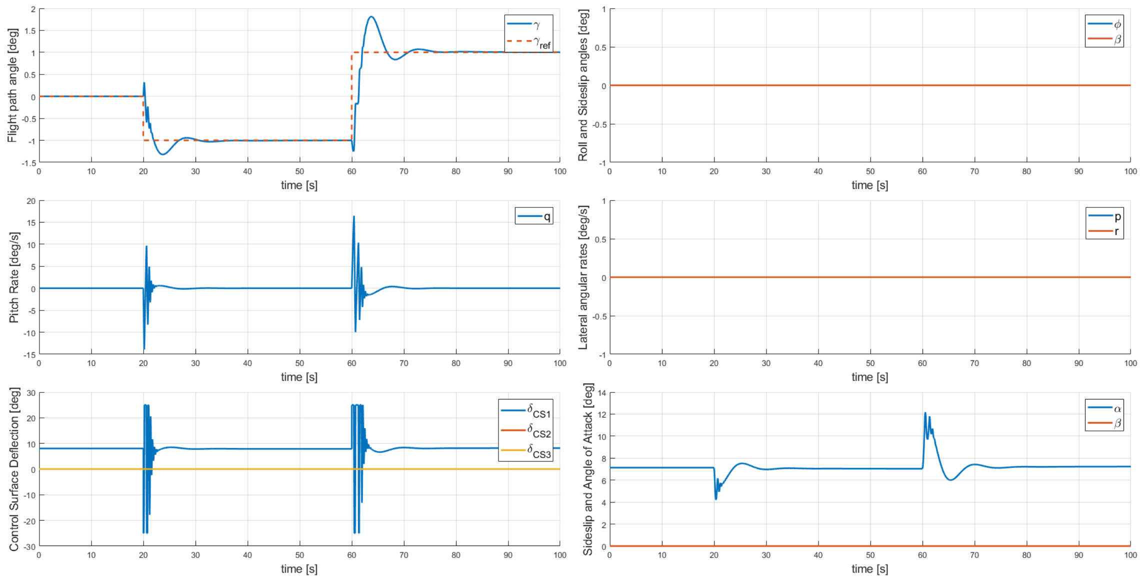

Figure 5.19: Flight path angle tracking performance PID controller

	INDI	$PID_{original}$	$PID_{command}$	$PID_{retuned}$
Rise Time 1 [s]	1.171	1.749	2.21	2.17
Rise Time 2 [s]	1.395	1.963	2.32	2.28
Overshoot 1 [-]	1.2524	1.335	1.316	1.40
Overshoot 2 [-]	1.4164	1.897	1.662	1.85
Settling time 1 [s]	5.945	15.76	16.2	19.3
Settling time 2 [s]	6.542	24.51	25.4	23.54
e_{SS_1} [%]	0.12	0.173	0.17	0.06
e_{SS_2} [%]	0.12	0.308	0.34	0.07
RMS error [deg]	$0.37 \cdot 10^{-2}$	$0.93 \cdot 10^{-2}$	$0.92 \cdot 10^{-2}$	$0.9 \cdot 10^{-3}$

Table 5.19: Flight path angle tracking statistics

times. It should also be noted that both controllers show non minimum-phase behaviour, as the flight path angle first goes down, before it goes up and vice-versa.

There are two ways of improving the performance of the flight path angle tracking of the PID investigated. The first one is changing the cost function for the pitch rate tracking, as described in subsection 5.4.3. The second one is to implement a first-order filter on the input of the outer control loop. The transfer function of the filter can be found in Equation 5.12.

$$H_{command} = \frac{1}{1 + 0.4s} \tag{5.12}$$

The time constant of this first-order filter was found by running the simulation with different time constants ranging from zero to 1.5, and using the time constant that gave the best score, using the same scoring method as for the gain tuning.

The statistics can be found in Table 5.19, and a comparison can be seen in Figure 5.20. When comparing the three PID results, it can be seen that the command filter and retuning both worked for reducing the number of oscillations and period the control surfaces are saturated. However, the response is slower than the original PID tuning, which was already slower than the INDI control. A possible disadvantage of the command filter is that the unwanted oscillations could still occur due to gust winds, as the feedback signal is not affected by the filter.

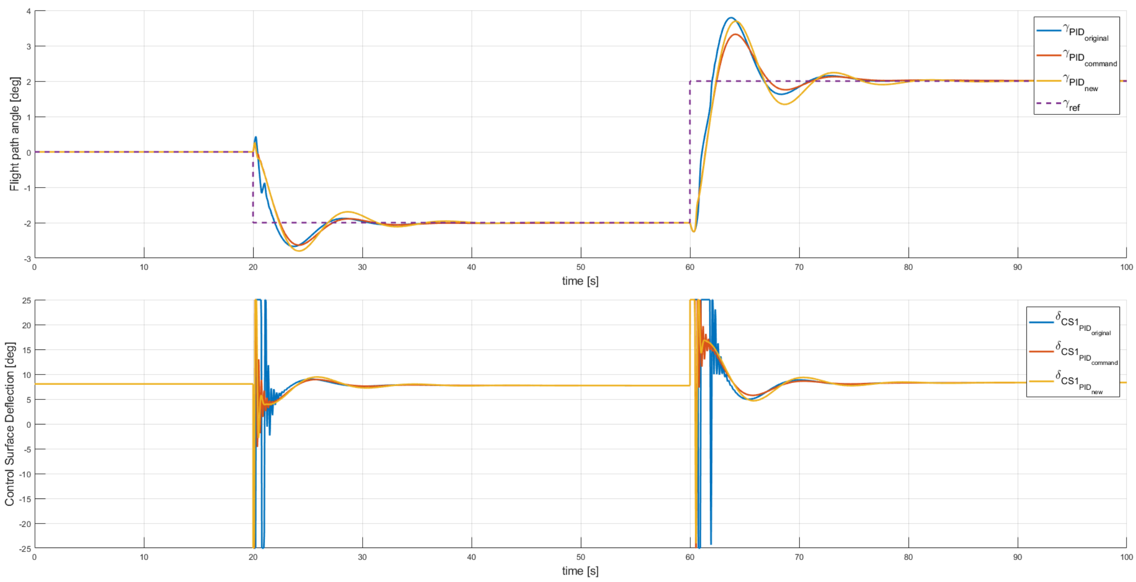

Figure 5.20: Comparison in flight path angle tracking between the PID, PID with command filter and with the retuned PID

5.5.4. Roll angle

For the roll angle tracking the same reference signal is used, as for the flight path angle, only applied to the roll angle. The results can be found for the INDI controller in Figure 5.21 and for the PID in Figure 5.22. The resulting metrics are listed in Table 5.20.

When comparing both results, it is clear that the INDI controller performs better then the PID controller, as all metrics have better values for the INDI controller except for the second overshoot, which is smaller at the PID controller. Another difference is the control surface deflections, which oscillate less at the INDI controller than for the PID controller. The roll angle for the PID controller contains also more oscillations.

For both controllers the steady state error is really small. However for both controllers there are a lot of oscillations between the maximum deflections of the control surfaces, which indicates little control authority, a problem that was also present in the roll rate tracking in approach conditions. The flight path angle for the PID controller has smaller peaks then for the INDI controller, but it takes longer to get back to a zero degree flight path angle.

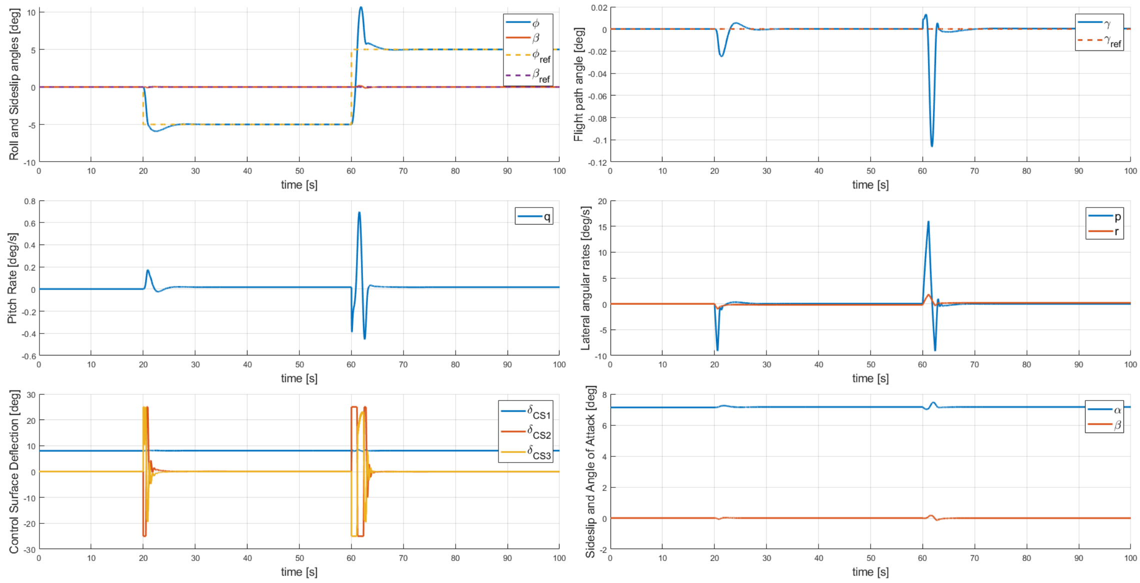

Figure 5.21: Roll angle tracking performance INDI controller

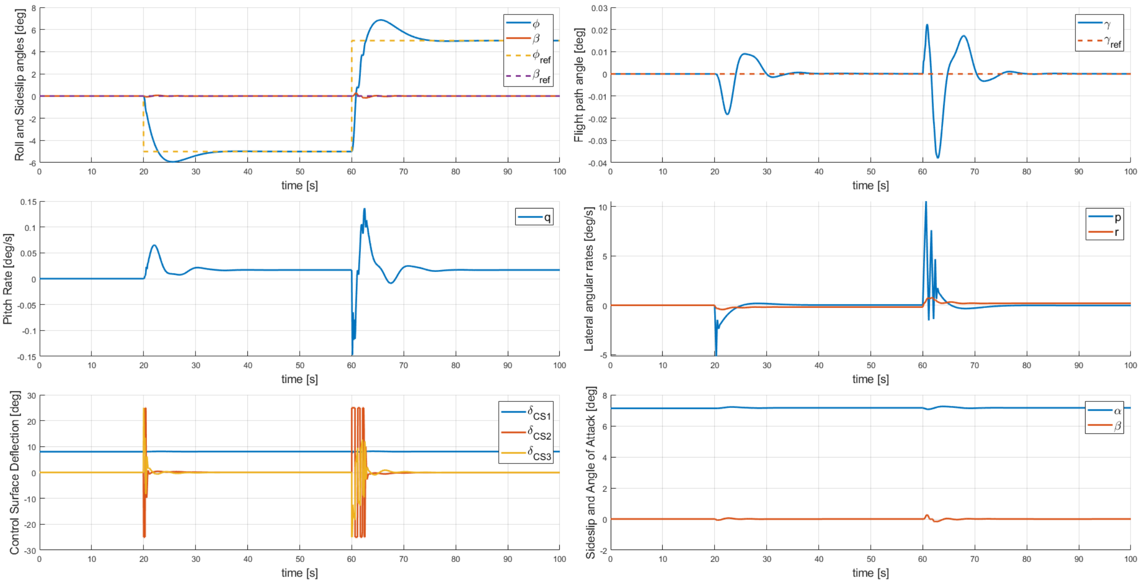

Figure 5.22: Roll angle tracking performance PID controller

	INDI	PID
Rise Time 1 [s]	0.81	2.255
Rise Time 2 [s]	1.1	2.67
Overshoot 1 [-]	1.181	1.187
Overshoot 2 [-]	2.045	1.3733
Settling time 1 [s]	6.35	13.825
Settling time 2 [s]	9.61	14.505
e_{SS_1} [%]	$1.98 \cdot 10^{-5}$	$2.6 \cdot 10^{-4}$
e_{SS_2} [%]	$2.93 \cdot 10^{-5}$	$5.1 \cdot 10^{-4}$
RMS error [deg]	$1.70 \cdot 10^{-2}$	$1.82 \cdot 10^{-2}$

Table 5.20: Roll angle tracking statistics

5.5.5. Gibson Criteria

As is explained in chapter 4.1 Handling Qualities are also an important way to analyse the performance of a FCS. For this preliminary analysis the Dropback and Flight path angle delay criteria of the Gibson Criteria are analysed.

To determine if the two controllers meet the criteria, a pitch rate reference step signal was given of $1[°/s]$ between 1 and 6 seconds. The results from the INDI controller can be seen in Figure 5.23 and for the PID controller in Figure 5.24.

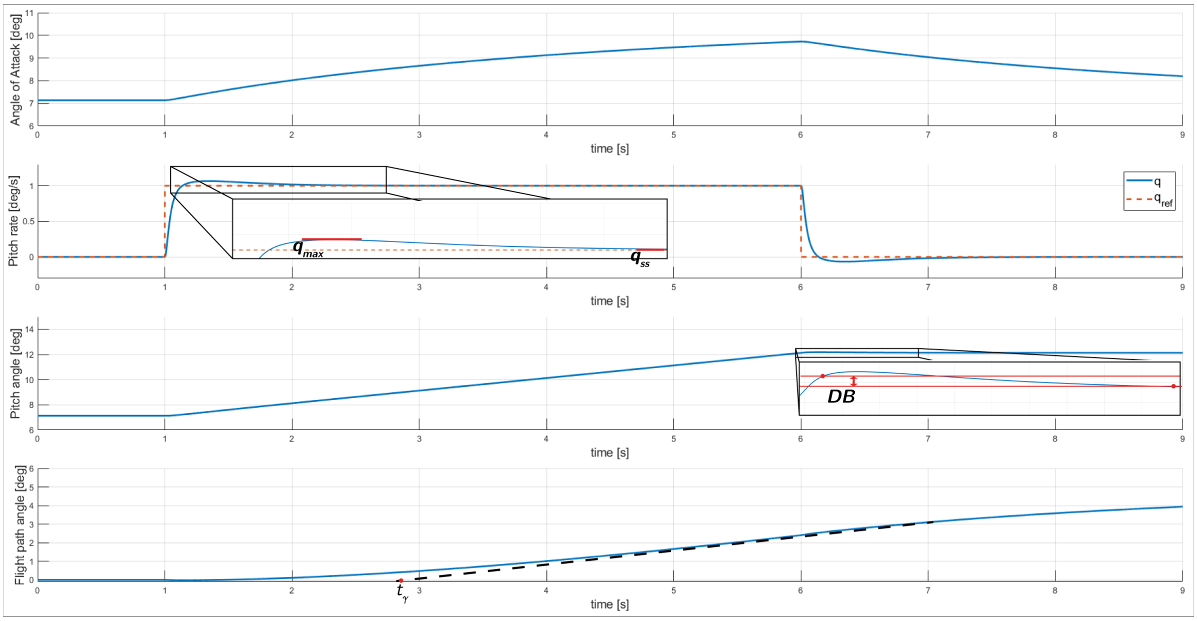

Figure 5.23: INDI Pitch rate respons for Gibson criteria

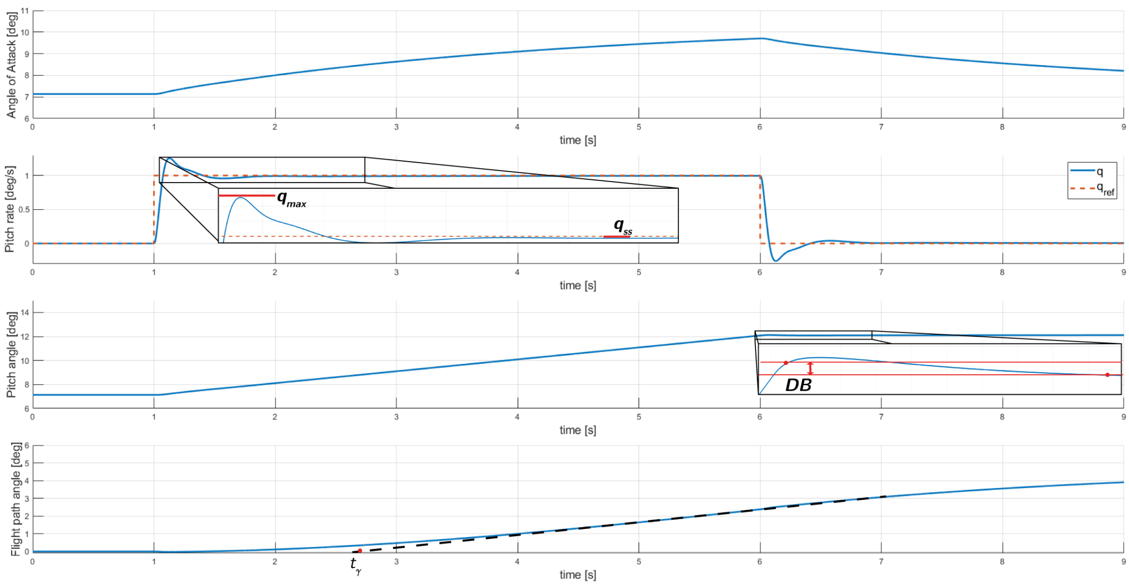

Figure 5.24: PID Pitch rate respons for Gibson criteria

From this the ratio between the overshoot and steady state (q_{max}/q_{ss}, Dropback ratio $((\theta_{t=6} - \theta_{ss})/q_{ss})$ and t_γ could be determined. These are listed in Table 5.21.

In Figure 5.25 it can be seen for which values of dropback ratio and overshoot ratio the Gibson dropback criterion is met. The INDI controller is in the satisfactory area, as well as the PID controller.

	INDI	PID
$\frac{q_{max}}{q_{ss}}[-]$	1.066	1.26
$\frac{DB}{q_{ss}}[-]$	0.017	0.016
$t_\gamma[s]$	1.763	1.767

Table 5.21: Gibson criteria parameters PID and INDI controller

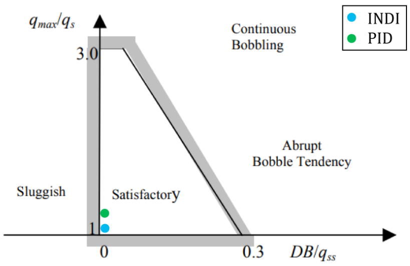

Figure 5.25: Gibson Dropback Criterion [15]

For the flight path angle delay criterion, t_γ should be less than $1.5[s]$ and less than $1[s]$ for precise flying tasks [15]. Both controllers do not meet this requirement. The performance of the INDI controller on this point could be improved by adding the command filter as proposed by Smit [36].

5.6. Comparison with earlier work

In this section, the results of this preliminary analysis will be compared with the results of van Overeem [27]. A difference between the controller from van Overeem and the controller used in this analysis, are the tuning of the gains, which causes the difference in results.

In Figure 5.26 a flight path angle tracking and roll angle tracking response from van Overeem [27] is given. It should be noted that this is in approach conditions. Due to the different tuning of the gains, the response is quite different. So is there no overshoot, and are there more oscillations at the roll angle response.

Both simulations show minimum phase behaviour at the flight path angle responses. Van Overeem also noticed that there is a lack of lateral control authority and suggests to also use the inner elevon for lateral control to improve the control authority.

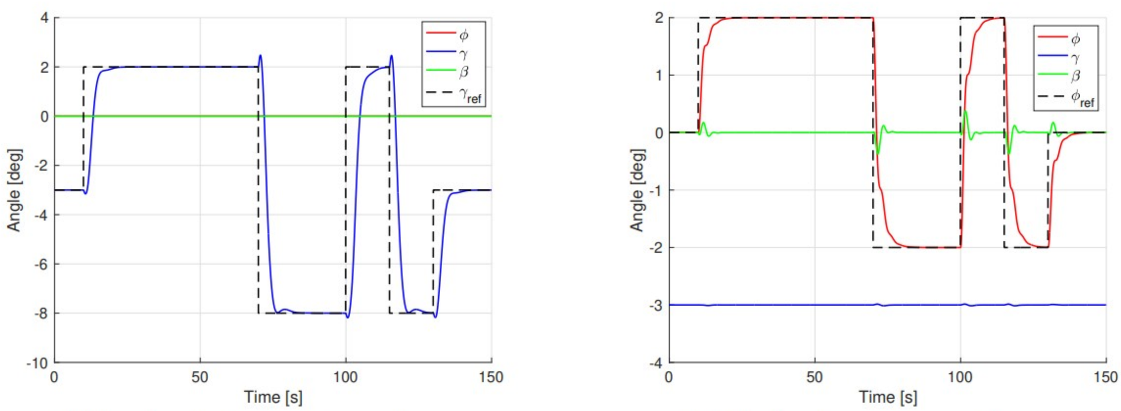

(a) Flight path angle reference trajectory and response.

(b) Roll angle reference trajectory and response.

Figure 5.26: Results INDI controller from van Overeem [27]

5.7. Conclusion Preliminary Analysis

In this chapter the performance of an INDI controller is compared to a PID controller for the Flying-V. When looking at the tracking performance of the inner loop stability augmentation system, the INDI controller performs better for the pitch rate. The PID controller is faster for the roll rate, but it has more problems with the coupled roll and yaw rate, and has more oscillations.

For approach, the difference in performance between the pitch rate tracking is slightly better for the PID controller, but the difference is larger with the roll rate tracking, as the PID struggles by accurately tracking the reference signal. This could be due to the coupling between roll and yaw rate. There are problems with saturated control surfaces with both the INDI and PID controller. Therefore the effect of using the inboard elevons for lateral control is probably necessary. It could also be investigated if adding pseudo control hedging to the controller can improve this issue. Another solution might be to use a control surface layout with more control authority.

The differences between both flight path angle tracking performances are mostly in the oscillating behaviour of the PID controller, which is not apparent with the INDI controller. This might be caused by the slightly more aggressive oscillating pitch rate tracking performance of the PID controller. Retuning the inner loop might give better outer loop performance but would lead to slightly worse inner loop performance.

The same can be said about the roll angle tracking, where the PID controller has also slower settling and rise times. It also oscillates more and the control surface are more switching between both actuator limits.

When looking at the Gibson criteria, there is not much difference between both controllers. Both are in the satisfactory region for the dropback criteria, and are not meeting the flight angle delay criterion, for which a redesign of the inner loop controller with a command filter should be considered. A reevaluation and change in the cost function for the tuning of the gains can also help in meeting the Gibson criteria.

In general, the INDI controller shows better performance, especially when dealing with roll and yaw rate, and suffer less form oscillating behaviour. This could already be seen when tuning the controllers, as the INDI controller got better scores. It is therefore also possible that for the parameters where the PID controller performed better, the INDI controller could also get this performance if the cost score for tuning was defined differently.

III

Additional Results

6 Linearization verification

As the linear analysis of the flight control system is a large part of the tuning and is necessary for determining a large number of the handling qualities, it is important that the linearization of the system is accurate. The linearization of the MATLAB Simulink model is done with the function linearize() [1]. The model is linearized to a continuous-time system, with the rate conversion method set to Tustin. To verify that the model is linearized accurately, the nonlinear model, as well as the linear model is subjected to a box input from t = 5s until t = 15s. The input is 1.8 for the longitudinal responses, and 5 degrees for the lateral responses.

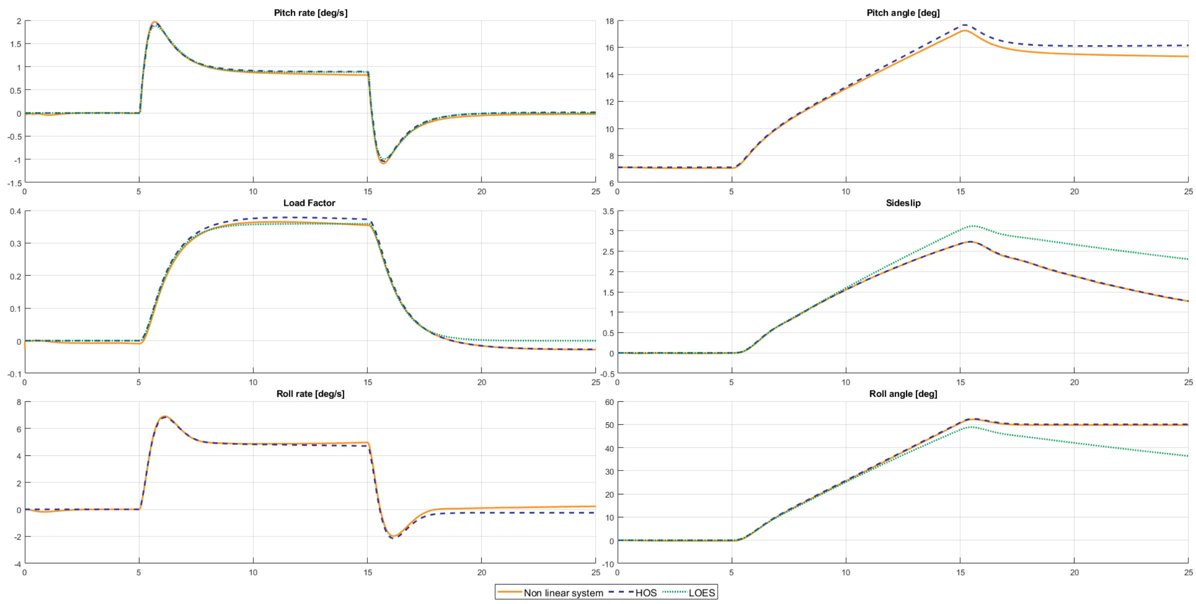

Figure 6.1: The difference in response between the nonlinear and linear model

The results can be seen in Figure 6.1. The difference in pitch rate and roll rate response is very small, as well as for the load factor response. For sideslip and roll angle the responses of the nonlinear and linear models seem to be almost exactly the same. For pitch angle, the error seems to increase over time, but the difference is still small and can be explained by the fact that some nonlinear effects cause the difference. It can therefore be concluded that the linearization of the model, which includes the sensor dynamics and discretization effects is accurate. In the figure the LOES model is also plotted, if applicable. It can also be seen here that the LOES model is also fitted correctly, however, there is a deviation in sideslip and roll angle, which is as expected, as the LOES model can not take into account all the different effects, as it is a reduced model, where, for example, the longitudinal case only the

[1] https://www.mathworks.com/help/slcontrol/ug/linearize.html

short period eigenmode is taken into account, so long term effects from the phugoid eigenmode, are not taken into account.

7

LOES fit algorithm

After the linear High Order System is obtained, it is also important that the Low Order Equivalent System is fitted as best as possible. The calculation of the score is explained in the scientific paper. The fitting score is optimized by the MATLAB function fmincon() [1], with the optimization algorithm set to 'sqp'. To obtain the initial guess for the LOES parameters, an initial guess of the LOES transfer function is made. This is done by using the frequency response data from 0.1 rad/s up to 10 rad/s with the MATLAB function tfest() [2]. To verify if the LOES fitting algorithm is able to find the correct parameters, two different HOS systems were tested with the pitch and load factor LOES models. The first is one is actually the LOES model itself, so the fitting algorithm should find exact same values, the pitch rate transfer function is given in Equation 7.1, and the load factor in Equation 7.2

$$\frac{q(s)}{\delta_e(s)} = \frac{0.5\left(s+\frac{1}{3}\right)e^{-0.1s}}{s^2 + 2\cdot 1.3\cdot 1.1s + 1.1^2} \tag{7.1}$$

$$\frac{n_z'}{\delta_e(s)} = \frac{4e^{-0.5s}}{s^2 + 2\cdot 1.3\cdot 1.1s + 1.1^2} \tag{7.2}$$

The second HOS model is based on the non-simplified LOES model, with phugoid dynamics. The frequency of the phugoid is set to 0.06, with a damping ratio of 1.2. The pitch rate function is given in Equation 7.3 and the load factor function in Equation 7.4

$$\frac{q(s)}{\delta_e(s)} = \frac{1s\left(s+\frac{1}{4}\right)\left(s+\frac{1}{8}\right)e^{-0.05s}}{\left(s^2 + 2\cdot 0.3\cdot 2.2s + 2.2^2\right)\left(s^2 + 2\cdot 1.2\cdot 0.06s + 0.06^2\right)} \tag{7.3}$$

$$\frac{n_z'}{\delta_e(s)} = \frac{3s\left(s+\frac{1}{3}\right)e^{-0.04s}}{\left(s^2 + 2\cdot 0.3\cdot 2.2s + 2.2^2\right)\left(s^2 + 2\cdot 1.2\cdot 0.06s + 0.06^2\right)} \tag{7.4}$$

The frequency responses of the two HOS models and fitted LOES models can be seen in Figure 7.1. The frequency response of LOES 1 perfectly fits the HOS, indicating that the correct parameters were found. For model 2 there are some differences at the lower frequencies, which are caused by the phugoid dynamics that will not be present in the LOES model. Final verification is done by comparing the relevant LOES parameters with the parameters that were expected in Table 7.1. From the table, it can be confirmed that for HOS 1, the LOES is indeed perfectly fit, for HOS2 there are some small deviations, but this was as expected, as the values are slightly pulled towards the extra values in the HOS, that cannot be represented in the LOES.

[1] https://www.mathworks.com/help/optim/ug/fmincon.html
[2] https://www.mathworks.com/help/ident/ref/tfest.html

	HOS_1	$LOES_1$	HOS_2	$LOES_2$
T_{θ_2}	3	3	4	4.4
τ_e	0.1	0.1	0.05	0.05
ω_{sp}	1.1	1.1	2.2	2.194
ζ_{sp}	1.3	1.3	0.3	0.33
τ_{en}	0.5	0.5	0.04	0.0486

Table 7.1: LOES parameters compared with parameters from HOS

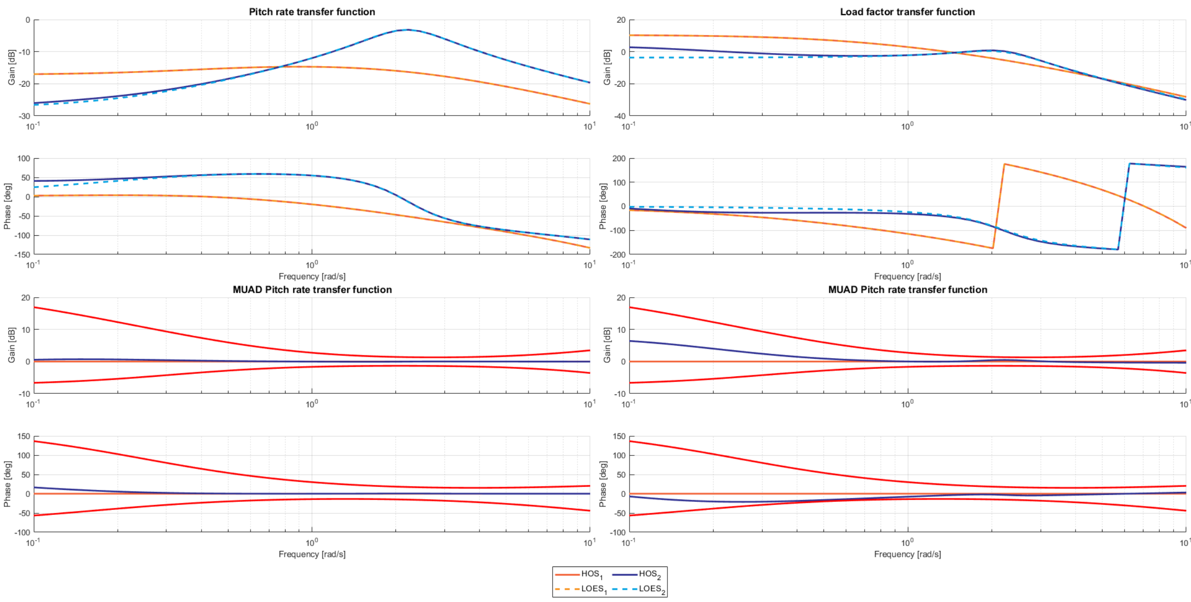

Figure 7.1: Frequency responses of the HOS models, as well as the fitted LOES models

8 Additional step responses in cruise and approach conditions

The response of the controller to a C* input in approach conditions is given in Figure 8.1. It can be seen that the retuning improved the performance, as fewer oscillations in pitch rate and load factor response are present. In Figure 8.2 the response to a roll rate block input is given in approach conditions. The largest difference in the two cases is in the sideslip, where the retuned model is better able to keep the sideslip angle close to zero. When looking at the control surface deflections, the reason for this is found, as the cruise tuning reaches the saturation limits of the rudder.

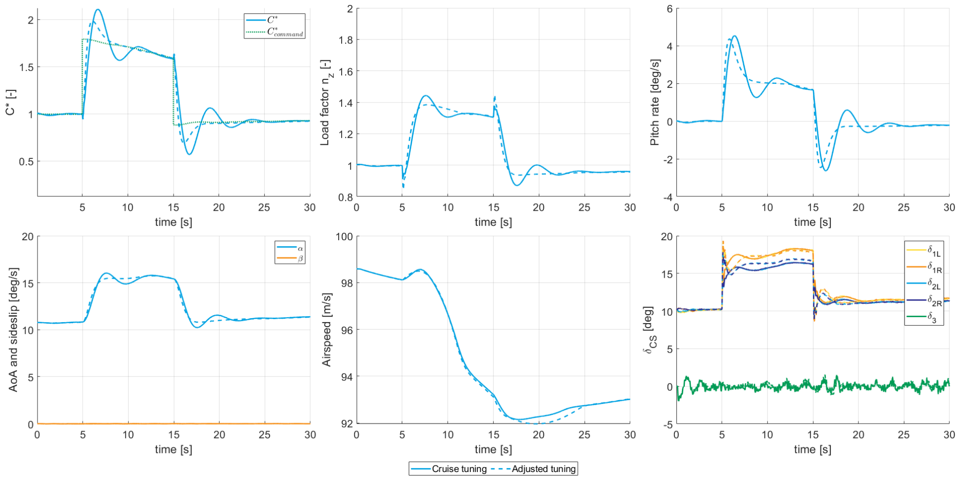

Figure 8.1: C* step input response in approach conditions

To check the ability of the control system to deal with disturbances, a wind gust w_{wind} was applied. The response in cruise can be found in Figure 8.3, and for the approach condition in Figure 8.4. For both cases is the aircraft back at it's initial angle of attack after around 3 seconds. In cruise condition there is one oscillation in pitch rate when recovering to it's initial condition, this oscillation is not present for the approach case.

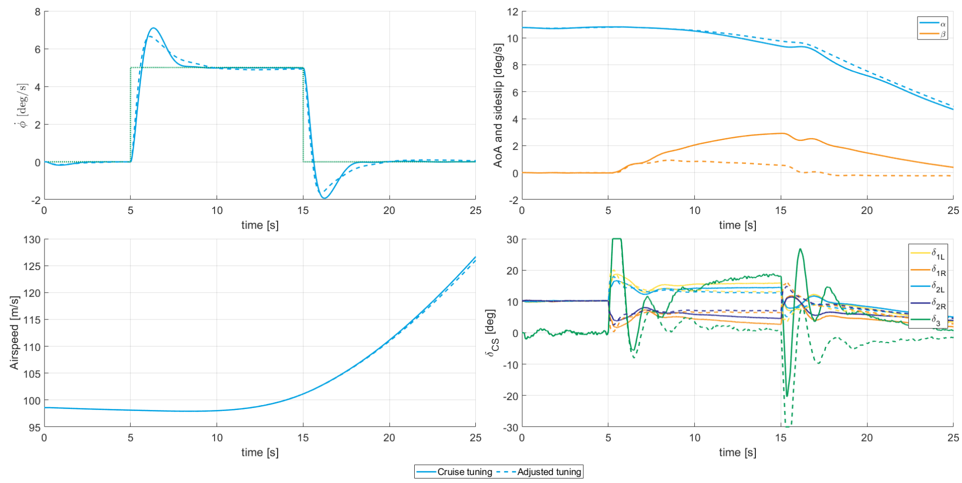

Figure 8.2: Roll rate step input response in approach conditions

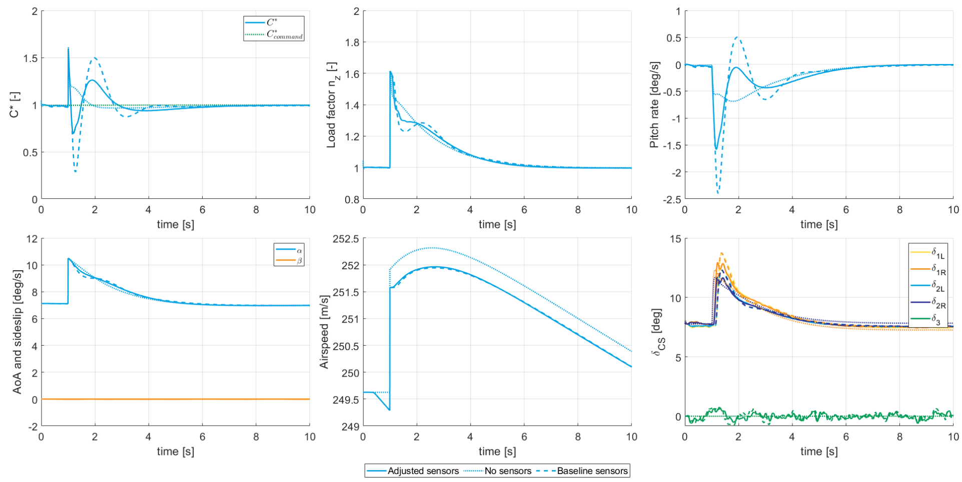

Figure 8.3: Response in cruise condition to a wind step w_{wind} of 15 m/s

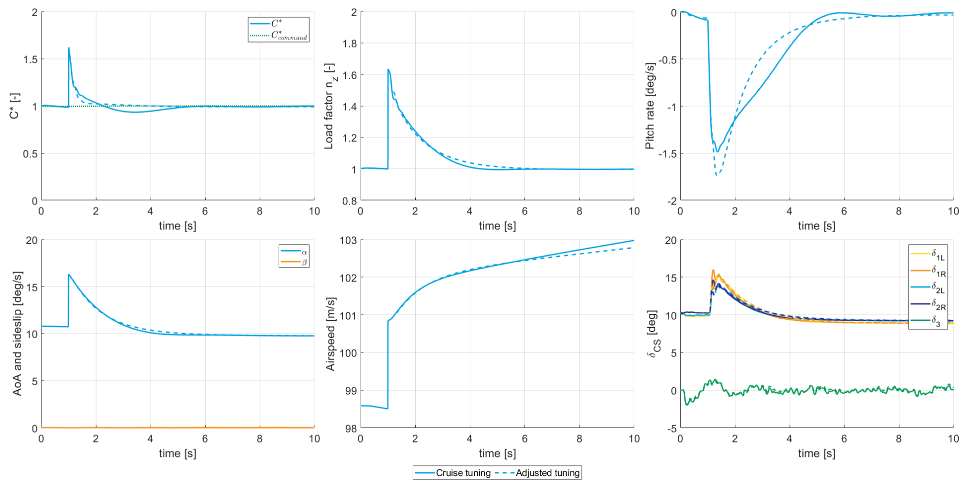

Figure 8.4: Response in approach condition to a wind step w_{wind} of 10 m/s

9

Additional Flight Envelope Protection test cases

In Figure 9.1, the simulation results of the flight envelope protection starting from 1 km altitude, without roll. When comparing these results the results from cruise conditions, there are two main differences. The first one is that the pitch angle oscillates more. It should be kept in mind that the simulation time is 100 s instead of 250, as the aircraft reaches the angle of attack limit faster in this condition. The pitch angle goes below zero twice, instead of only once.

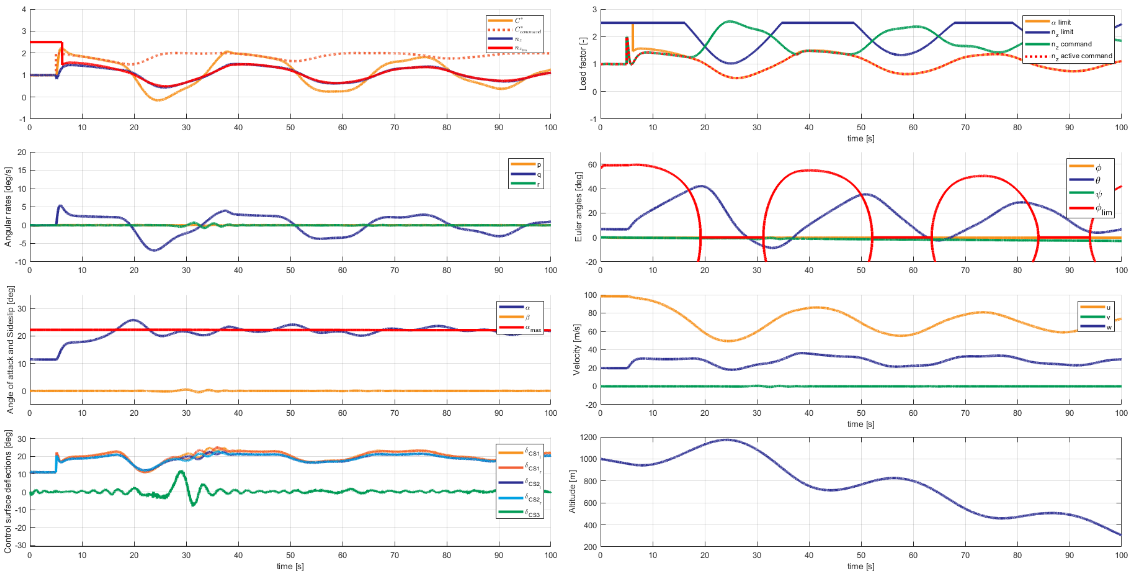

Figure 9.1: Flight Envelope Protection starting from 1 km altitude

The rudder oscillation in this case seems to have a lower frequency, but higher amplitude. The oscillations occur at an airspeed of around 50 m/s, so it could possibly be resolved by scheduling gains for this low velocity. To check this an additional simulation was run, where the gains K_r and K_{b_i} were halved for airspeeds below 60 m/s. The results of these simulation can be found in Figure 9.2.

When comparing both figures, there are two differences, both related to sideslip. First, in the case with extra gain scheduling, the sideslip actually stays zero, whereas in the other case there are some errors, this also is visible in rudder deflections, as the oscillations are less present in the second case. This indicates that the extra gain scheduling solves the problems with the rudder deflections.

In Figure 9.3 the results from the FEP simulation starting from 1 km, with roll and the extra gain scheduling is given. When compared to the case without the extra gain scheduling, it can be seen that

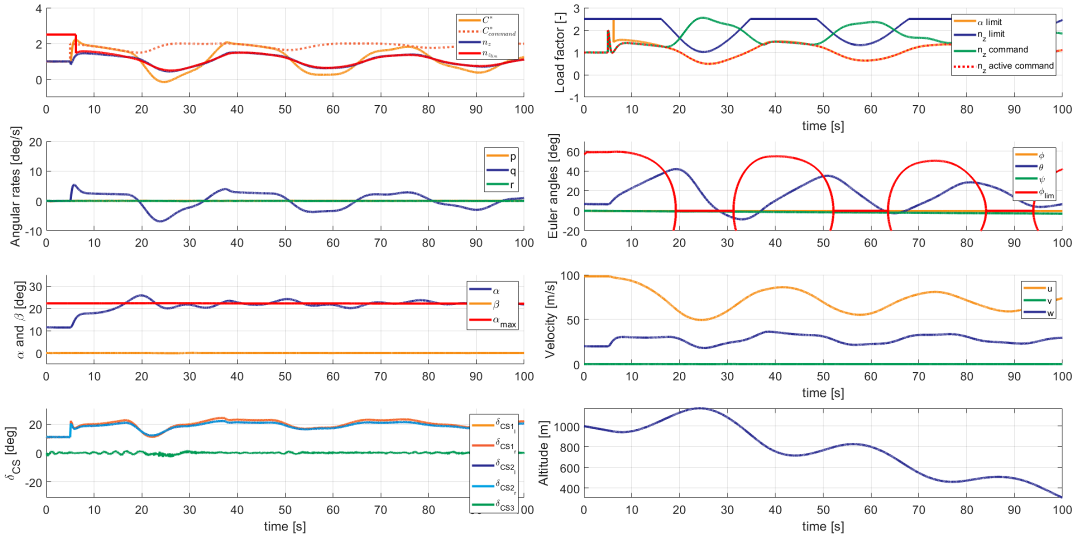

Figure 9.2: Flight Envelope Protection starting from 1 km altitude, with extra gain scheduling

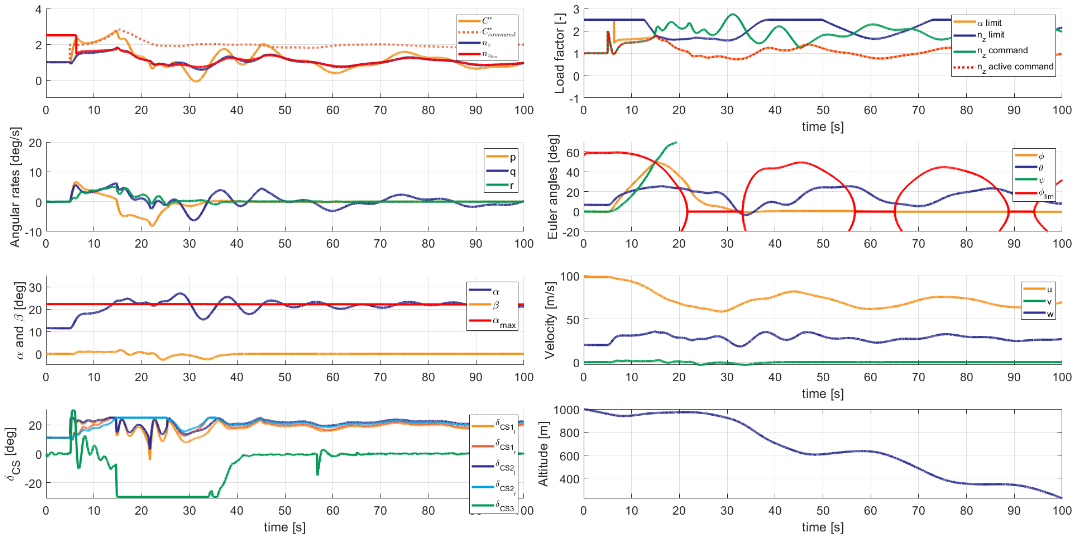

Figure 9.3: Flight Envelope Protection starting from 1 km altitude, with roll and extra gain scheduling

the oscillations in the rudder control surface deflections are less, however, it still reaches its saturation limits. From this it can be concluded that the extra gain scheduling can improve on the problems with the rudder oscillations, however, the lack of control authority from the rudder still remains a problem that should be kept in mind.

10
Effect of difference in control effectiveness

To further investigate the larger rudder oscillations with larger differences in aerodynamic model parameters, the control effectiveness parameters were varied from -20 % to 20 %. The Rudder activity is plotted in Figure 10.1.

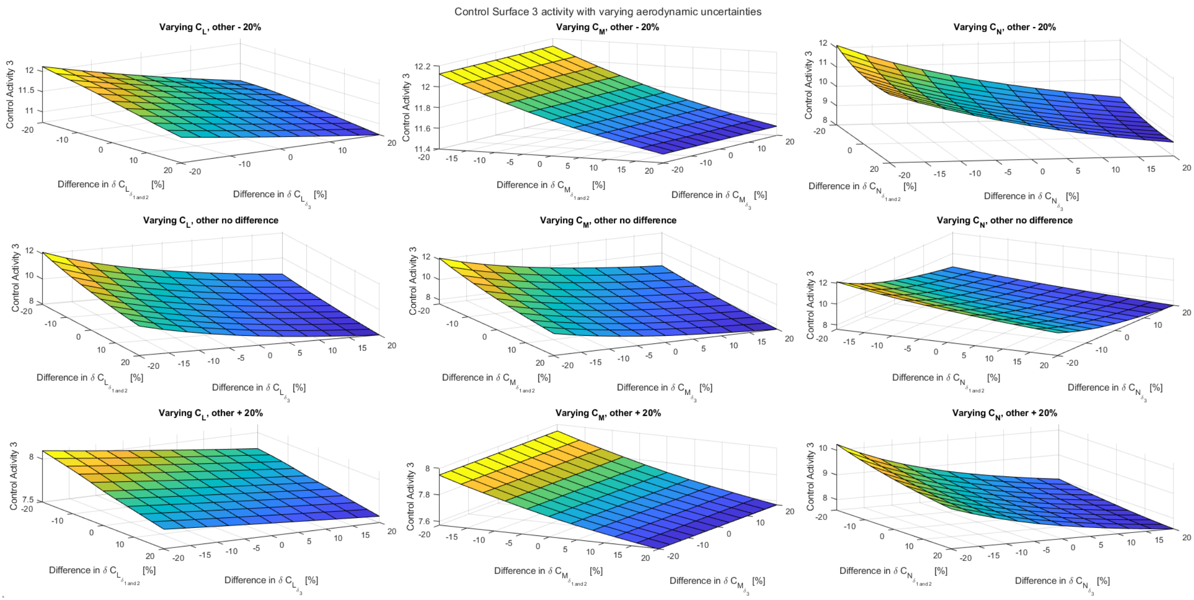

Figure 10.1: Rudder activity with changing control effectiveness parameters

In Figure 10.1 it can be seen that the rudder activity is the largest when each parameter is overestimated, indicating that the oscillations occur when the control effectiveness is overestimated. This can be explained by the fact that for these cases the control authority is lowered, and therefore the control surfaces have to move more.

IV

Conclusion

11 Conclusions

The goal of this thesis research is to increase the maturity of the Flight Control System of the FlyingV by testing and if necessary improving the INDI-based flight control laws in high angle of attack conditions and with other effects. To achieve this objective multiple research questions were established that need to be answered.

Research question 1 was what the current challenges are in controlling the Flying-V. By looking at the literature it was found that the Flying-V has pitch breakup tendencies at angles of attack larger than $20°$ and an unstable dutch roll in certain conditions. The Flying-V has also limited control authority, especially for lateral control. It was also found that an INDI controller for the Flying-V is already proposed, but that different effects that influence the robustness of this controller were not investigated yet, such as sensor dynamics and discrete time effects, as well as high angle of attack conditions. In this research the INDI controller is further investigated, with different outer loop control laws, as well as Flight envelope protection

The next research question 2 was: ”What is the state of the art of INDI flight control?”. Research on INDI shows that it has good performance and robustness against model parameter uncertainties. However, measurement delays and saturation limits can decrease performance. For saturation problems, pseudo-control hedging can be a solution to windup problems, and for measurement delays, a hybrid INDI form can improve the performance. INDI has also been used on other forms of flying wings, where it was shown to be able to deal with problems that are usually associated with flying wings, such as the non-linearity and coupled control surfaces.

The third research question was ”What is the performance of the INDI controller for the Flying-V under high angle of attack conditions”. This question has three subquestions,

1. the first question was how the performance of the controller could be evaluated. For this handling quality requirements are used, as well as metrics such as tracking error. For the handling qualities a linear analysis was done, to determine the bandwidth, as well as fit a Low Order Equivalent System to find the CAP, short period parameters, roll, and spiral mode, as well as dutch roll damping and frequency. The linear analysis was also used to determine gain and phase margins. Finally, simulations were done to determine the control surface activity.

2. The second question was what requirements there are for high angle of attack conditions. As the Flying-V can go in auto-rotation for high angles of attack, a Flight Envelope Protection law was implemented to prevent reaching the very high angles of attack. However, the aircraft should still be able to reach angles of attack near the limit, as well as safe return from high angle of attack to lower angles of attack. The requirements for the flight envelope protection were determined that the angle of attack should not go above 30 degrees, that the protection should not influence the control system when the aircraft is well within its flight envelope and the load factor should never go outside of the limits, which are between -1 and 2.5g.

3. The third question was ”How can the INDI controller be extended to include Flight envelope protection?” The Flight control system was extended with a load factor, angle of attack, and roll angle protection law. The load factor protection was applied by limiting the commanded load factor. The angle of attack protection law is also applied by limiting the commanded load factor, where the difference in angle of attack and maximum angle of attack is used in combination with a gain to obtain the maximum load factor for the angle of attack protection. The roll angle protection is applied by limiting the commanded roll rate.

From this, it can be concluded that the FCS is able to perform at high angle of attack conditions, without reaching the limit set at 30 degrees angle of attack, in the cases that were tested. The implemented flight envelope protection was evaluated at 1 and 13 km altitude and was found to meet the set requirements. It should, however, be mentioned that there are some issues with rudder oscillations, this can probably be solved by improving the gain scheduling, by not only making it dependent on airspeed but also on air density. During the simulation of the FEP at 1 km height, with a roll command, the control surfaces are saturated for a long time, and the envelope protection is even in this condition able to function. It should however be further investigated if certain inputs at this condition could cause problems, and if more protection laws are required to prevent this.

Finally, the fourth research question, was ”What the influence of different effects are on the robustness of the INDI controller?” This question was divided into four subquestions. These questions are:

1. The first question was ”How is robustness of a control system defined?” The robustness of a control system is the ability of the control system to deal with uncertainties, these uncertainties can be aerodynamic uncertainties, but also unmodeled dynamics, time delay, and lag, sensor noise, or sampling frequency.

2. The second question was ”What is the influence of time delay?” In this research, the effect of time delay due to sensor dynamics were investigated. The main effect of the time delay due to the sensor dynamics was the reduction of the phase margins, and pitch attitude bandwidth. It was also found that a synchronization filter was required, to ensure the actuator deflections are in sync with the angular acceleration dynamics. The body rate sensor was identified to be the most critical sensor for the time delay. With the proposed flight control system the time delay of this sensor could not be larger than 0.04 s, to be able to tune the control laws for having enough phase margin, while also having a pitch attitude bandwidth of at least 3 rad/s.

3. The third question was ”What is the influence of the sampling frequency?” To analyse the effect of the sampling frequency, the controller was set up as a discrete-time system, with the aircraft dynamics itself still being a continuous-time system. When simulating different sampling frequencies, it was found that when the sampling time decreases, the tracking error and control surface activity increases, which is as expected. It was further found that the error does not decrease much when sampling time goes lower then 0.01 s. For sampling times above 0.1s, the system becomes unstable.

4. Finally, the fourth question was ”What is the influence of aerodynamic uncertainties?” The effect of aerodynamic uncertainties was investigated by running simulations with varying aerodynamic coefficients. It was found that for the investigated variance (of 20 %), the tracking error does not change much. The control surface activity does increase more, especially the rudder activity. It was therefore concluded that the control system is robust for aerodynamic uncertainties.

Combining the answers to the subquestions it can be concluded that time delay has the largest effect on the performance of the control system. For the proposed controller, the handling qualities could be within level 1, as long as the time delay of the body rate sensor is not higher than 0.04 s. The sampling time of the controller should not be higher than 0.1 s, but with a sampling time of 0.01 s, is the tracking error reduced. Further reduction of the sampling time has less effect on the tracking error. Aerodynamic uncertainties only have a minor effect on the tracking error, only a reduction of rudder control authority could be problematic.

In this research, a flight control system was proposed with an INDI inner-loop and a C* control law for longitudinal control and a Rate Control Attitude Hold roll control law. The control system was evaluated with discretization effects and sensor dynamics, where it was found that the controller has predicted level 1 handling requirements at cruise and approach conditions, as long as the body rate sensor has no more than 0.04 s time delay. It was also found that the controller is stable as long as the sampling time is less than 0.1 s, and that it is robust for model uncertainties. The controller also contains flight envelope protection laws, which were tested successfully at 1 and 13 km altitudes. With this research, a next step in the maturity of the Flight Control system of the Flying-V was made.

12 Recommendations

To further increase the maturity of the controller of the Flying-V there are multiple areas that could be investigated in further work. This work only looked at one c.g. location and evaluated the aircraft only in cruise and approach conditions, but other points in the flight envelope should also be investigated. There are also other effects that could degrade the performance of the controller which are not investigated yet, such as aero-elasticity effects, nuisance dynamics, and time delay caused within the flight controller. To further increase the maturity of the FCS it is important that the aero-elasticity effects are also taken into account, as well as that the FCS is meeting the Handling requirements in the whole flight envelope.

It was also assumed that the c.g. location, weight of the aircraft, control surface deflection, and air density are known for the control system, the effects of a mismatch in this should also be investigated.

As the time delay of the angular rate sensor was found to be the most critical for the controller's ability to meet all requirements, it should be investigated if the requirement on the sensor is feasible and if for example, the use of Hybrid INDI could make this requirement less stringent.

There is also further research possible for the flight envelope protection. The flight envelope protection could for example be improved by also taking the angle of attack rate into account, to see if this could increase the maximum angle of attack. It could also be investigated if airspeed protection is required, and if protection further protection for control surface saturation is required. Certification requirements for the flight envelope protection should also be investigated.

Finally, the rudder oscillations should be looked into. It should be checked if better gain scheduling, with also taking air density into account, improves this problem, and if better filtering of the sideslip signal would lead to an improvement, as well as if a larger rudder would improve performance.

Bibliography

[1] R van 't Veld, Erik-Jan Van Kampen, and Q Ping Chu. "Stability and Robustness Analysis and Improvements for Incremental Nonlinear Dynamic Inversion Control". In: *2018 AIAA Guidance, Navigation, and Control Conference*. DOI: 10.2514/6.2018-1127. URL: https://arc.aiaa.org/doi/abs/10.2514/6.2018-1127.

[2] Jürgen Ackermann. *Robust Control: The Parameter Space Approach*. 2nd ed. Springer, 2002. ISBN: 978-1-85233-514-4. DOI: 10.1007/978-1-4471-0207-6.

[3] European Union Aviation Safety Agency. *Type-Certificate Data Sheet No. E.111 for Trent XWB Series Engines*. 2019. URL: https://www.easa.europa.eu/document-library/type-certificates/engine-cs-e/easae111.

[4] Gavin K. Ananda et al. "Design Methodology for a Dynamically-Scaled General Aviation Aircraft". In: *35th AIAA Applied Aerodynamics Conference*. DOI: 10.2514/6.2017-4077. URL: https://arc.aiaa.org/doi/abs/10.2514/6.2017-4077.

[5] B.J. Bacon and A.J. Ostroff. "Reconfigurable flight control using nonlinear dynamic inversion with a special accelerometer implementation". In: *AIAA Guidance, Navigation, and Control Conference and Exhibit*. DOI: 10.2514/6.2000-4565. URL: https://arc.aiaa.org/doi/abs/10.2514/6.2000-4565.

[6] B.J. Bacon, A.J. Ostroff, and S.M. Joshi. "Reconfigurable NDI controller using inertial sensor failure detection & isolation". In: *IEEE Transactions on Aerospace and Electronic Systems* 37.4 (2001), pp. 1373–1383. DOI: 10.1109/7.976972.

[7] Justus Benad. *The Flying V - A new Aircraft Configuration for Commercial Passenger Transport*. Nov. 2015. DOI: 10.25967/370094.

[8] Thibaut Cappuyns. "Handling Qualities of a Flying V Configuration". M.Sc Thesis. TU Delft, 2019. URL: http://resolver.tudelft.nl/uuid:69b56494-0731-487a-8e57-cec397452002.

[9] Michael V. Cook. *Flight Dynamics Principles: A Linear Systems Approach to Aircraft Stability and Control*. Butterworth-Heinemann, 2013. ISBN: 978-0-08-098242-7. DOI: 10.1016/C2010-0-65889-5.

[10] S.A. van Empelen and Roelof Vos. "Effect of Engine Integration on a 4.6%-Scale Flying-V Subsonic Transport". In: *AIAA 2021-0939 Session: Aerodynamic Testing: Ground, Wind-Tunnel and Flight Testing I*. AIAA Scitech 2021 Forum, 2021. DOI: 978-1-62410-609-5.

[11] F Faggiano. "Aerodynamic Design Optimization of a Flying V Aircraft". M.Sc Thesis. TU Delft, 2016. URL: http://resolver.tudelft.nl/uuid:0b1472a5-3aad-433c-9a64-242c84b114fd.

[12] W Falkena. "Investigation of practical flight control systems for small aircraft". English. PhD thesis. TU Delft, 2012. ISBN: 978-94-6203-258-3.

[13] Gregg G. Fliming and Ivan de Lépinay. "Environmental Trends in Aviation to 2050". In: *2019 Environmental Report*. ICAO, 2019, pp. 17–23. URL: https://www.icao.int/environmental-protection/Documents/EnvironmentalReports/2019/ENVReport2019_pg17-23.pdf.

[14] A Ruiz Garcia, Roelof Vos, and C.C. de Visser. "Aerodynamic model identification of the flying V from wind tunnel data". In: (2020). DOI: 10.2514/6.2020-2739.

[15] J.C. Gibson. "Development of a design methodology for handling qualities excellence in fly by wire aircraft". PhD thesis. TU Delft, 1999. ISBN: 90-407-1841-5. URL: http://resolver.tudelft.nl/uuid:6b564b35-cb74-436c-8c47-845bfbbb8b4d.

[16] Fabian Grondman et al. “Design and Flight Testing of Incremental Nonlinear Dynamic Inversion-based Control Laws for a Passenger Aircraft”. In: *2018 AIAA Guidance, Navigation, and Control Conference*. DOI: 10.2514/6.2018-0385. URL: https://arc.aiaa.org/doi/abs/10.2514/6.2018-0385.

[17] R Grotens. “Nonlinear Flight Control: Fault Tolerant Control with Sliding Modes and Control Allocation”. M.Sc Thesis. TU Delft, 2010. URL: http://resolver.tudelft.nl/uuid:29ddf25f-bcc3-47f3-9c26-53da9b6d9301.

[18] Jackson Horwitz. “Parametric Design of the Flying-V Winglets for Improved Lateral-Directional Stability and Control”. M.Sc Thesis. TU Delft, 2021. URL: http://resolver.tudelft.nl/uuid:d7513b36-b9fd-4f8a-8726-f5c7ee7f3a6b.

[19] Balaji Jayaraman, Dipak Kumar Giri, and Ajoy Kanti Ghosh. “Attitude Tracking Control of a Light Aircraft Using Classical and Incremental Nonlinear Dynamic Inversion Approaches”. In: (2021), pp. 985–993. DOI: 10.1109/ICUAS51884.2021.9476803.

[20] Nelson Johnson. “Effect of Winglet Integration and Rudder Deflection on Flying-V Aerodynamic Characteristics”. M.Sc Thesis. TU Delft, 2021. URL: http://resolver.tudelft.nl/uuid:b664ae03-846f-4ad3-849a-c081a32260ad.

[21] Chong-Sup Kim et al. “Stability Margin and Structural Coupling Analysis of a Hybrid INDI Control for the Fighter Aircraft”. In: *International Journal of Aeronautical and Space Sciences* 22 (2021), pp. 1154–1169. DOI: 10.1007/s42405-021-00394-8.

[22] Yagiz Kumtepe. “Flight Control Design Using Hybrid Incremental Nonlinear Dynamic Inversion”. M.Sc Thesis. TU Delft, 2020. URL: http://resolver.tudelft.nl/uuid:755193c5-9a83-47bc-a904-bfb0f2a4579a.

[23] Yu Li et al. “Angular acceleration estimation-based incremental nonlinear dynamic inversion for robust flight control”. In: *Control Engineering Practice* 117 (2021), p. 104938. ISSN: 0967-0661. DOI: https://doi.org/10.1016/j.conengprac.2021.104938. URL: https://www.sciencedirect.com/science/article/pii/S096706612100215X.

[24] Peng Lu et al. “Aircraft fault-tolerant trajectory control using Incremental Nonlinear Dynamic Inversion”. In: (2016). DOI: 10.1016/j.conengprac.2016.09.010.

[25] R. Martinez-Val. “Flying Wings. A New Paradigm for Civil Aviation?” In: *Acta Polytechnica* 47 (Jan. 2007). DOI: 10.14311/914.

[26] Christopher Miller. “Nonlinear Dynamic Inversion Baseline Control Law: Flight-Test Results for the Full-scale Advanced Systems Testbed F/A-18 Airplane”. In: *AIAA Guidance, Navigation, and Control Conference*. DOI: 10.2514/6.2011-6468. URL: https://arc.aiaa.org/doi/abs/10.2514/6.2011-6468.

[27] Simon van Overeem. “Modelling, Control, and Handling Quality Analysis of the Flying-V”. M.Sc Thesis. TU Delft, 2021. URL: http://resolver.tudelft.nl/uuid:7fd04eec-41d4-4967-b246-89fdfac2446e.

[28] Simon van Overeem, Xuerui Wang, and Erik-Jan Van Kampen. “Modelling and Handling Quality Assessment of the Flying-V Aircraft”. In: *MST-05, Modeling and Simulation of Air and Space Vehicle Dynamics, Systems, and Environments I, January 4*. AIAA SciTech 2022. DOI: 10.2514/6.2022-1429.

[29] Marco Palermo. “The Longitudinal Static Stability and Control Characteristics of a Flying V Scaled Model”. M.Sc Thesis. TU Delft, 2019. URL: http://resolver.tudelft.nl/uuid:6286f9e2-c24a-430c-a4fa-9fb67b9558b4.

[30] Tijmen Pollack and Erik-Jan Van Kampen. “Robust Stability and Performance Analysis of Incremental Dynamic Inversion-based Flight Control Laws”. In: *AIAA SCITECH 2022 Forum*. DOI: 10.2514/6.2022-1395.

[31] J. Roskam. *Airplane Flight Dynamics and Automatic Flight Controls*. Airplane Flight Dynamics and Automatic Flight Controls dl. 1. Design Analysis and Research Corporation, 1995. ISBN: 9781884885174. URL: https://books.google.nl/books?id=RDZUG--o9HMC.

[32] S. Sieberling, Q. P. Chu, and J. A. Mulder. “Robust Flight Control Using Incremental Nonlinear Dynamic Inversion and Angular Acceleration Prediction”. In: *Journal of Guidance, Control, and Dynamics* 33.6 (2010), pp. 1732–1742. DOI: 10.2514/1.49978.

[33] P. Simplício et al. “An acceleration measurements-based approach for helicopter nonlinear flight control using Incremental Nonlinear Dynamic Inversion”. In: *Control Engineering Practice* 21.8 (2013), pp. 1065–1077. ISSN: 0967-0661. DOI: https://doi.org/10.1016/j.conengprac.2013.03.009. URL: https://www.sciencedirect.com/science/article/pii/S0967066113000634.

[34] Ewoud J. J. Smeur, Qiping Chu, and Guido C. H. E. de Croon. “Adaptive Incremental Nonlinear Dynamic Inversion for Attitude Control of Micro Air Vehicles”. In: *Journal of Guidance, Control, and Dynamics* 39.3 (2016), pp. 450–461. DOI: 10.2514/1.G001490.

[35] Ewoud J.J. Smeur. “Incremental Control of Hybrid Micro Air Vehicles”. PhD thesis. TU Delft, 2018. ISBN: 978-94-6186-973-9. DOI: 10.4233/uuid:23c338a1-8b34-40a6-89e9-997adbdafd75.

[36] Beau Smit. “Adaptive Incremental Nonlinear Dynamic Inversion for Consistent Pitch Rate Control”. M.Sc Thesis. TU Delft, 2021. URL: http://resolver.tudelft.nl/uuid:3014e195-28c7-49e9-9e29-1e468d045325.

[37] P.. Smith. “A simplified approach to nonlinear dynamic inversion based flight controlL”. In: *23rd Atmospheric Flight Mechanics Conference*. American Institute of Aeronautics and Astronautics, 1998. DOI: 10.2514/6.1998-4461.

[38] Phill Smith and Andrew Berry. “Flight test experience of a non-linear dynamic inversion control law on the VAAC Harrier”. In: *Atmospheric Flight Mechanics Conference*. DOI: 10.2514/6.2000-3914. URL: https://arc.aiaa.org/doi/abs/10.2514/6.2000-3914.

[39] Andreas Varga, Anders Hansson, and Guilhem Puyou. *Optimization Based Clearance of Flight Control Laws*. 1st ed. Springer Berlin, 2012. ISBN: 978-3-642-22627-4. DOI: 10.1007/978-3-642-22627-4.

[40] Rob Vliet. “Analysis of the flight characteristics of a highly swept cranked flying wing by means of an experimental test”. M.Sc Thesis. TU Delft, 2019. URL: http://resolver.tudelft.nl/uuid:90de4d9e-70ae-4efc-bd0a-7426a0a669c3.

[41] N. Wahler. “The Impact of Control Allocation on Optimal Control Surface Positioning and Sizing: A comparative study for a PrandtlPlane”. M.Sc Thesis. TU Delft, 2021. URL: http://resolver.tudelft.nl/uuid:5e9baf63-8a8f-4c1b-98cd-5aa993938027.

[42] Xuerui Wang et al. “Stability Analysis for Incremental Nonlinear Dynamic Inversion Control”. In: *Journal of Guidance, Control, and Dynamics* 42.5 (2019), pp. 1116–1129. DOI: 10.2514/1.G003791. URL: https://doi.org/10.2514/1.G003791.

[43] Jiannan Zhang et al. “Modeling and Incremental Nonlinear Dynamic Inversion Control for a Highly Redundant Flight System”. In: *AIAA Scitech 2019 Forum*. DOI: 10.2514/6.2019-1922.

[44] Shaojie Zhang, Wuhan Han, and Yuemei Zhang. “Finite Time Convergence Incremental Nonlinear Dynamic Inversion-Based Attitude Control for Flying—Wing Aircraft with Actuator Faults”. In: *Actuators* 9.3 (2020). ISSN: 2076-0825. DOI: 10.3390/act9030070.

[45] Shaojie Zhang and Qingkai Meng. “An anti-windup INDI fault-tolerant control scheme for flying wing aircraft with actuator faults”. In: *ISA Transactions* 93 (2019), pp. 172–179. ISSN: 0019-0578. DOI: https://doi.org/10.1016/j.isatra.2019.02.037.